

MATHEMATICAL MODELS OF BIOFILM IN VARIOUS ENVIRONMENTS

A Dissertation
Submitted to
the Temple University Graduate Board

in Partial Fulfillment
of the Requirements for the Degree of
DOCTOR OF PHILOSOPHY

by
Yilin Wu
August, 2019

Examining Committee Members:

Isaac Klapper, Advisory Chair, Department of Mathematics

Daniel B. Szyld, Department of Mathematics

Wei-Shih Yang, Department of Mathematics

Bettina Buttaro, Lewis Katz School of Medicine, Temple University

©

by

Yilin Wu

August, 2019

All Rights Reserved

ABSTRACT**MATHEMATICAL MODELS OF BIOFILM IN VARIOUS
ENVIRONMENTS**

Yilin Wu

DOCTOR OF PHILOSOPHY

Temple University, August, 2019

Professor Isaac Klapper, Chair

Microbial biofilms are defined as clusters of microbial cells living in self-produced extracellular polymeric substances (EPS), which always attached to various kinds of surfaces. In this thesis, we studied several mathematical models of biofilm in the human body and marble environment. Some related background of biofilm growth and some basic existing numerical models were introduced in the first chapter. In the first project, we introduced how biofilm affects the local oxygen concentration near the neutrophil cells in the human body with three one-dimensional reaction-diffusion models from different geometries. In nature, microbial biofilm development can be observed on almost all kinds of stone monuments and can also be associated with the problem of monument conservation. In the second part of my research, we built the deliquescence models for biofilm growth environment in the first model and added biomass into consideration in the second one. Also, we analyzed the stability of the equilibria. In the third part, we applied the weather data collected from the weather station on the roof of the Jefferson Memorial to the deliquescence model with biofilm. Furthermore, compared the simulation result for biofilm growth in cold and warm weathers. In the last part of this thesis, we analyzed the biofilm activity with support vector regression. The machine learning model we obtained can be used to find the growth trends of biofilm for any pair of temperature and relative humidity data.

ACKNOWLEDGEMENTS

First and foremost, I would like to give the deepest and most sincere gratitude possible to my advisor Prof. Isaac Klapper. He has always been very patient and enthusiastic and I have found his advice and support invaluable. I feel very fortunate and privileged for being a student of such a great mentor and mathematician. Without his coaching, this research project would have never been completed.

Besides my advisor, I would like to thank the rest of my thesis committee: Prof. Daniel Szyld, Prof. Wei-Shih Yang, Prof. Bettina Buttaro, and the Director of Graduate Studies, Prof. David Futer, for their insightful comments and encouragement, but also for the hard question which incited me to widen my research from various perspectives.

I would like to thank our collaborators Judy Jacob from National Park Service for helping me with data collection and thesis related knowledge from a workshop at Eagle Hill Institute, and Dr. Phil Stewart from Center from Biofilm Engineering at Montana State University for helping me with part of the thesis.

I would also like to thank all the Temple math faculty who I have encountered in some way or another. My passion and knowledge has grown so much in the past six years and I owe that to the professors of the classes I have taken as a graduate student at Temple. In particular, I would like to thank Prof. Benjamin Seibold and Prof. Yury Grabovsky for all the analysis and applied math I learned from them.

I would like to thank my friends, Dr. Shumo Cui, Dr. Giordano Tierra Chica, Dr. Faycal Chaouqui, Dr. Francisco Villarroja for being supportive during my studies.

Finally, I would like to thank my parents and my entire family for their love and support.

I would like to dedicate my thesis to the six years in my
life spent at Temple University

TABLE OF CONTENTS

ABSTRACT	iv
ACKNOWLEDGEMENT	v
DEDICATION	vi
LIST OF FIGURES	ix
LIST OF TABLES	xv
1 INTRODUCTION	1
1.1 Background and Motivation	1
1.1.1 What are Microbes	1
1.1.2 What is biofilm?	5
1.1.3 Motivation for Biofilm Studies	6
1.2 Existing Models for Biofilm Communities	8
1.3 Main Aims and Key Results	9
2 METHODS AND RESULTS	12
2.1 Biofilm, Oxygen, and Neutrophil	12
2.1.1 Biofilm-Neutrophil System	12
2.1.2 Table of the Coefficients	15
2.1.3 Material and Methods	15
2.1.4 Numerical Simulation and Analysis	21
2.1.5 Conclusion and Discussion	30
2.2 Biofilm Modeling in Marble Environment	32
2.2.1 Biofilm on Stone	32
2.2.2 Deliquescence Process and Deliquescence Model	33
2.2.3 Deliquescence Model without Biofilm	37
2.2.4 Deliquescence Model with Biofilm	56
2.2.5 Conclusion and Discussion	70
2.3 Simulation with Time Series Data	72

2.3.1	Data Visualization	72
2.3.2	Simulation for Deliquescence Model with Biofilm . . .	75
2.3.3	Simulation for Deliquescence model with a Loss term .	79
2.3.4	Simulation for Deliquescence Model with Year-Around Data	82
2.3.5	Conclusion and Discussion	84
2.4	Data Analysis	86
2.4.1	Support Vector Machine	86
2.4.2	k-fold Cross Validation	87
2.4.3	SVR Model Result	88
2.4.4	Conclusion and Discussion	89
3	FUTURE WORK	90
	REFERENCES	92

LIST OF FIGURES

1.1	Scanning electron micrograph of a <i>staphylococcus aureus</i> biofilm on an indwelling medical device. Available from: URL:Public Domain, https://commons.wikimedia.org/w/index.php?curid=2740748	4
1.2	Stages of biofilm development, courtesy of the Montana State University Center for Biofilm Engineering, P. Dirckx.	6
2.1	1D two-layered slab geometry in which adjoining biofilm and neutrophil layers are bounded by oxygen sources on both external boundaries. One boundary is conceptualized as air and the other as host tissue. This geometry could approximate a biofilm in a dermal wound or in the airways of the lung. . . .	16
2.2	1D two-layer slab geometry in which a biofilm layer coats an impermeable surface and is covered by a second layer of neutrophils. This geometry would approximate the situation on an infected medical implant.	17
2.3	1D spherical geometry in which a biofilm core is surrounded by a concentric spherical shell of neutrophils. This geometry could approximate a biofilm aggregate in mucus or deep tissues. . .	18
2.4	Oxygen concentration profiles in slab geometry bounded by air and host tissue for five illustrative cases as detailed in Table 2.3. Figures A-E correspond to the lettered cases in the table. Position is the value of depth of the variable z , with $z > 0$ corresponding to the biofilm layer and $z < 0$ to the neutrophil layer.	24

- 2.5 Oxygen concentration within the biofilm layer for slab geometry bounded by an air and host tissue with first-order kinetics presented as a contour plot: (A) minimum concentration within the biofilm; (B) concentration at the bioiflm-neutrophil interface. Blue denotes values corresponding to hypoxia (less than 10 mm Hg oxygen); red denotes values that are oxie (greater than or equal to 10 mm Hg oxygen). Parameter values: $C_A = 200\mu m = 127.6$ mm Hg, $C_H = 40\mu m = 25.5$ mm Hg, $k_N = 0.01s^{-1}$, $k_B = 0.1s^{-1}$, $D_N = 1000\mu m^2s^{-1}$, $D_B = 1000\mu m^2s^{-1}$, h_N ranging from 10 to 1000 μm , h_B ranging from 10 to 1000 μm 25
- 2.6 Oxygen concentration profiles in slab geometry bounded by an implant and host tissue for five illustrative cases as detailed in Table 2.3. Figures A-E correspond to the lettered cases in the table. Position is the value of depth of the variable z , with $z < 0$ corresponding to the biofilm layer and $z > 0$ to the neutrophil layer. 26
- 2.7 Oxygen concentration within the biofilm layer for slab geometry bounded by an implanted and host tissue with first-order kinetics presented as a contour plot: (A) minimum concentration within the biofilm; (B) concentration at the bioiflm-neutrophil interface. Blue denotes values corresponding to hypoxia (less than 10 mm Hg oxygen); red denotes values that are oxie (greater than or equal to 10 mm Hg oxygen). Parameter values: $C_A = 200\mu m = 127.6$ mm Hg, $C_H = 40\mu m = 25.5$ mm Hg, $k_N = 0.01s^{-1}$, $k_B = 0.1s^{-1}$, $D_N = 1000\mu m^2s^{-1}$, $D_B = 1000\mu m^2s^{-1}$, h_N ranging from 10 to 1000 μm , h_B ranging from 10 to 1000 μm 27
- 2.8 Oxygen concentration profiles in spherical geometry for five illustrative cases as detailed in table 2.3. Figures A-E correspond to the lettered cases in the table. Position is the value of depth of the variable r 28
- 2.9 Oxygen concentration within the biofilm layer for spherical geometry with first-order kinetics presented as a contour plot: (A) minimum concentration within the biofilm; (B) concentration at the bioiflm-neutrophil interface. In this setting, the minima are always at the center of the composite structure. Blue denotes values corresponding to hypoxia (less than 10 mm Hg oxygen); red denotes values that are oxie (greater than or equal to 10 mm Hg oxygen). Parameter values: $C_A = 200\mu m = 127.6$ mm Hg, $C_H = 40\mu m = 25.5$ mm Hg, $k_N = 0.01s^{-1}$, $k_B = 0.1s^{-1}$, $D_N = 1000\mu m^2s^{-1}$, $D_B = 1000\mu m^2s^{-1}$, h_N ranging from 10 to 1000 μm , h_B ranging from 10 to 1000 μm 29

2.10	Photos of Jefferson Memorial in 2001 (left) (Credit: David Pleacher) and 2017 (right)(Credit: George Rose/Getty Images)	32
2.11	Diagram of the interaction of salt solid with water vapor in the atmosphere with different relative humidity values, where RH_0 = deliquescence relative humidity and RH = atmosphere relative humidity. When $RH < RH_0$, salt adsorb minimal amounts of moisture at surfaces. Upon increasing the RH to RH_0 , more vapor is adsorbed at the surface, and the salt will dissolve until saturation is reached.	36
2.12	Three-layered dynamics of air, liquid, and salt/stone. Water condensation and evaporation happen at the air-liquid interface, while salt dissolution and precipitation occur at the salt/stone-liquid interface. Biofilm exists on the salt layer and immersed in the solution. The cartoon is demonstrating the phase changes and is not drawn to scale.	37
2.13	Phase portrait of the equation at $RH = RH_0$, and the nullclines of the two odes coincide. There are infinitely many equilibrium points, and all the equilibrium points satisfy the linear relation $m_s^{eq} = \frac{C_s m_w^{eq}}{\rho_0}$ (marked on the red line).	46
2.14	Phase portrait of the equilibrium case when $RH = 0.95 > RH_0$, the red dot is the equilibrium solution. In this case, at the equilibrium, all the available salt dissolved in the solution and the m_w^{eq} depends on the RH (0.95 in the simulation). The left figure shows the streamline on the domain $([0, 30] \times [0, 10])$ ($m_s^{max} = 10$), while the right one shows the vector field near the equilibrium point. All the streamlines go towards the red dot.	47
2.15	Phase portrait of the equilibrium case when $RH = 0 < RH_0$, $m_w^{eq} = 0$ and $m_s^{eq} = 0$ is the singular point of the system. In this case, there is no water in the system, and all the salt is in the solid phase. The left figure shows the streamline on the domain $([0, 10] \times [0, 10])$ ($m_s^{max} = 10$), while the right one shows the vector field near the singular point. All the vectors approach (0,0)	48
2.16	The phase portrait with streamlines for equation (2.39) and (2.40). If we put the initial points close enough around the origin, the points will converge to the equilibrium point eventually. Therefore, in the critical RH case, the system is stable. The mass of water and the mass of salt will come back to the red line in figure (2.13)	51

2.17	The phase portrait with streamlines for the above ODE system of \tilde{m}_s and \tilde{m}_w . If we perturbed the solutions close enough to the origin, the perturbation converges to zero. Therefore, the system is stable at high RH, and the perturbation around the equilibria will converge to the red dot (equilibrium point) in Figure (2.14)	52
2.18	Water mass (left) and salt mass (right). Parameters: see table 2.4 and $RH = 90\% > RH_0$. Initial condition: $m_w = 0.1kg$, $m_s = 0.1kg$. Since the actual RH is greater than RH_0 , water mass and salt mass increase in time. All the available salt in the system dissolves into the water and water vapor condenses into the solution to reach the equilibrium point for high RH. .	54
2.19	Water mass (left) and salt mass (right). Parameters: see table 2.4 and $RH = 40\% < RH_0$. Initial condition: $m_w = 0.1kg$, $m_s = 0.1kg$. When the actual RH is lower than RH_0 , both of the masses decrease to zero (the singular point) in time. Salt precipitates into solid phase and water in the solution evaporates into the air.	55
2.20	Comparison of bare marble and biofilm covering marble	56
2.21	Plot of water mass, salt mass, and biomass. Parameters: see table (2.4), $\eta = 10^{-6}$, $N = 1$ and $RH = 90\% > RH_0$. Initial conditions: $m_w = 0.1kg$, $m_s = 0.1kg$, $m_b = 0.1$. The water and salt masses increase to the equilibrium, all the available salt dissolves into the solution, and biomass reaches the carrying capacity.	68
2.22	Plot of water mass, salt mass, and biomass. Parameters: see table (2.4), $\eta = 10^{-6}$, $N = 1$ and $RH = 50\% < RH_0$. Initial conditions: $m_w = 0.1kg$, $m_s = 0.1kg$, $m_b = 0.1$. The actual RH is lower than RH_0 for the model without biofilm, which is also lower than RH_0 for the model with biofilm. The mass of water and the mass of salt decrease to zero in time, and biofilm stops growing once the mass of water hits zero. The salt precipitates into solid phase and the water in the solution evaporates into the air.	69
2.23	ibuttons (left) and one of the ibuttons on the roof of JM (right). ibuttons recorded temperature and humidity of the air near the marble.	72
2.24	Light sensor (left : <i>LI-190R Quantum Sensor</i>) and rain gauge (middle and right : <i>RG3 Onset Hobo Rain Gauge Data Logger</i>) measured light intensity and precipitation on the roof.	73

2.25	Plot with sample date selected in summer (07/23/2016-07/27/2016). (Black) Relative humidity and (blue) temperature. Red blocks in the plot represent high light intensity ($>500\mu\text{mol} \cdot \text{m}^{-2} \cdot \text{s}^{-1}$), and the blue block in the plot represents activity of rain gauge, which means we have precipitation during that period. To check the validity of the data we collected from the rain gauge, we compared with the weather data collected by the National Oceanic and Atmospheric Administration (NOAA). During this time (07/23/2016-07/27/2016), there was a thunderstorm starting at midnight on 07/24/2016 which verifies our data.	73
2.26	Plot with sample date selected in winter (02/02/2016-02/06/2016). (Black) Relative humidity and (blue) temperature. Red blocks in the plot represent high light intensity ($>500\mu\text{mol} \cdot \text{m}^{-2} \cdot \text{s}^{-1}$), and the blue block in the plot represents activity of rain gauge, which means we have precipitation during that period. Checking with the weather data collected by the National Oceanic and Atmospheric Administration (NOAA), we had rain on 02/03/2016, which validates the correctness of our data. Notice that there is a sudden drop in relative humidity on 02/04/2016. This irregularity might be attributed to the inaccuracy of a rain-soaked button.	74
2.27	Summer data used for simulation.	75
2.28	Water mass (top), salt mass (middle), and biomass (bottom). Parameters: $\eta = 10^{-6}$ and $N = 1\text{kg}$. Initial conditions: $m_w = 0.1\text{kg}$, $m_s = 0.1\text{kg}$, $m_b = 0.1\text{kg}$, Time period: 2016/07/13-2016/8/11.	76
2.29	Water mass (top), salt mass (middle), and biomass (bottom). Parameters: $\eta = 10^{-6}$ and $N = 1\text{kg}$. Initial conditions: $m_w = 0.1\text{kg}$, $m_s = 0.1\text{kg}$, $m_b = 0.1\text{kg}$. Data: duplicated the temperature and RH data from figure 2.27 three times.	76
2.30	Winter data used for simulation.	77
2.31	Water mass (top), salt mass (middle), and biomass (bottom). Parameters: $\eta = 10^{-6}$ and $N = 1\text{kg}$. Initial conditions: $m_w = 0.1\text{kg}$, $m_s = 0.1\text{kg}$, $m_b = 0.1\text{kg}$, Time period: 2016/01/21-2016/02/19.	77
2.32	Water mass (top), salt mass (middle), and biomass (bottom). Parameters: $\eta = 10^{-6}$ and $N = 1\text{kg}$. Initial conditions: $m_w = 0.1\text{kg}$, $m_s = 0.1\text{kg}$, $m_b = 0.1\text{kg}$, Data: duplicated the temperature and RH data from figure 2.30 three times.	78

2.33	Water mass (top), salt mass (middle), and biomass (bottom). Parameters: $\eta = 10^{-6}$, $d = 1.5 \times 10^{-7}$, and $N = 1kg$. Initial conditions: $m_w = 0.1kg$, $m_s = 0.1kg$, and $m_b = 0.1$. Time period: 2016/07/13-2016/8/11.	80
2.34	Water mass (top), salt mass (middle), and biomass (bottom). Parameters: $\eta = 10^{-6}$, $d = 1.5 \times 10^{-7}$, and $N = 1kg$. Initial conditions: $m_w = 0.1kg$, $m_s = 0.1kg$, and $m_b = 0.1$. Data: duplicated the temperature and RH data from figure 2.27 60 times (five years).	80
2.35	Water mass (top), salt mass (middle), and biomass (bottom). Parameters: $\eta = 10^{-6}$, $d = 1.5 \times 10^{-7}$, and $N = 1kg$. Initial conditions: $m_w = 0.1kg$, $m_s = 0.1kg$, and $m_b = 0.1$. Time period: 2016/01/21-2016/02/19.	81
2.36	Water mass (top), salt mass (middle), and biomass (bottom). Parameters: $\eta = 10^{-6}$, $d = 1.5 \times 10^{-7}$, and $N = 1kg$. Initial conditions: $m_w = 0.1kg$, $m_s = 0.1kg$, and $m_b = 0.1$. Data: duplicated the temperature and RH data from figure 2.30 60 times (five years).	81
2.37	Water mass (top), salt mass (middle), and biomass (bottom). Parameters: $\eta = 10^{-6}$, $d = 1.5 \times 10^{-7}$, and $N = 1kg$. Initial conditions: $m_w = 0.1kg$, $m_s = 0.1kg$, and $m_b = 0.1$. Data Period: 05/20/2015-05/20/2016. From the plot, biofilm grows faster in the winter than in the summer.	83
2.38	Water mass (top), salt mass (middle), and biomass (bottom). Parameters: $\eta = 10^{-6}$, $d = 1.5 \times 10^{-7}$, and $N = 1kg$. Initial conditions: $m_w = 0.1kg$, $m_s = 0.1kg$, and $m_b = 0.1$. Data: duplicated the temperature and RH data for the entire year 5 times (five years). Overall, biomass increases in winters and decreases in summers.	84
2.39	Black samples are time series data, the red and blue plane is the regression hyperplane (2D in this case). We trained the data with optimized hyperparameters and k-fold cross valida- tion with $k = 5$. There are some outliers at $RH = 1$, which are statistical errors of the model.	88
2.40	Actitivity of biofilm. Samples in red are active and in blue are inactive. The boundary is $RH = -0.03T + 6$. When $RH >$ $-0.03T + 0.6$, biomass increases and conversely, decreases. . .	89

LIST OF TABLES

1.1	Table of Different Type of Bacteria [5]	3
2.1	Table of Coefficients	15
2.2	Parameter Values	22
2.3	Parameter values for simulations	23
2.4	List of Parameters	42
2.5	Possible Dissoluble Chemical Salts on Marble	44

CHAPTER 1

INTRODUCTION

1.1 Background and Motivation

Before commencing with an outline for the thesis, we first present some background into the existence of a biofilm by introducing the formation, the basic architecture of biofilm communities, and some motivations for biofilm studies.

1.1.1 What are Microbes

Microbe, is a microscopic organism, which may exist in its single-celled form or in a colony of cells. Microbes include all unicellular organisms and so are extremely diverse. Of the three domains of life identified by Carl Woese[123], all of the Archaea and Bacteria are microorganisms. These were previously grouped together in the two domain system as Prokaryotes, the other being the eukaryotes. Prokaryotes is simpler than Eukaryota as there is no nucleus in the cell structure. Microbes are found in every habitat on earth, such as soil, rock, oceans and even arctic snow. Some live in or on other organisms including plants and animals including human beings. In 2016, researchers from Weizmann institute in Isreal argued that there is about 1.3 bacterial cells per human cell [104]. These numbers may vary significantly from person to person

and could change significantly with each defecation [104]. A lot of bacterial cells are found in the digestive system of animals, and are known as gut bacteria. Gut bacteria have several roles. For example, gut bacteria can produce vitamin B_1 , control the growth of harmful bacteria, break down poisons in the large intestine, and also break down the food that cannot be digested [72]. Bacteria in soil perform important services related to water dynamics, nutrient cycling, and disease suppression [34]. Moreover, some bacteria can break down pesticides and pollutants in soil [16]. Some types of bacteria are useful in the production of fermented foods such as yogurt and soy sauce [83]. These kind of bacteria are known as fermenting bacteria, and they use organic molecules as their final electron acceptor to produce fermentation end-products [48]. For example, *Streptococcus*, *Lactobacillus*, and *Bacillus* can produce lactic acid, while *Escherichia* and *Salmonella* produce ethanol, lactic acid, succinic acid, acetic acid, CO_2 , and H_2 .

Bacteria are thought to have been the first organisms to appear on earth more than 3 billion years ago [4], and the oldest known fossils look like bacterial colonies [101]. Bacteria can use most organic, and some inorganic compounds as food and some can survive extreme conditions [96]. Some bacteria can form dormant structures, known as endospores, which are resistant to hostile physical and chemical conditions such as heat, UV radiation, and disinfectants. Bacteria may grow across a wide range of temperatures, from very cold to very hot, although all bacteria have their optimal environmental surroundings and temperatures in which they thrive the most [81]. Some bacteria grow best around moderate temperature and neutral pH values (6.5 - 7.0), but some thrive in very acid conditions, and some can even tolerate a pH as low as 1.0 [99]. Such acid-loving microbes are called *acidophiles*. Many natural habitats for microbes have high pH. Marine bacteria grow in alkaline marine environments at pH 8.2 [46] and other bacteria spend part of their life cycle in marine environments, where they must survive or grow [97]. Even though they can live in very acid or alkaline environments, their internal pH is much closer to neutral values [3, 8]. Besides the suitable environmental conditions,

bacteria must have an energy source and carbon source to grow in nature. The energy sources for bacteria includes light, inorganic compounds, and organic compounds, and the carbon sources for bacteria includes CO_2 , and organic compounds. Different types of bacteria have different energy sources. For example, phototrophs are organisms that use light as an energy sources and CO_2 as a carbon source; heterotrophs are organisms that use organic compounds as an energy source and carbon source. Thus, based on carbon and energy sources for growth, four major nutritional types of bacteria may be defined in Table 1.1 [5]. This classification of bacteria provides a natural approach to study bacteria growth with different energy and carbon sources conditions.

Table 1.1: Table of Different Type of Bacteria [5]

Nutritional Type	Energy Source	Carbon Source	Example
Photoautotrophs	Light	CO_2	Cyanobacteria
Photoheterotrophs	Light	Organic compounds	Purple and Green Bacteria
Lithoautotrophs	Inorganic compounds (NH_3 , NO_2)	CO_2	nitrifying bacteria
Heterotrophs	Organic compounds	Organic compounds	non-sulfur bacteria

In order to survive and to increase tolerance, e.g., from predators or wash off, bacteria tend to be found in a community where they can better maintain the surrounding living environment. It is often stated that there is strength in numbers. In some cases it is pure power, while in many other examples, the benefit of numbers derives from the fact that larger groups of individuals can divide tasks, thereby allowing them to diversify into teams of coordinated

specialists that can accomplish more together than the simple sum of their parts [131]. Furthermore, microbial activity within the community can modify the internal environment, such as pH, CO_2 or metabolic products [95]. For example, Burmolle et al. [12] showed that a mixed species bacterial community has significantly more biomass than the monospecies community without up taking more nutrients. They also observed that such diverse communities have a higher tolerance to antimicrobials, chemical stress, and predators. Hence, the cooperation within bacteria groups can be mutually beneficial and significant competitive advantage over bacteria growing in suspension. Bacteria in suspension can be washed away with the water flow, but bacteria in the community are protected from washout and can build in locations where their food supply remains abundant. The community formed by same or different species tends to attach on a surface to maintain physical stability, and can create natural polymers (EPS, explained later in this chapter). For the above reasons, bacteria living on a surface (shown in Figure 1.1) have a large advantage for surviving. The community bacteria created is known as biofilm.

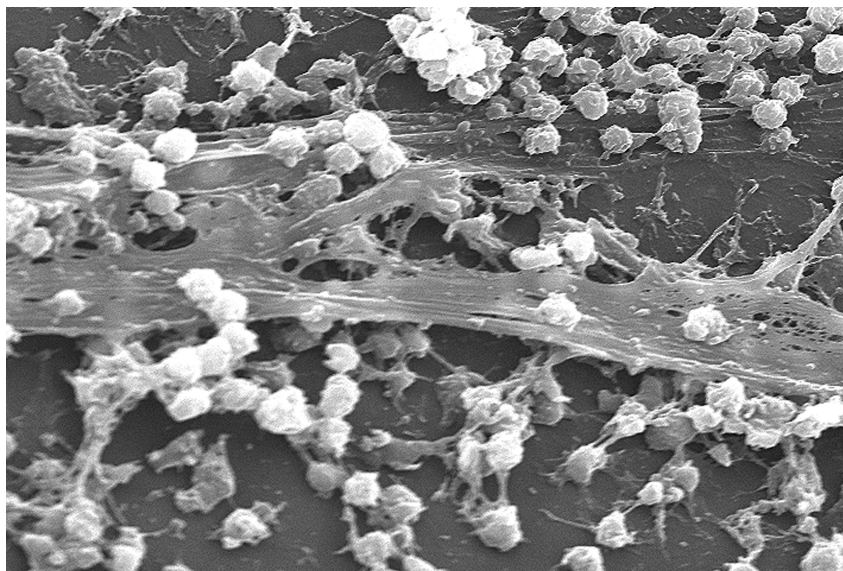


Figure 1.1: Scanning electron micrograph of a *staphylococcus aureus* biofilm on an indwelling medical device. Available from: URL:Public Domain, <https://commons.wikimedia.org/w/index.php?curid=2740748>

1.1.2 What is biofilm?

Bacterial biofilms are defined as clusters of microbial cells living in self-produced extracellular polymeric substances (EPS) which attach to various kinds of surfaces, such as metals, plastics, soil particles, medical implant materials and human or animal tissue [58]. Accumulation of microorganisms were observed as early as 1674, when Antonie van Leeuwenhoek used his simple microscope to describe the vast accumulation of animalcules that he scraped from human tooth surfaces [21]. In the 1940s, Heukelekain, Heller [50] and Zobell [133] observed that the density of bacteria on surfaces was much higher than in the surrounding medium (in their cases, seawater). The earliest use of biofilm in publication is 1975 from the journal *Microbial Ecology* [74]. However, we did not have a high - resolution picture of the 3d structure of biofilm until the invention of the confocal microscope.

Biofilms can be formed of a population that developed from a single species or a community derived from multiple microbial species [21]. The formation of a biofilm starts with the attachment of free-floating microorganisms to a surface. If the colonists are not immediately separated from the attached surface, they can anchor themselves using adhesive slimy [61]. Some bacteria species are not able to attach to a surface by themselves but can anchor themselves to the matrix or earlier bacteria colonists. Once colonization has begun, the biofilm grows by a combination of cell division and attraction of other species. The final stage of biofilm formation is known as dispersion and is the stage in which dispersal of cells happens. Dispersal enables biofilms to spread and colonize on new surfaces. Following this pattern, biofilm grows and is hard to eliminate from the colonized surfaces (See chapter 2.2 for an example).

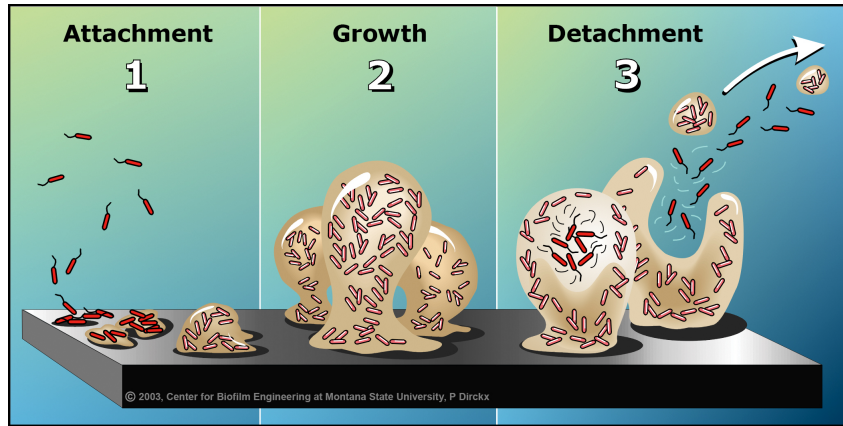


Figure 1.2: Stages of biofilm development, courtesy of the Montana State University Center for Biofilm Engineering, P. Dirckx.

In essence, biofilm represents an interdependent community-based existence.

1.1.3 Motivation for Biofilm Studies

There are different types of biofilms which are playing a distinct role in our life. Approximately 80% of the world's microbial biomass resides as biofilm populations and the formation and persistence of biofilms may cause human infections [24].

Some biofilms provide valuable services to human society or the functioning of natural ecosystems. People started to use biofilm as a tool for wastewater treatment and contaminant removal (from soil or groundwater) since the end of the 19th century. Also, the biochemical byproducts from biofilms are useful in the production of medicines, food additives and cleaning agents, see, [43, 47, 105, 111]. Moreover, biofilm can attach to the root system of the plants to increase the flow of nutrients transportation, and increase agricultural productivity.

Some biofilms can pose a potential threat to humans and surfaces. In dentistry, biofilms cause major problems in dental hygiene. Oral biofilms serve as a model system for bacterial adhesion [10, 13] and antibiotic resistance [129].

Biofilm may also cause infectious diseases and infections related to medical implants. According to recent data from the National Institutes of Health, biofilms cause more than 75% of all microbial infections [94] and the top two causes of death, chronic diseases, and poor water quality are highly related to biofilms [122]. In the food industry, biofilm may cause serious engineering problems. Biofilm grown on food surfaces and in processing environment can cross-contaminate, and may lead to biotransfer potential if the biofilm from food-contact surfaces is not completely removed [69]. Examples of cross-contamination are found in the milk [17] and the slaughter [87] industries.

As one can see from the above examples, biofilm is everywhere and is crucial to human beings. Therefore the study of microbial biofilms has received significant attention and achieved substantial popularity in the past few decades. Understanding the mechanisms of biofilm formation, growth, and removal is the key to promoting useful biofilms and reducing unacceptable functions of the biofilm. The study of biofilms benefits from the efforts of researchers from various fields, including environmental and clinical biologists, engineers, and mathematicians, and people from different areas are working together to have a better and more precise understanding of nature. Mathematical modeling is one of the significant ways to interpret how bacteria in biofilm collaborate, how biofilm grows and what it does for the attached surfaces and surrounding environment. Using mathematical models, we can understand the fundamental mechanisms of biofilm, relate different systems, and make predictions for the long term.

To model biofilm, we are essentially trying to study the following problems.

- How fast biofilm grows on a given surface with a particular environment?
- Why and how biofilm started to colonize on certain surfaces?
- How does the division of labor work between different species of bacteria in one community?
- What biofilm will do to the surrounding environment, e.g., erosion or

pollution?

1.2 Existing Models for Biofilm Communities

The first mechanistically-based modeling of biofilm was developed in 1976 by Williamson and McCarty [120], and this model describes the kinetics of substrate utilization by biofilm using Fick's law and Monod relationship. After that, biofilm researchers started to do experimental measurements which enabled the detailed analysis of microbial communities with mathematical models. Today, mathematical models come in many forms that can range from simple empirical correlations to complicated and computationally comprehensive algorithms that can describe biofilm formation and activity. Many published articles give an overview of mathematical models for biofilm in general, see [15, 51, 61, 119].

Mainly there are two types of mathematical models, and different methodologies may have the advantages in different situations depending on the mechanisms we model. The first type of models is continuum models based on ordinary differential equations (ODE) and partial differential equations (PDE). In such a model, the biofilm is described as a penetrable material that allows mass exchanges, reaction, and diffusion between biofilm and surrounding liquid or solid layers. Several strategies can be used to describe the spatial structure of biofilm in this context. In some PDE (ODE) models, biofilm and liquid are separated by a physical interface, the evolution of which is computed by moving front techniques [1, 60]. There is another modeling strategy which is using mixture theory introduced by Trusdell et al. [115] in the 1960s. This method provides continuous models based on PDEs for multi-component fluids by assuming that several components may be present locally. For more details about mixture theory, see [18, 93, 92]

The second approach of biofilm modelling uses discrete models, such as cellular automaton (CA) models [49, 82, 89, 121], and individual-based models (IBM) [67, 68, 70]. The origins of the CA model is Conway's Game of Life [20].

The advantage of the CA model is that it can produce a complex behavior for bacteria reproduction and movement, and the diffusion of the nutrient with simple rules. IBM is also a discrete approach that it attempts to model a population or community by describing the actions and properties of the individuals comprising the population or community. IBM is particularly suited to address questions about the effects of individual variability. However, fluid dynamics effects are challenging to take into account for discrete models, and the computational cost for simulating the evolution of a large number of cells are quite expensive even with the recent advances in parallel computing.

1.3 Main Aims and Key Results

In my thesis, I will introduce four different biofilm-related projects on which I worked with biofilm researchers from various fields. In these four projects, I applied two continuous models (ODE and PDE), data visualization, and data analysis.

For the first part of the thesis, we introduce how biofilm affects the local oxygen concentration near the neutrophil cells in the human body with three one-dimensional reaction-diffusion models from different geometries. These three models were analyzed approximating biofilm near an air interface as in a dermal wound or mucus layer, biofilm on an implanted medical device, or biofilm aggregates dispersed in mucus or tissue. The models derived in this project are in simple geometries and can be solved analytically. Also, models are clearly simplifications of reality. For each of the models, we simulated the oxygen level at the biofilm-neutrophil interface or within the biofilm layer with sets of plausible parameters. The finding that oxygen concentration at the biofilm-neutrophil juncture can be diminished to hypoxic (absence of oxygen) levels is biologically relevant because oxygen depletion will reduce the neutrophil killing ability. The conclusion that hypoxia can readily establish in the interior of the biofilm is biologically relevant because this change will alter microbial metabolism and persistence. Therefore understanding how biofilms

quantitatively influence the oxygen concentration is necessary. This paper was published in *Pathogens and Disease* in 2018 [125] and chapter 2.1 of the thesis is excerpted from that paper. My role in this paper was to solve three one-dimensional reaction-diffusion models analytically, and do the simulation for oxygen concentration with line and contour plots.

In nature, microbial biofilm development can be observed on almost all kinds of stone monuments such as churches, tombstones, and temples, and can also be associated with the problem of monument conservation. In the second part of my research, I focus on biofilm growth on outdoor marble monuments. For this research project, the monument we are particularly studying is Jefferson Memorial (JM) in Washington, DC. Biofilm was first noticeable in discrete areas of the JM's white marble in 2006 and has become more pronounced in recent years. The National Park Service have been studying the best treatment options to eliminate the dark spots on the marble dome to reveal the purely marble dome again. We are still not sure about whether biofilm is protecting or damaging the marble in this context. Therefore, we use a mathematical model to give us a better understanding of why and how biofilm is growing in this environment. We first develop a deliquescence model which contains a coupled system for mass fluxes of water and salt on the marble, which describes the suitable growing environment for biofilm. After that, we add biomass into the model to connect biofilm photosynthesis with its living surroundings. The deliquescence model with biofilm gives us a general idea of the relation of biofilm growth rate and water depletion rate. In this model, we also find a critical relative humidity of salt mathematically instead of experimental measurements and compare the values we got with the existing data from experiments. This critical relative humidity determines when deliquescence happens under different humidity conditions.

During our studies on the JM, we had a weather station set on top of the monument, from which we collect year-around weather data, including temperature, humidity, precipitation, and sunlight intensity. For the third part of my thesis, I study the time series data we collect from the JM and apply

the deliquescence model we derive from the second project. We simulate with the data from 28 days in the summer and 28 days in the winter, and compare the biomass between such two different kinds of weather. We further develop a modified deliquescence model with the loss term in biomass and apply the previous data to this model for a longer time. In the end, we simulate with year-around data to verify the result of biofilm growth from the deliquescence model in different weather.

In the last project, we analyze biofilm growth with different temperature and relative humidity data to predict the biofilm growth rate with any pair of temperature and relative humidity data. After running year-around data with the model, we obtain the biomass and growth rate at each data point. After the simulation, we have three-dimensional data of relative humidity, temperature, and biofilm growth rate. Using support vector regression from machine learning, we create a two-dimensional plane which minimized the model error. On this plane, we create a region of biofilm activity with a linear boundary. This can be used to predict the growth rate of biofilm. When we have the ideal temperature and humidity in the biofilm living environment, the biofilm starts to grow, and if one of the conditions fails, the biofilm stops growing.

CHAPTER 2

METHODS AND RESULTS

2.1 Biofilm, Oxygen, and Neutrophil

2.1.1 Biofilm-Neutrophil System

Biofilms exist on the surface of living organisms where they may consume oxygen. In the biofilm state, microbes evade killing by antibiotics and by the host defenses [22, 27]. Examples of infections that are now widely acknowledged to stem from biofilms include periodontitis or gum disease [90], chronic lung infection in individuals with cystic fibrosis (CF) [22, 73], chronic wounds such as diabetic foot ulcers, pressure ulcers and venous stasis ulcers [7, 54]; and troublesome infections associated with implanted medical devices such as catheters [86, 80], heart valves [52] and artificial joints [40]. Biofilm formation is thus a common microbial strategy that is considered a virulence factor in numerous persistent infections [22].

A nearly universal feature of microbial biofilms in oxic environment is an oxygen concentration gradient [126, 108]. Respiring microbes at the surface of the biofilm consume oxygen creating an oxygen shadow that alters microbial metabolism and allows for the coexistence of aerobic and anaerobic microorganisms in close proximity. Multiple lines of evidence indicate oxygen limitation and a shift to anaerobic metabolism in biofilm infections. Here we

focus discussion on CF pneumonia and chronic wounds.

One of the most compelling pieces of evidence for hypoxia in infected non-healing wounds is the identification of strictly anaerobic bacteria, such as those belonging to the genera *Bacteroides* and *Clostridia*, which are commonly found in human chronic wounds [28, 35, 36, 45, 91]. The presence of these microorganisms, which require highly reduced conditions to be able to multiply, shows that anoxic niches occur in these infected tissues. In addition, direct measurement of very low skin tissue oxygenation in the vicinity of chronic wounds has been reported and shown to correlate with impaired healing [57, 98]. Neutrophils are known to be abundant in chronic ulcers [25].

The lung is a well-aerated environment. In the CF lung, however, thickened mucus and deficient mucociliary clearance combine to permit overgrowth of bacteria and localized depletion of oxygen. Invading neutrophils, the predominant inflammatory cells [29] consumes oxygen as do the bacteria [64]. Anoxic pockets within the infected mucosa [124] or freshly expectorated infected sputum [65, 23] have been directly measured using oxygen microelectrodes. Recent investigation also report the recovery of large numbers of anaerobic bacteria from the airways of CF patients when appropriate techniques are employed [116, 130, 106, 44]. These chemical and biological measurements are consistent with hypoxic conditions within the lung mucus layer. Even the paradigm CF pneumonia organism *Pseudomonas aeruginosa*, widely understood to prefer aerobic growth conditions, is now thought to grow under microaerobic or anaerobic conditions in *vivo* in the CF lung. Oxygen limitation and a shift to anaerobic metabolism are hallmarks of biofilm infection [110].

Oxygen concentration is a critical parameter for host healing [102, 103], neutrophil function and signaling [114, 128, 75, 62, 37, 14], and microbial persistence [9, 33, 59, 100, 42]. We hypothesize that local oxygen concentration plays a fundamental role in the etiology of biofilm infection. Both host and microbe consume oxygen, modulate oxygen transport and actively respond to oxygen, giving rise to complex interactions with multiple feedback loops [55, 56, 14, 114]. The purpose of the work reported here is to provide a starting

place for analyzing the concerted utilization of oxygen by microorganisms in a biofilm and neutrophils responding to the microbial aggregate. This work expands on many years of reaction-diffusion modeling in the biofilm field [71] as well as on computational models of host cell-microbe interactions [85]. In this project, we report analysis of reaction-diffusion problems in which biofilm and neutrophil regions adjoin each other without intermixing or overlapping. The models derived herein are geometrically simple and afford analytic solutions. Such models are clearly simplifications of reality. They do not incorporate multidimensional structures, mixed species interactions or external flows, all features that are known to occur in some biofilm systems and aspects that have been addressed in pioneering biofilm modeling work [88, 19, 1, 30]. Here we extend classic biofilm reaction-diffusion models to include host interactions in the form of an adjoining neutrophil layer. To the best of our knowledge, this project is the first example of a reaction-diffusion analysis of a hybrid biofilm-neutrophil system. The value of analytical models as a starting point is that they can define overall behaviors of the system and point to likely biological relevance without introducing extra complexity. This project was published in *Pathogens and Disease* in 2018 [125] and this part of the thesis is excerpted from that paper. My role in this project was to solve three one-dimensional reaction-diffusion models analytically (Chapter 2.1.3), and do the simulation for oxygen concentration with line and contour plots (Chapter 2.1.4) with parameters and geometries provided by Dr. Phil Stewart and my advisor Dr. Isaac Klapper.

2.1.2 Table of the Coefficients

Table 2.1: Table of Coefficients

C_A	oxygen concentration on biofilm-air boundary
C_B	oxygen concentration in biofilm region
C_H	oxygen concentration on biofilm-host boundary
C_N	oxygen concentration in neutrophil region
D_B	effective diffusion coefficient of oxygen in biofilm region
D_N	effective diffusion coefficient of oxygen in neutrophil region
h_B	slab thickness of biofilm region
h_N	slab thickness of neutrophil region
k_B	first-order oxygen reaction rate coefficient in biofilm region
k_N	first-order oxygen reaction rate coefficient in neutrophil region
r	spatial coordinate in spherical coordinates
R	combined radius of biofilm and neutrophil regions
r_B	radius of biofilm region
r_N	dimension of radial shell describing neutrophil regions
z	spatial coordinate in slab geometry
ϕ_B	biofilm region Thiele modulus
ϕ_N	neutrophil region Thiele modulus

2.1.3 Material and Methods

We analyze theoretically three simple geometries that may approximate the distribution of biofilm [7] and neutrophils in *vivo* (shown in Figure 2.1, 2.2, and 2.3). A classic model of biofilm structure is the flat slab, and here we allow for an adjoining layer containing neutrophils to create a two-layered slab structure in Figure 2.1. Such a disjoint layered structure is suggested by some microscopic observations [25, 66, 132]. For a mucosal or dermal biofilm, one

boundary of the biofilm will be an air interface and the other will be in tissue. Thus, we imposed specific oxygen concentrations along these boundaries. An implanted medical device constitutes a special case of the two layered slab. In this case the biofilm is assumed to form a layer on the implant surface and is covered by a neutrophil-containing layer (shown in Figure 2.2). The implant is assumed to be impermeable to oxygen so that a no-flux boundary condition is imposed at this boundary. Recent discussions of the structure of the infectious biofilms suggest that biofilms are often found as relatively small aggregates of microbial cells intermixed or covered with extensive host-derived material [6, 109]. To capture this structure, concentric spheres (at the core) and neutrophils (in a shell) are considered (shown in Figure 2.3). Simplified geometric models can often present the overall behavior of complex systems [2].

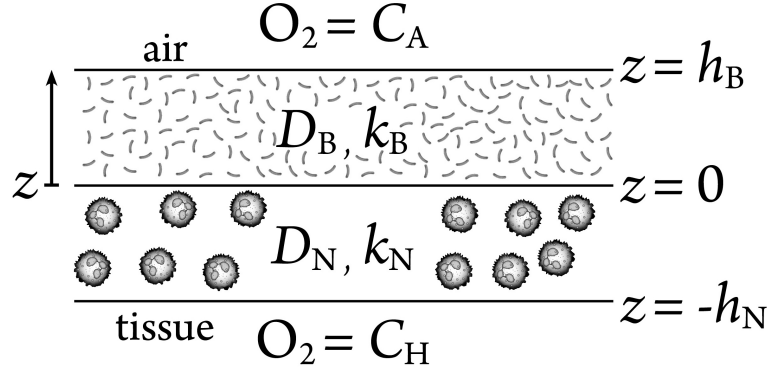


Figure 2.1: 1D two-layered slab geometry in which adjoining biofilm and neutrophil layers are bounded by oxygen sources on both external boundaries. One boundary is conceptualized as air and the other as host tissue. This geometry could approximate a biofilm in a dermal wound or in the airways of the lung.

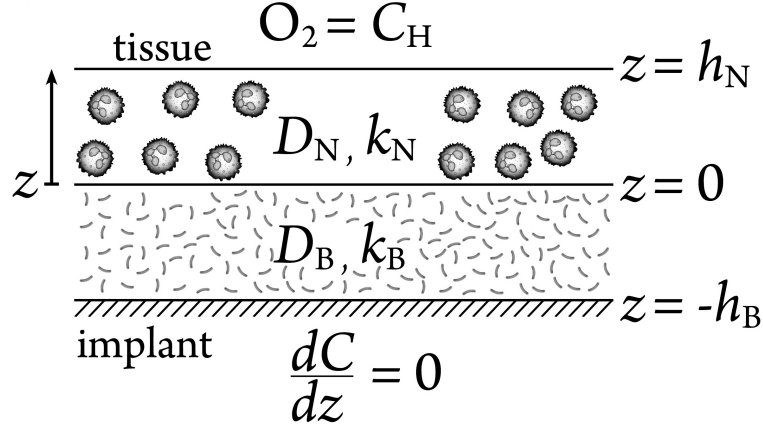


Figure 2.2: 1D two-layer slab geometry in which a biofilm layer coats an impermeable surface and is covered by a second layer of neutrophils. This geometry would approximate the situation on an infected medical implant.

First-order reaction kinetics of oxygen have been assumed for the consumption of oxygen by both bacteria and neutrophils. This is partly done for mathematical convenience as it permits exact analytical solutions. First-order kinetics provide a bound on the behavior expected from a more realistic saturation kinetic models such as Monod kinetics. The first-order approximation of saturation kinetics leads to the maximum extent of oxygen penetration. Thus, we anticipate that the actual occurrence of hypoxia will be more common and more severe than the current analysis predicts. Our results can be viewed as a conservative estimation of the importance of hypoxia in biofilm-host interactions.

Consider the steady-state reaction-diffusion equations in a two-layered slab

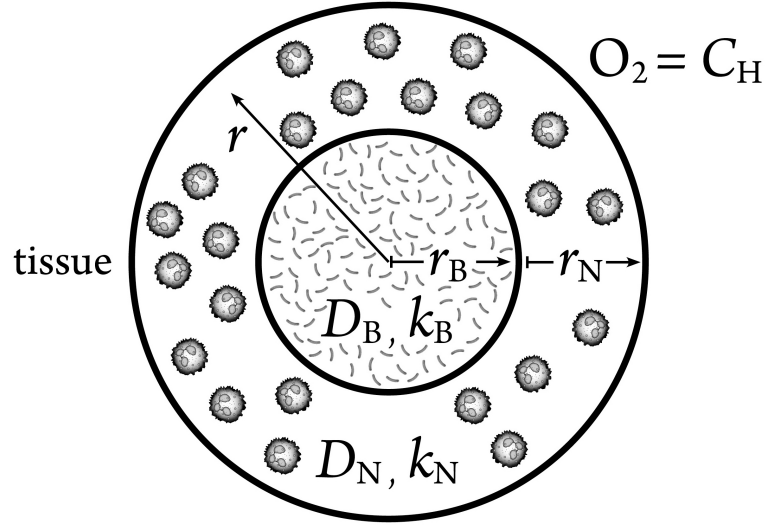


Figure 2.3: 1D spherical geometry in which a biofilm core is surrounded by a concentric spherical shell of neutrophils. This geometry could approximate a biofilm aggregate in mucus or deep tissues.

(Figure 2.1 and 2.2). We have

$$D_B \frac{d^2 C_B}{dz^2} - k_B C_B = 0, \quad (2.1)$$

$$D_N \frac{d^2 C_N}{dz^2} - k_N C_N = 0, \quad (2.2)$$

with interface conditions,

$$C_B(0) = C_N(0), \quad (2.3)$$

$$D_B \frac{dC_B}{dz}(0) = D_N \frac{dC_N}{dz}(0). \quad (2.4)$$

The interface conditions subject to the continuity of oxygen concentration (Eqn 2.3) and flux (Eqn 2.4). For the first geometry (Figure 2.1), the boundary conditions impose fixed concentrations:

$$C_B(h_B) = C_A, \quad (2.5)$$

$$C_N(-h_N) = C_H. \quad (2.6)$$

The solutions are:

$$C_N = \frac{\cosh(\phi_N \frac{z}{h_N})}{\cosh(\phi_N)} \left(\frac{C_H \alpha \tanh \phi_B + C_A \frac{\sinh \phi_N}{\cosh \phi_B}}{\alpha \tanh \phi_B + \tanh \phi_N} \right) + \frac{\sinh(\phi_N \frac{z}{h_N})}{\sinh(\phi_N)} \left(\frac{C_A \frac{\sinh \phi_N}{\cosh \phi_B} - C_H \tanh \phi_N}{\alpha \tanh \phi_B + \tanh \phi_N} \right), \quad (2.7)$$

$$C_B = \frac{\cosh(\phi_N \frac{z}{h_N})}{\cosh(\phi_B)} \left(\frac{C_H \alpha \frac{\sinh \phi_B}{\cosh \phi_N} + C_A \tanh \phi_N}{\alpha \tanh \phi_B + \tanh \phi_N} \right) + \frac{\sinh(\phi_N \frac{z}{h_N})}{\sinh(\phi_B)} \left(\frac{C_A \alpha \tanh \phi_B - C_H \alpha \frac{\sinh \phi_B}{\cosh \phi_N}}{\alpha \tanh \phi_B + \tanh \phi_N} \right), \quad (2.8)$$

where

$$\alpha = \left(\frac{k_N D_N}{k_B D_B} \right)^{1/2},$$

$$\phi_B = \left(\frac{k_B h_B^2}{D_B} \right)^{1/2},$$

$$\phi_N = \left(\frac{k_N h_N^2}{D_N} \right)^{1/2}.$$

The parameter ϕ_B and ϕ_N are dimensionless ratios of the reaction and diffusion rates known as Thiele Moduli.

For the slab structure on the surfaces of a medical devices (Figure 2.2), a no flux condition is required at the implant surface, which is assumed to be oxygen impermeable, and a fixed concentration is imposed at the interface with tissue:

$$\frac{dC_B}{dz}(-h_B) = 0, \quad (2.9)$$

$$C_N(h_N) = C_H. \quad (2.10)$$

In this case, the solutions are:

$$C_B = C_H \alpha \frac{\cosh(\phi_B \frac{z}{h_B}) + \tanh \phi_B \sinh(\phi_B \frac{z}{h_B})}{\tanh \phi_B \sinh \phi_N + \alpha \cosh \phi_N} \quad (2.11)$$

$$C_N = C_H \frac{\alpha \cosh(\phi_N \frac{z}{h_N}) + \tanh \phi_B \sinh(\phi_N \frac{z}{h_N})}{\tanh \phi_B \sinh \phi_N + \alpha \cosh \phi_N}. \quad (2.12)$$

Finally, we consider the scenario of a spherical core of microbial biofilm surrounded by a concentric shell of neutrophils (Figure 2.3). The steady state reaction-diffusion equations in spherical coordinates are:

$$\frac{1}{r^2} \frac{d}{dr} \left(r^2 D_B \frac{dC_B}{dr} \right) - k_B C_B = 0, \quad (2.13)$$

$$\frac{1}{r^2} \frac{d}{dr} \left(r^2 D_N \frac{dC_N}{dr} \right) - k_N C_N = 0, \quad (2.14)$$

with interface conditions:

$$\begin{aligned} C_B(r_B) &= C_N(r_B), \\ D_B \frac{dC_B}{dr}(r_B) &= D_N \frac{dC_N}{dr}(r_B), \end{aligned}$$

and boundary conditions:

$$\begin{aligned} C_N(r_B + r_N) &= C_H, \\ r^2 \frac{dC_B}{dr}(0) &= 0. \end{aligned}$$

The solutions are:

$$C_B = \frac{B_1 R}{r} \sinh \left(\phi_B \frac{r}{r_B} \right), \quad (2.15)$$

$$C_N = \frac{A_2 R}{r} \cosh \left(\phi_N \left(\frac{r - R}{r_N} \right) \right) + \frac{B_2 R}{r} \sinh \left(\phi_N \left(\frac{r - R}{r_N} \right) \right), \quad (2.16)$$

where

$$\begin{aligned} R &= r_B + r_N, \\ \phi_B &= \left(\frac{k_B r_B^2}{D_B} \right)^{1/2}, \\ \phi_N &= \left(\frac{k_N r_N^2}{D_N} \right)^{1/2}, \\ B_1 &= \frac{\alpha C_H}{\sinh \phi_N \sinh \phi_B \left(\frac{\alpha}{\phi_N} \frac{r_N}{r_B} - \frac{1}{\phi_B} \right) + \sinh \phi_N \cosh \phi_B + \alpha \cosh \phi_N \sinh \phi_B}, \\ A_2 &= C_H, \\ B_2 &= \frac{\alpha \sinh \phi_N \sinh \phi_B + \cosh \phi_N \cosh \phi_B + \cosh \phi_N \sinh \phi_B \left(\frac{\alpha}{\phi_N} \frac{r_N}{r_B} - \frac{1}{\phi_B} \right)}{\sinh \phi_N \sinh \phi_B \left(\frac{\alpha}{\phi_N} \frac{r_N}{r_B} - \frac{1}{\phi_B} \right) + \sinh \phi_N \cosh \phi_B + \alpha \cosh \phi_N \sinh \phi_B}. \end{aligned}$$

2.1.4 Numerical Simulation and Analysis

We calculated the spatial distribution of oxygen in systems consisting of adjoining layers of microbial biofilm and host neutrophils. Because both microorganisms and activated neutrophils consume oxygen, their concerted activity determines the local availability of oxygen. Of particular interest is the concentration of oxygen at the interface between the biofilm and neutrophil layers. The availability of oxygen at this juncture is likely important for the ability of neutrophils to exhibit microbiocidal activity and is the relevant concentration for this aspect since this is where the neutrophils contact microorganisms. We also examine the lowest concentration of oxygen within the biofilm layer, a minimum that is expected to be important in determining a shift from aerobic to anaerobic respiration or fermentative metabolism in the microbial community.

The solutions examined here are presented in terms of Thiele moduli, dimensionless numbers that compare the rates of reaction and diffusion of oxygen. There are two Thiele moduli: one for the biofilm region (ϕ_B) and another one for the neutrophil region (ϕ_N). When a Thiele modulus is small, say $\phi < 1$, diffusive transport is fast compared to reaction, which means diffusion dominant. Conversely, when a Thiele modulus is large, say $\phi > 1$, diffusive transport is slow compared to reaction and steep concentration gradients can develop.

Simulation parameter values were drawn from references as summarized in Table 2.2 and five specific cases representing a spectrum of possibilities were analyzed.

Table 2.2: Parameter Values

Parameter	Notation	Value	Reference
Dimension of neutrophil layer	h_N or r_N	$20 - 2000\mu m$	[25, 32, 66]
Dimension of biofilm layer	h_B or r_B	$5 - 1200\mu m$	[6]
Oxygen concentration at tissue interface	C_H	$30 - 160\mu m$	[107]
Oxygen concentration at air interface	C_A	$190 - 250\mu m$	[26]
First-order oxygen consumption rate for neutrophil	k_N	$0.001 - 0.28s^{-1}$	[64]
First-order oxygen consumption rate for biofilm	k_B	$0.017 - 1.7s^{-1}$	[64]
Diffusion coefficient of oxygen in neutrophil layer	D_N	$10^{-5}cm^2s^{-1}$	[108]
Diffusion coefficient of oxygen in biofilm layer	D_B	$10^{-5}cm^2s^{-1}$	[108]

Table 2.3: Parameter values for simulations

Case	(s^{-1}) k_B	$\mu m h_B$	$(\mu m^2 s^{-1})$ D_B, D_N	(s^{-1}) k_N	$\mu m h_N$	ϕ_B	ϕ_N	Scenario
A	0.01	10	1000	0.001	10	0.032	0.01	Both ϕ_N , ϕ_B small
B	0.01	10	1000	0.1	1000	0.032	10	ϕ_N dominates
C	0.1	100	1000	0.01	100	1	0.32	Both ϕ_B , ϕ_N intermediate
D	1	1000	1000	0.001	10	32	0.01	ϕ_B dominates
E	1	1000	1000	0.1	1000	32	10	Both ϕ_N , ϕ_B large

Parallel Slabs Bounded by Oxygen Sources

We study first the flat slab geometry that is bounded by air along one edge and host tissue on the other. These results correspond to the geometry diagrammed in Figure 2.1. The illustrative cases presented in Figure 2.4 suggest a range of possible outcomes. Concentration minima are predicted in three of the five cases. Hypoxia at the biofilm-neutrophil interface is predicted in only one case (Figure 2.4E), and hypoxia internally within the biofilm layer is predicted in two instances (Figure 2.4D and E). In this simulation, we define hypoxia as less than 10 mm Hg of oxygen. When the Thiele moduli are relatively small, approximately linear concentration profiles are predicted, see A and C in Figure 2.4. When one or both Thiele moduli is large, concentration minima and large hypoxic zones are predicted, see B, D and E in Figure 2.4. The dimension of the region of hypoxia in these latter three cases ranges from approximately 0.5 to 1.7 mm.

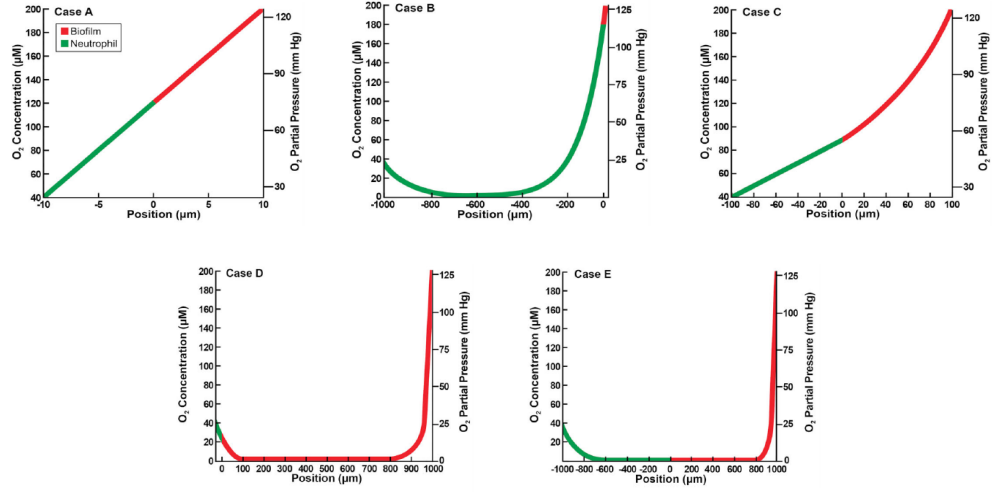


Figure 2.4: Oxygen concentration profiles in slab geometry bounded by air and host tissue for five illustrative cases as detailed in Table 2.3. Figures A-E correspond to the lettered cases in the table. Position is the value of depth of the variable z , with $z > 0$ corresponding to the biofilm layer and $z < 0$ to the neutrophil layer.

To explore these outcomes further, the occurrence of hypoxia was plotted as a function of the two Thiele moduli (Figure 2.5). Hypoxia develops within the biofilm (shown in Figure 2.5A) when the biofilm associated Thiele modulus, ϕ_B , is greater than about 3. Hypoxia develops at the biofilm-neutrophil interface if $\phi_B > 3$ and $\phi_N > 0.2$ (shown in Figure 2.5B).

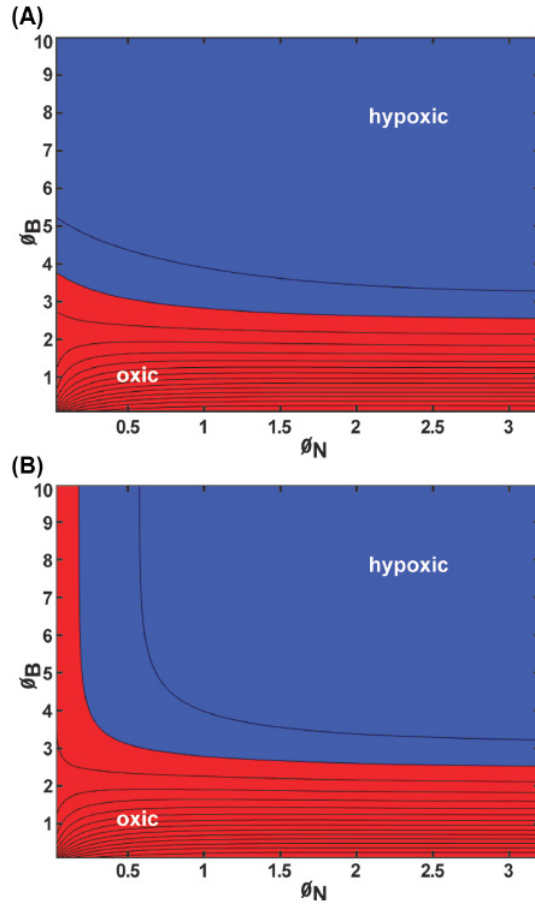


Figure 2.5: Oxygen concentration within the biofilm layer for slab geometry bounded by an air and host tissue with first-order kinetics presented as a contour plot: (A) minimum concentration within the biofilm; (B) concentration at the biofilm-neutrophil interface. Blue denotes values corresponding to hypoxia (less than 10 mm Hg oxygen); red denotes values that are oxic (greater than or equal to 10 mm Hg oxygen). Parameter values: $C_A = 200\mu m = 127.6$ mm Hg, $C_H = 40\mu m = 25.5$ mm Hg, $k_N = 0.01s^{-1}$, $k_B = 0.1s^{-1}$, $D_N = 1000\mu m^2s^{-1}$, $D_B = 1000\mu m^2s^{-1}$, h_N ranging from 10 to 1000 μm , h_B ranging from 10 to 1000 μm .

Parallel Slabs with One Side Bounded by Implant

Next, we consider the flat slab geometry that is bounded by an implant surface along one edge and host tissue on the other. These results correspond to the geometry diagrammed in Figure 2.2. The concentration of oxygen decreases monotonically from the host interface to a minimum at the implant surface in all of the illustrative cases presented in Figure 2.6. Hypoxia at the biofilm-neutrophil interface is predicted in two cases (shown in Figure 2.6 B and E), and hypoxia internally within the biofilm layer is predicted in four instances (shown in Figure 2.6 A, B, D, and E).

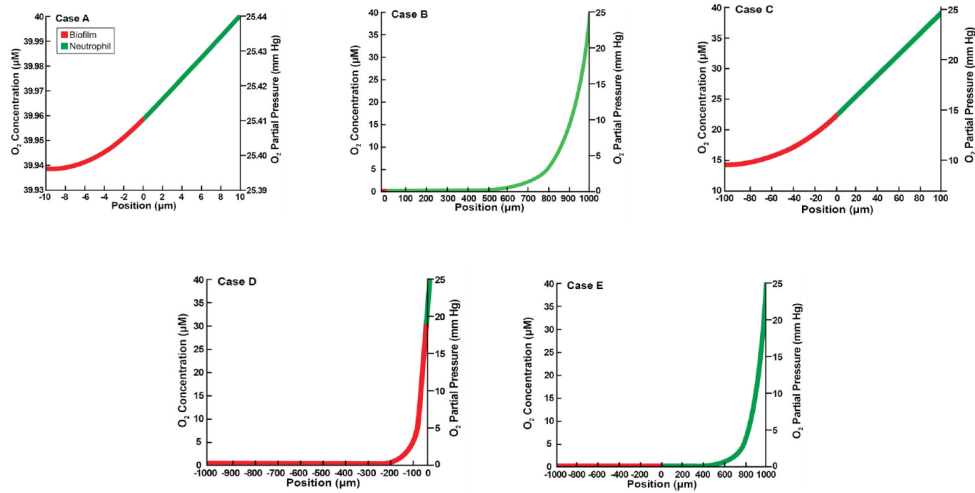


Figure 2.6: Oxygen concentration profiles in slab geometry bounded by an implant and host tissue for five illustrative cases as detailed in Table 2.3. Figures A-E correspond to the lettered cases in the table. Position is the value of depth of the variable z , with $z < 0$ corresponding to the biofilm layer and $z > 0$ to the neutrophil layer.

To explore these outcomes further, the occurrence of hypoxia was plotted as a function of the two Thiele moduli (Figure 2.7). Hypoxia develops within the biofilm when either ϕ_B or ϕ_N exceeds about 1 (shown in Figure 2.7A). Hypoxia develops at the biofilm-neutrophil interface if ϕ_N is larger than about

0.4 (shown in Figure 2.7B).

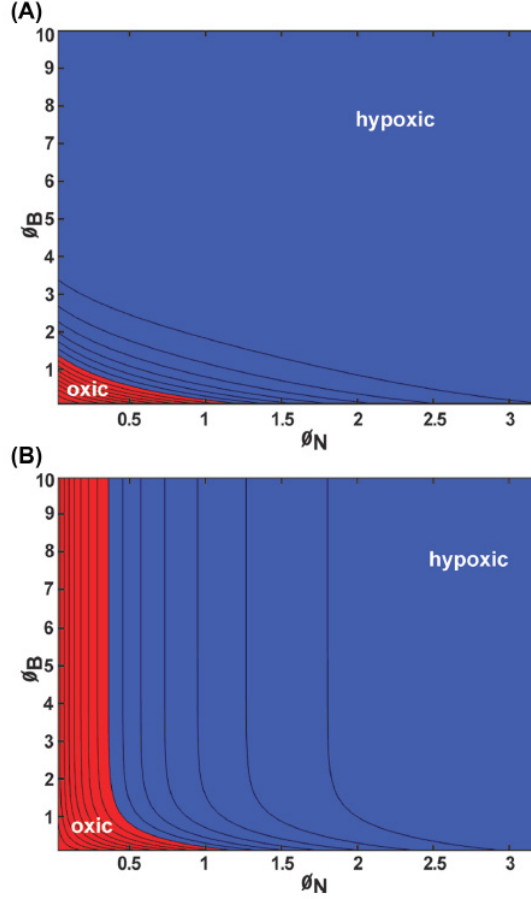


Figure 2.7: Oxygen concentration within the biofilm layer for slab geometry bounded by an implanted and host tissue with first-order kinetics presented as a contour plot: (A) minimum concentration within the biofilm; (B) concentration at the biofilm-neutrophil interface. Blue denotes values corresponding to hypoxia (less than 10 mm Hg oxygen); red denotes values that are oxic (greater than or equal to 10 mm Hg oxygen). Parameter values: $C_A = 200\mu m = 127.6$ mm Hg, $C_H = 40\mu m = 25.5$ mm Hg, $k_N = 0.01s^{-1}$, $k_B = 0.1s^{-1}$, $D_N = 1000\mu m^2s^{-1}$, $D_B = 1000\mu m^2s^{-1}$, h_N ranging from 10 to 1000 μm , h_B ranging from 10 to 1000 μm .

Spherical Geometry with a Biofilm Core

Representative oxygen concentration profiles for the concentric spherical structure (a biofilm core surrounded by a neutrophil shell) are plotted in Figure 2.8. These results correspond to the geometry diagrammed in 2.3. The profiles decrease monotonically to a minimum at the center of the structure; the lowest oxygen concentration experienced by the microorganisms occurs at this point. Hypoxia at the biofilm-neutrophil interface is predicted in two cases (shown in Figure 2.8 B and E) and hypoxia within the biofilm in three cases (shown in Figure 2.8 B, D and E). Hypoxia at the center is manifested with $\phi_B > 4$ or at smaller values of ϕ_B if ϕ_N is sufficiently large (shown in Figure 2.9 A). In the spherical geometry, hypoxia at the biofilm-neutrophil interface requires that ϕ_N is greater than approximately 2 (shown in Figure 2.9 B).

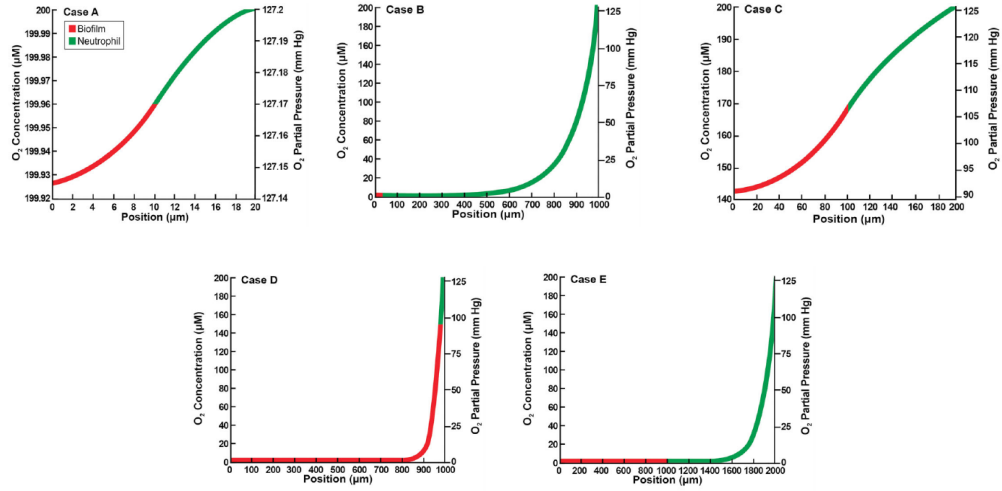


Figure 2.8: Oxygen concentration profiles in spherical geometry for five illustrative cases as detailed in table 2.3. Figures A-E correspond to the lettered cases in the table. Position is the value of depth of the variable r .

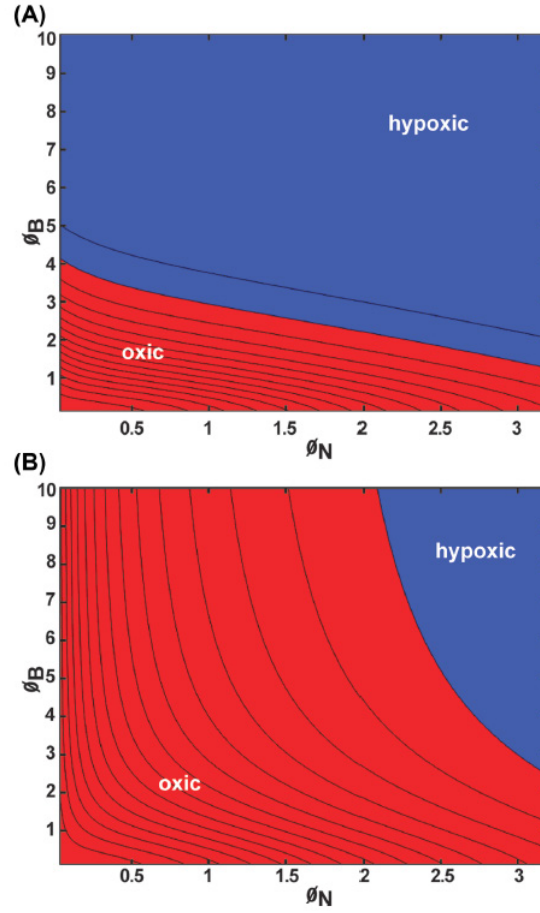


Figure 2.9: Oxygen concentration within the biofilm layer for spherical geometry with first-order kinetics presented as a contour plot: (A) minimum concentration within the biofilm; (B) concentration at the biofilm-neutrophil interface. In this setting, the minima are always at the center of the composite structure. Blue denotes values corresponding to hypoxia (less than 10 mm Hg oxygen); red denotes values that are oxic (greater than or equal to 10 mm Hg oxygen). Parameter values: $C_A = 200\mu m = 127.6$ mm Hg, $C_H = 40\mu m = 25.5$ mm Hg, $k_N = 0.01s^{-1}$, $k_B = 0.1s^{-1}$, $D_N = 1000\mu m^2s^{-1}$, $D_B = 1000\mu m^2s^{-1}$, h_N ranging from 10 to 1000 μm , h_B ranging from 10 to 1000 μm .

2.1.5 Conclusion and Discussion

Locally reduced oxygen tension is a common feature of the *in vivo* biofilm. We analyzed the reaction-diffusion interactions that underpin the establishment of oxygen concentration gradients *in vivo*. The results support the conjecture that oxygen consumption by both microorganisms in the biofilm and host neutrophil can contribute to the development of hypoxic conditions in the vicinity of a biofilm infection. In all three geometries considered (biofilm near an air interface as in a dermal wound or mucus layer, biofilm on an implanted medical device, biofilm aggregates dispersed in mucus or tissue), hypoxia was predicted with a subset of a plausible parameter values representing ranges of the oxygen consumption kinetics of microorganisms and neutrophil, oxygen diffusion coefficients, and biofilm and neutrophil region dimensions. Specifically, realistic conditions were found for all three scenarios analyzed that could lead to hypoxia at the biofilm-neutrophil interface or hypoxia in the interior of the biofilm layer.

These calculations suggest that hypoxia may manifest more readily on an implant (Figure 2.7) than in a wound or lung mucosal biofilm (Figure 2.5). The reasons for this are simply that the biofilm on the implant is supplied with oxygen at a lower concentration (in our analysis, $40\mu m$ in the tissue rather than $200\mu m$ at the air interface) and the implant is supplied with oxygen from a single boundary rather than from both sides.

The oxygen concentration gradients we have calculate resemble those measured experimentally *in vivo* and *ex vivo* [124, 56, 65, 23, 53]. Depletion of oxygen to hypoxic levels (here taken as below 10 mm Hg or $16\mu m$ oxygen) was reported in five of the six measurements summearized in Table 2.3. The distance over which oxygen concentration decreased from a maximum to minimum values ranged from 480 to 8850 microns. These distances are similar to those used in our calculation Table 2.2. Oxygen gradients measured in mice with biofilm-infected wound scabs immediately after euthanization found minima in oxygen concentration profiles that resemble those predicted here (Figure

2.4 D and E).

The finding that oxygen concentration at the interface of the biofilm and neutrophil layers can be diminished to hypoxic levels is biologically relevant because oxygen depletion will reduce neutrophil killing ability [75, 62, 37, 56]. Neutrophil-mediated killing is dependent in part on the generation of reactive oxygen species from molecular oxygen. If the environment around a biofilm contains little oxygen, neutrophils will be impaired in their ability to generate reactive oxygen species such as hydrogen peroxide and hypochlorous acid. This impairment will compromise neutrophil ability to control and eliminate microorganisms.

The finding that hypoxia can readily establish within the biofilm layer is biologically relevant because this change in environment will likely alter microbial growth and metabolism. For a facultative anaerobic bacterium such as *P. aeruginosa*, oxygen depletion may limit microbial growth. Bacteria that enter an altered metabolic state in which the organism is less susceptible to antibiotics [9, 33, 59, 100, 42]. For a voluntary microorganisms such as *Staphylococcus aureus*, oxygen limitation will likely cause a shift to a fermentative metabolism [127]. With this shift, the bacterium acquires an advantage as it can sustain metabolic activity and continue to replicate whereas the host faces conditions that are not permissive of healing.

2.2 Biofilm Modeling in Marble Environment

2.2.1 Biofilm on Stone

Biofilm may exist on any solid surface in which sufficient moisture is available in nature. Rock surfaces freshly exposed to the atmosphere can be colonized by microbial communities forming subaerial biofilms (i.e. biofilm growing in the open air, rather than in a water environment) [38]. Subaerial biofilms are made up of many different types of microbial cells, and the microbial connections between cells helps to avoid the loss of energy and nutrients. The biofilm employs coordinated survival strategies to increase resistance to environmental factors (e.g. being washed off from the rain) [118]. Recently, researchers noticed that such kind of microbial communities threatened the artistic and historical value of certain monuments in Washington, D.C (shown in figure 2.10). The memorial had a white dome in 2001 (left photo in figure 2.10), while some black blocks were observed on the dome more recently (right photo in figure 2.10). To understand how biofilm grows on the monuments, we first build a mathematical model to describe the biofilm living environment and then add biomass into the model to connect biofilm growth and its living environment.



Figure 2.10: Photos of Jefferson Memorial in 2001 (left) (Credit: David Pleacher) and 2017 (right)(Credit: George Rose/Getty Images)

In the first part of this project, we study the environmental conditions in which biofilm grow on the surface of marble. Water, light, and carbon dioxide are essential components for photosynthesis, and we assume light and carbon dioxide are abundant in the outdoor environment. Water and salt (from biodeterioration of marble) both exist on the marble and form a solution in the biofilm living environment on the monument, and they together affect the concentration of the solution in which biofilm resides. Water on the marble determines how fast photosynthesis takes place. The masses of the water and salt (from biodeterioration of marble) in the solution are variables, changing with the weather data, such as temperature, relative humidity, vapor pressure, etc. This model connects some of these weather indicators with related masses by a coupled ODE system of two equations. The first equation describes the water flux on the air-liquid interface, and the second equation represents the salt flux on the liquid-stone interface. Solving these two equations with plausible parameters, we will obtain the mass of water and mass of salt on the marble surface (biofilm living environment).

For the second part of this project, we further develop the first model by adding biomass. The biofilm growth rate and the quantity of biomass are the objects we are interested in. The first equation is changed by subtracting the water uptake by biomass for photosynthesis from the total amount of water available in the system, and a new equation is added to describe the biofilm growth. Solving this system with fixed parameters, we will obtain the mass of water, salt, and biofilm on the marble.

2.2.2 Deliquescence Process and Deliquescence Model

Deliquescence Process

Water is one of the essential components for photosynthesis, biofilm survival, and biofilm growth. The amount of liquid or vapor water in the environment is the first aspect we need to consider. The available water in the system determines whether photosynthesis takes place, and also results in the increase

of biomass. We first assume that due to weathering or biodeterioration, there is a thin layer of salt crystals on the surface of the marble. Such salt that originates from the earth's surface plays an essential role in many atmospheric processes. Both natural and artificial chemicals contribute to the formation of aerosols, which are composed mostly of sulfate, nitrates, and chlorides in their pure or mixed form. These inorganic salt aerosols are hygroscopic (absorb moisture from the air) by nature and deliquescent in the humid air [113]. Deliquescence happens when the atmosphere relative humidity (RH) increases to a certain threshold, and beyond the threshold, salt crystals start to adsorb water molecules on their surfaces and dissolved into water to form a thin layer of salt solution [11].

The humidity threshold of the salt is defined as the critical relative humidity (RH_0) of the salt (at a specific temperature) at which such material begins to absorb moisture from the atmosphere and below which it will not absorb atmospheric moisture. The relative humidity related to the deliquescence process can also be named deliquescence RH or deliquescence point. RH_0 is a material property which depends on the chemical composition and physical properties of the salt particle, e.g., the molecular mass of the salt, density of the solution, the solubility of the solvent, and temperature. However, the conventional measuring methods of RH_0 are complicated and tedious, and the most convenient way so far is to determine the RH_0 by measuring air humidity in equilibrium directly. In this project, we show a mathematical approach to obtain such critical relative humidity RH_0 (later in section 2.2.3), and validates the values with the existed data.

From the view of thermodynamics, the phenomenon of deliquescence occurs when the vapor pressure of the solution that is formed is less than the partial pressure of the water vapor in the air because of the affinity of the salt for water. Vapor pressure is defined as the pressure exerted by a vapor in thermodynamic equilibrium with its condensed phases at a given temperature in a closed system. The vapor pressure is an indication of a liquid's evaporation rate, and it relates to the tendency of particles to escape from the liquid (or a

solid). The vapor pressure of a gas is a measure of thermodynamic activity of the gas's molecules. In thermodynamics, the chemical potential is

$$\mu = \mu_0 + RT \ln(p_0),$$

where μ_0 is the standard chemical potential, R is the gas constant, T is the temperature, and p_0 is the vapor pressure of pure water. Let μ_{sol} be the chemical potential of the water in the saturated solution. The difference between the chemical potential of the water in the solution and pure water can be expressed as

$$\mu_{sol} - \mu = RT \ln \left(\frac{p_{sol}}{p_0} \right), \quad (2.17)$$

where p_{sol} is the vapor pressure of the solution which is an indication of the evaporation rate. Since $p_{sol} < p_0$ (by Raoult's law explained in chapter 2.2.3), the chemical potential or thermodynamic activity of the solution is lower than that of pure water. When the vapor pressure exceeds p_{sol} , or equivalently when the relative humidity from the surrounding exceeds RH_0 , condensation of water occurs in the system, which raises the vapor pressure of the solution to that of the surrounding vapor pressure. Dissolution of the solid brings the vapor pressure back to critical relative humidity (RH_0) and following this pattern, dissolution and condensation take effect until all the available salt dissolves in the solution. Equilibration with the atmosphere is reached when complete dissolution has occurred.

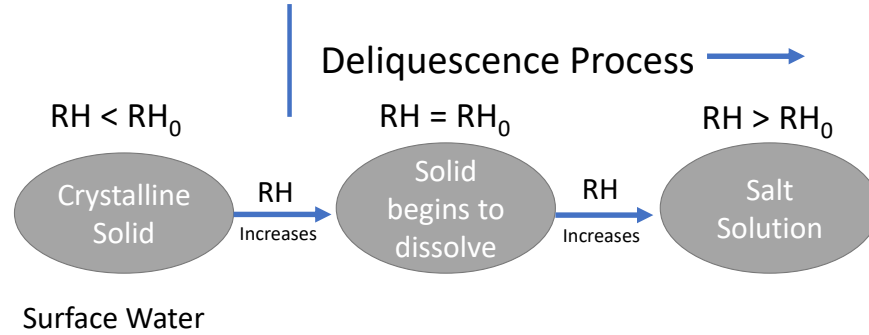


Figure 2.11: Diagram of the interaction of salt solid with water vapor in the atmosphere with different relative humidity values, where RH_0 = deliquescence relative humidity and RH = atmosphere relative humidity. When $RH < RH_0$, salt adsorb minimal amounts of moisture at surfaces. Upon increasing the RH to RH_0 , more vapor is adsorbed at the surface, and the salt will dissolve until saturation is reached.

Deliquescence Model

As a result of the deliquescence procedure, water molecules adsorb on the surface of the salt molecules and forms a saturated solution (shown in Figure 2.11). The salt/marble, liquid, and air form a three-layered dynamical system coupled with molecular phase changes (shown in Figure 2.12). Condensation and evaporation happen at the air-liquid interface, while dissolution and precipitation occur at the salt/stone-liquid interface. The mathematical models we derive later are based on this geometry and considered the dynamics of phase changes at the two interfaces.

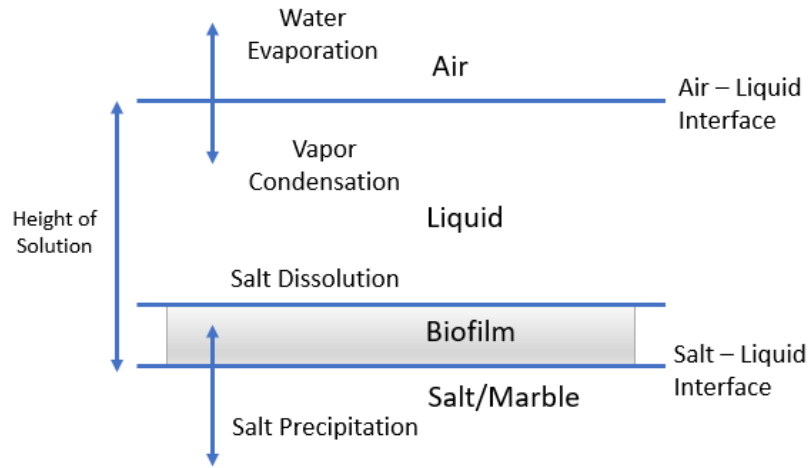


Figure 2.12: Three-layered dynamics of air, liquid, and salt/stone. Water condensation and evaporation happen at the air-liquid interface, while salt dissolution and precipitation occur at the salt/stone-liquid interface. Biofilm exists on the salt layer and immersed in the solution. The cartoon is demonstrating the phase changes and is not drawn to scale.

2.2.3 Deliquescence Model without Biofilm

Model Setup

We first consider a deliquescence model without biofilm, and we will add the biomass into the system in the next section. Let $m_w(t)$ be the mass in kg of the pure water in the solution on a unit area on marble, and $m_s(t)$ be the mass in kg of the salt in the solution on a unit area. We derived a system of ODEs for the flux of water and salt on two interfaces.

We first consider phase changes on the air-liquid interface modeled with the Hertz-Knudsen equation (HK) [63].

Hertz-Knudsen Equation

The HK equation (as derived by Knudsen and Hertz in 1956) follows from kinetics theory for gases via the formula giving the number of molecules hitting

the liquid-air surface at equilibrium, per unit area and unit time. The HK equation is

$$m'_w(t) = \sqrt{\frac{M}{2\pi k_B}} \left(\sigma_c \frac{P_v}{\sqrt{T_V}} - \sigma_e \frac{P_s(T_L)}{\sqrt{T_L}} \right). \quad (2.18)$$

In equation (2.18), on the left hand side, $m'_w(t)$ is the mass flux of water, while on the other side of the equation is the evaporation and condensation rates. When $m'_w(t) > 0$, condensation dominates the equation, and the mass of water increases. Conversely, when $m'_w(t) < 0$, evaporation dominates, and the mass of water decreases. In equation (2.18), M is the mass of a water molecule, k_B is the Boltzmann constant, T_v is the vapor temperature, T_L is the solution temperature, P_v is the vapor pressure, and P_s is the vapor pressure of solution. In this system, we have a thin layer of solution between stone and air, so we assume that the ambient temperature in the air and the temperature in the solution are the same, say $T_V = T_L = T$.

σ_c is the condensation coefficient for condensation and σ_e is the evaporation coefficient for evaporation. The evaporation and condensation coefficients indicate the fraction of molecules that strike the interface and change phases from their initial liquid or vapor states, respectively. If each particle that collided with the interface were to change phase, then the coefficients would have a value of unity. The factors represent the ratio of the actual unidirectional flux compared to the maximum flux predicted from classical kinetic theory (CKT) [76]. CKT describes gas as a large number of submicroscopic particles (atoms or molecules), all of which are in constant, rapid, random motion. The randomness arises from the particles' many collisions with each other and with interfaces between two phases. Following CKT, the values of σ_e and σ_c must be between 0 and 1 and many investigators have assumed [79]:

$$\sigma_e = \sigma_c = \sigma = 0.243. \quad (2.19)$$

Relative Humidity and Pressure

There are two pressure terms in equation 2.18. The vapor pressure P_v is defined as the pressure exerted by vapor in thermodynamic equilibrium with its condensed phase (liquid in this case) at a given temperature in a closed system, and this can be directly measured or approximated by relative humidity and temperature. By definition, the actual vapor pressure can be calculated with saturated vapor pressure multiplied by the relative humidity which is one of the most important parameters associated with the deliquescence model.

The definition of relative humidity is

$$RH = \frac{P_v(T)}{P_{v_{sat}}(T)}, \quad (2.20)$$

where $P_v(T)$ is the vapor pressure at temperature T and $P_{v_{sat}}(T)$ is the saturation vapor pressure at temperature T . Monteith and Unsworth [78] provided an approximation of the function for saturation vapor pressure ($P_{v_{sat}}(T)$) of water from experiments in 2008 by,

$$P_{v_{sat}}(T) = 0.61078e^{\frac{17.27T}{T+237.3}}. \quad (2.21)$$

Thus from equation (2.20) and (2.21), we have

$$P_v(T) = RH \cdot 0.61078e^{\frac{17.27T}{T+237.3}}. \quad (2.22)$$

Equation (2.22) calculates the vapor pressure of water, where temperature T is in degrees Kelvin and saturation vapor pressure $P_{v_{sat}}$ is in KiloPascals.

The vapor pressure of solutions $P_s(T)$ of a non-volatile solute is equal to the vapor pressure of the pure water at that temperature multiplied by its mole fraction r_w which describes the percentage of water molecules over all molecules in the solution

$$r_w = \frac{\frac{m_w}{M_w}}{\frac{m_w}{M_w} + \frac{m_s}{M_s}}, \quad (2.23)$$

where M_w , M_s are the molar masses for a water molecule and a salt molecule, and m_w and m_s are the masses of water and salt in the solution. The relation-

ship between vapor pressure and solution composition is therefore,

$$\begin{aligned} P_s(T) &= r_w P_{v_{sat}}(T), \\ &= \frac{\frac{m_w}{M_w}}{\frac{m_w}{M_w} + \frac{m_s}{M_s}} P_{v_{sat}}(T), \end{aligned}$$

If the solution contains only a single nonvolatile solute (salt), then $r_w + r_s = 1$ [41], where r_s is the mole fraction of the salt molecule (similar to equation (2.23)). Now we have,

$$P_v(T) = RH \cdot P_{v_{sat}}(T) = RH \cdot 0.61078e^{\frac{17.27T}{T+237.3}}, \quad (2.24)$$

$$\begin{aligned} P_s(T) &= r_w P_{v_{sat}}(T) \\ &= r_w \cdot 0.61078e^{\frac{17.27T}{T+237.3}} \\ &= (1 - r_s) \cdot 0.61078e^{\frac{17.27T}{T+237.3}}. \end{aligned} \quad (2.25)$$

Noyes-Whitney Equation

$$m'_s(t) = D \left(C_s - \frac{m_s}{m_w} \rho_s(m_w, m_s) \right). \quad (2.26)$$

Equation (2.26) is named the Noyes-Whitney equation [84] after their experiment in 1897, which relates the rate of dissolution of solids to the properties of the solid and the dissolution medium. Equation (2.26) relates the rate of dissolution of solids to the properties of the solid and dissolution medium. In this equation, C_s is the solubility of the salt in water and D is the traveling velocity. The traveling velocity describes how fast salt molecules dissolve in the water, which depends on chemical and physical properties. Solubility is the capacity of a solute to dissolve in a pure solvent, i.e., the maximum amount of solute that the pure solvent can hold in solution at a specified temperature in degree Kelvin. Beyond solubility, salt molecules can exist tenuously in a supersaturated concentration, but will eventually revert to the solvent's true capacity. $\rho_s(m_w, m_s)$ is the density function of the salt solution which depends on the water mass and salt mass. Therefore, when $C_s > \frac{m_s}{m_w} \rho_s(m_w, m_s)$, the

solution is undersaturated, salt dissolves into the solution, and the mass of salt in the solution increases. Conversely, when $C_s < \frac{m_s}{m_w} \rho_s(m_w, m_s)$, the solution is supersaturated, salt precipitates out of solution, and the mass of salt in the solution decreases. In the Noyes-Whitney equation, they assumed that there is infinitely available salt in the system. However, in our model, we modified Equation (2.26) by multiplying a constraint for the availability of salt (maximum amount of salt exists in the system) to limit the volume of dissolved salt (in the real case, there is a limited amount of salt on the marble). The modified Noyes-Whitney equation is

$$m'_s(t) = D \left(C_s - \frac{m_s}{m_w} \rho_s(m_w, m_s) \right) \left(1 - \frac{m_s(t)}{m_s^{max}} \right). \quad (2.27)$$

We use equation (2.27) to describe the salt flux $m'_s(t)$ on the stone-liquid interface in the deliquescence model. m_s^{max} is the total amount of salt available in the system. Since the density of the solution does not affect the concentration too much and is close to water density, to simplify the model, we approximate the salt solution density with the density of the pure water ρ_0 at room temperature for the analysis and simulation.

ODE system

After the above discussion and simplification, equations (2.18) and (2.27) become

$$m'_w(t) = \sigma E \sqrt{\frac{M}{2\pi k_B T}} \left(RH - \frac{\frac{m_w}{M_w}}{\frac{m_w}{M_w} + \frac{m_s}{M_s}} \right), \quad (2.28)$$

$$m'_s(t) = D \left(C_s - \frac{m_s \rho_0}{m_w} \right) \left(1 - \frac{m_s}{m_s^{max}} \right), \quad (2.29)$$

where

$$E = 0.61078 e^{\frac{17.27T}{T+237.3}}.$$

By solving the above ODE system with plausible parameters, we have the mass of the pure water on the top of marble and the mass of the dissolved

salt in the solution. These two quantities determine whether photosynthesis takes place (in the deliquescence model with biofilm) or not, which is related to biofilm growth.

To have a better understanding of the solution behavior, we solve the equilibrium points for this system and then check the stability of these points after perturbation. Since stable and unstable equilibria play different roles in the dynamics system, it is useful to classify equilibrium points based on the stability.

Table 2.4: List of Parameters

symbol	name	test value(description)	unit
M	mass of single water molecule	3×10^{-26}	kg
M_w	molar mass of water	18	$k \cdot mol^{-1}$
M_s	molar mass of salt	depends on the salt	$k \cdot mol^{-1}$
σ_e	mass accommodation coefficient for evaporation	0.243 [79]	
σ_c	mass accommodation coefficient for condensation	0.243 [79]	
k_B	Boltzmann constant	1.38×10^{-23}	$kgm^2s^{-2}K^{-1}$
T_v	Air temperature	300 (26)	$K(C)$
T_L	Solution temperature	300 (26)	$K(C)$
RH	relative humidity	variable	
$P_v(T)$	vapor pressure in the air	variable	$kgms^{-2}$
$P_s(T)$	vapor pressure in the solution	variable	$kgms^{-2}$
C_s	solubility of the salt in water	depends on the salt	kgm^{-3}
D	diffusion coefficient	depends on the salt	m^2s^{-1}
ρ_s	density of the solution	1000	kgm^{-3}
m_s^{max}	total amount of salt	10	kg

Equilibrium Solution

To determine the equilibria of the ODE system, let m_w and m_s be time independent (long time behavior), and set $m'_w(t) = 0$ and $m'_s(t) = 0$. After substituting $P_s(T)$, and $P_v(T)$ into the equation, we have

$$0 = m'_w(t) = \sigma E \sqrt{\frac{M}{2\pi k_B T}} \left(RH - \frac{\frac{m_w}{M_w}}{\frac{m_w}{M_w} + \frac{m_s}{M_s}} \right), \quad (2.30)$$

$$0 = m'_s(t) = D \left(C_s - \frac{m_s \rho_0}{m_w} \right) \left(1 - \frac{m_s}{m_s^{max}} \right). \quad (2.31)$$

Critical RH for Deliquescence (RH_0)

There are three equilibrium solutions for the above system corresponding to high RH , low RH and the critical RH cases. The critical RH (RH_0) can be obtained by solving the equilibrium equation (equation (2.30)) at $RH = RH_0$. Let m_w^{eq} , m_s^{eq} be the equilibrium solution, solving equation (2.30) we have,

$$RH_0 = \frac{\frac{m_w^{eq}}{M_w}}{\frac{m_w^{eq}}{M_w} + \frac{m_s^{eq}}{M_s}}, \quad (2.32)$$

$$C_s = \frac{m_s^{eq}}{m_w^{eq}} \rho_0. \quad (2.33)$$

From equation (2.33) we have,

$$m_s^{eq} = \frac{C_s m_w^{eq}}{\rho_0}, \quad (2.34)$$

which is the relation between the m_s^{eq} and m_w^{eq} .

Substituting the equation (2.34) into equation (2.32) we have,

$$RH_0 = \frac{M_s \rho_0}{M_s \rho_0 + C_s M_w}. \quad (2.35)$$

From equation (2.35), we know that the RH_0 depends on physical properties of the salt, such as molar mass (M_s) and the solubility of the salt (C_s). For different kinds of salt in table 2.5, RH_0 varies, and RH_0 values for different salts determine r_w^{eq} (molar ratio of the number of water molecules among the number of all the molecules) in the system. Also, under the same RH condition, the

salt with lower RH_0 adsorb more water molecules on the surfaces. For different RH values, compared with RH_0 , we have three following cases:

- When $RH > RH_0$, $m'_w(t) > 0$. In this case, we have an increasing amount of water because condensation dominates equation (2.28). The increases in m_w lower the solution concentration, correspondingly, salt starts to dissolve into the solution, and in equation (2.29) $m'_s(t) > 0$. Therefore both of the masses increase until all the available salt dissolves into the solution as shown in figure (2.18) from the simulation. Once all the available salt dissolved, $m_s(t) = m_s^{max}$ and $m_w(t)$ stops growing.
- When $RH < RH_0$, $m'_w(t) < 0$. In this case, evaporation of water dominates equation (2.28), and water mass decreases. As a consequence, the solution becomes supersaturated and salt precipitates. Therefore both of the masses decreases to zero as shown in figure (2.19) from the simulation.
- When $RH = RH_0$, $m'_w(t) = 0$. There are no mass fluxes on the air-liquid and stone-liquid interfaces.

Table 2.5: Possible Dissoluble Chemical Salts on Marble

Chemicals	Name	Molecular weight	Solubility (kg/m^3)	Critical RH (RH_0)
$NaCl$	Sodium chloride	59	359	0.4772
$Ca(NO_2)_2$	Calcium nitrite	132	845	0.4646
$Ca(NO_3)_2$	Calcium nitrate	236	1212	0.5040
$Ca(Cl)_2$	Calcium chloride	111	745	0.4529
$Ca(HCO_3)_2$	Calcium bicarbonate	162	166	0.8442
$CaSO_4$	Calcium sulfate (gypsum)	172	2.55	0.9973

Comparing the result of the RH_0 for $Ca(Cl)_2$ with the value found by Gough et al in 2016 [39], the value we obtained is in the range of their exper-

imental result ($53.3\% \pm 12.5\%$). Also, comparing the RH_0 we have in Table 2.5 for calcium nitrate with the data they got from experiment, there is a 4% difference.

Equilibrium Solutions

There are three equilibria in this system. We will analyze their stability in the next section.

- Case (1). When $RH = RH_0$, and $C_s = \frac{m_s^{eq} \rho_0}{m_w^{eq}}$, the equilibrium solution is

$$m_s^{eq} = \frac{C_s m_w^{eq}}{\rho_0}.$$

In this case, the percentage of vapor in the air equals to the percentage of water molecules in the solution. At this equilibrium point, there are infinitely many solutions, because the m_s^{eq} and m_w^{eq} are proportional to each other (shown in figure 2.13). As long as we know one of the two quantities, using equation (2.34), we can find the other one. Physically, we obtained infinitely many solutions because the percentage of pure water in the solution, the percentage of pure water in the air (RH), and RH_0 equals to each other.

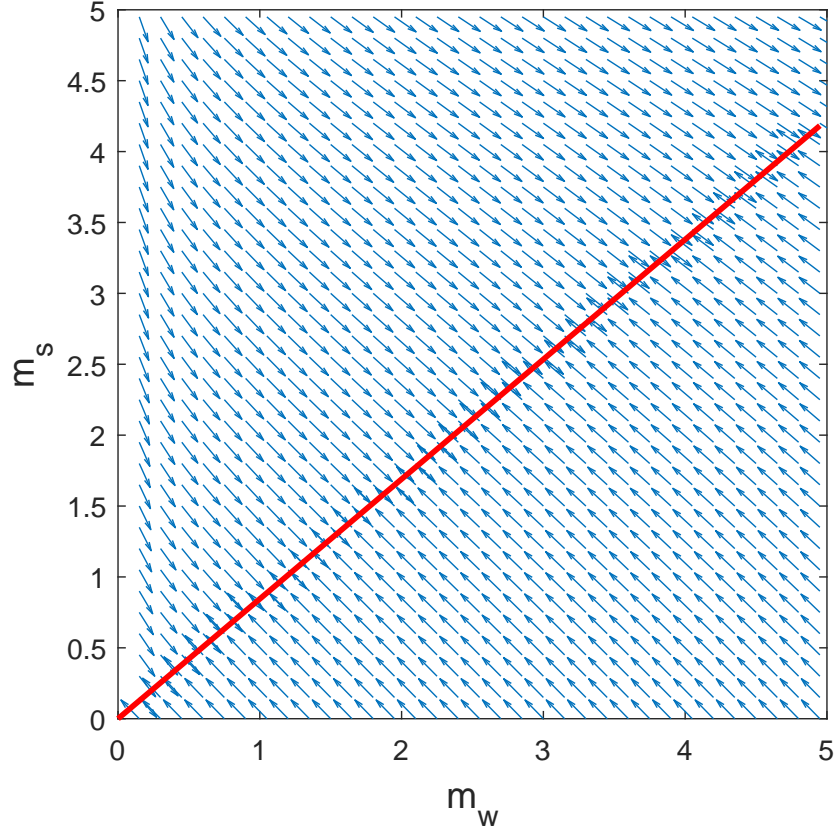


Figure 2.13: Phase portrait of the equation at $RH = RH_0$, and the nullclines of the two odes coincide. There are infinitely many equilibrium points, and all the equilibrium points satisfy the linear relation $m_s^{eq} = \frac{C_s m_w^{eq}}{\rho_0}$ (marked on the red line).

- Case (2). When $RH > RH_0$, and $m_w^{eq} = m_s^{max}$, the equilibrium solution is

$$m_s^{eq} = m_s^{max},$$

$$m_w^{eq} = \frac{RH}{1 - RH} \frac{M_w}{M_s} m_s^{max}.$$

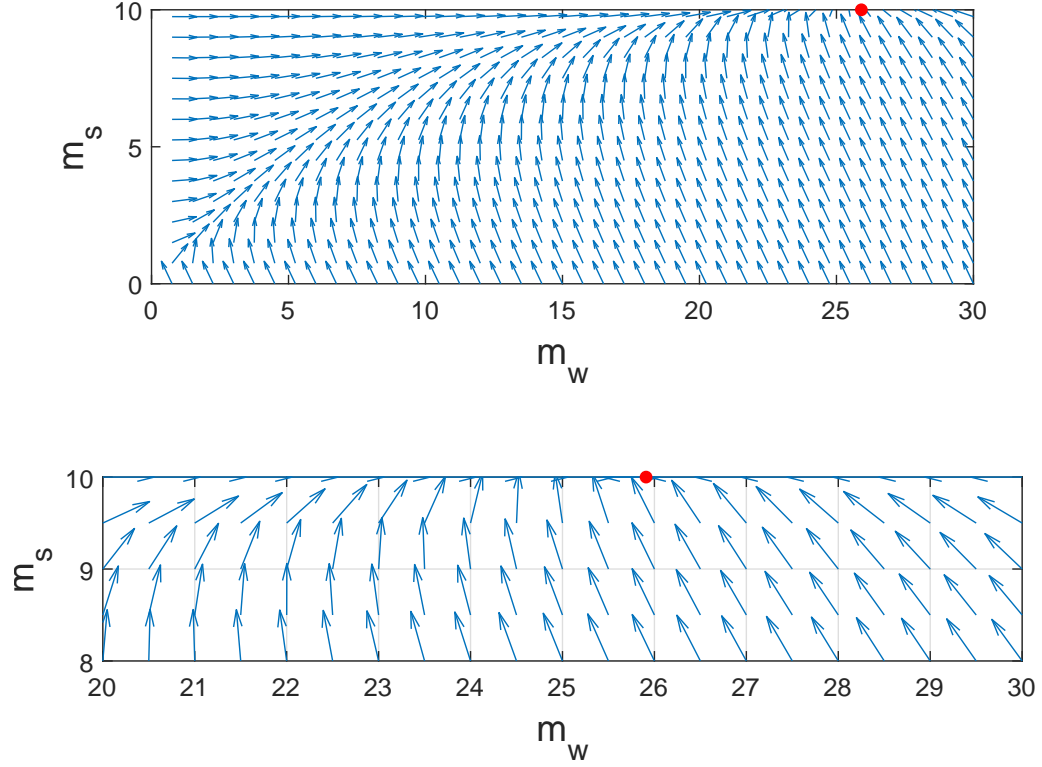


Figure 2.14: Phase portrait of the equilibrium case when $RH = 0.95 > RH_0$, the red dot is the equilibrium solution. In this case, at the equilibrium, all the available salt dissolved in the solution and the m_w^{eq} depends on the RH (0.95 in the simulation). The left figure shows the streamline on the domain $([0, 30] \times [0, 10])$ ($m_s^{max} = 10$), while the right one shows the vector field near the equilibrium point. All the streamlines go towards the red dot.

- Case (3). When $RH < RH_0$, the critical point of the system is

$$m_w^{eq} = 0,$$

$$m_s^{eq} = 0,$$

which is also a singular point of the dynamic system because the system

is not well-defined at $(0, 0)$.

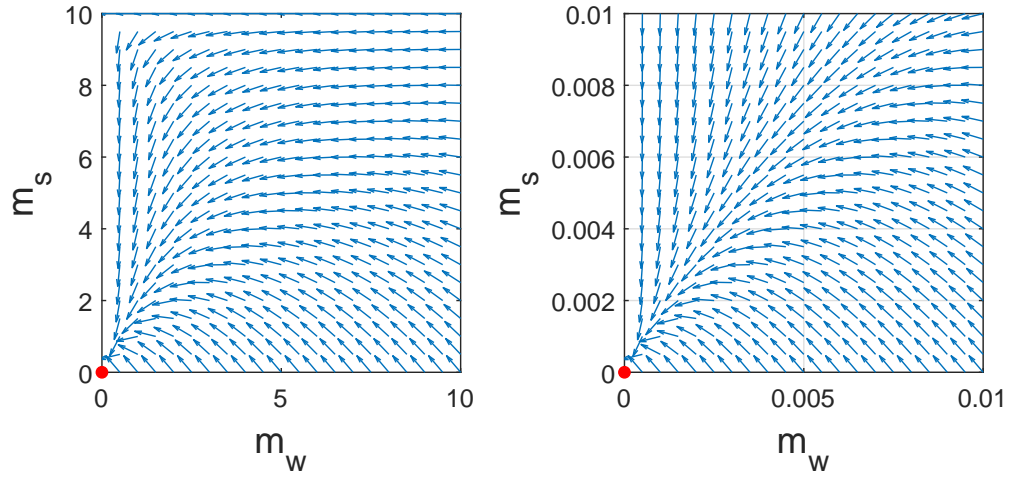


Figure 2.15: Phase portrait of the equilibrium case when $RH = 0 < RH_0$, $m_w^{eq} = 0$ and $m_s^{eq} = 0$ is the singular point of the system. In this case, there is no water in the system, and all the salt is in the solid phase. The left figure shows the streamline on the domain $([0, 10] \times [0, 10])$ ($m_s^{max} = 10$), while the right one shows the vector field near the singular point. All the vectors approach $(0,0)$

Stability Analysis

Stability theory addresses the stability of solutions of differential equations and of trajectories of dynamical systems under small perturbations of initial conditions. In dynamical systems, an orbit is called Lyapunov stable if the forward orbit of any point is in a small enough neighborhood or it stays in a small neighborhood. Conversely, if the system moves away from the equilibrium after small perturbations, then the equilibrium is unstable.

Case 1: Critical RH

For equilibrium case (1), we have an equilibrium solution

$$m_s^{eq} = \frac{C_s}{\rho_0} m_w^{eq}. \quad (2.36)$$

To check the stability of the solution in this case, perturb m_s and m_w around the equilibrium points, and set

$$m_s = m_s^{eq} + \tilde{m}_s, \quad (2.37)$$

$$m_w = m_w^{eq} + \tilde{m}_w. \quad (2.38)$$

We substitute equation (2.37) and (2.38) into equation (2.28), and after ignoring the higher order terms, we have

$$\begin{aligned} \frac{d}{dt} \tilde{m}_w &= \sigma E(T) \sqrt{\frac{M}{2\pi k_B T}} \left(RH - 1 + \frac{(m_s^{eq} + \tilde{m}_s) M_w}{(m_s^{eq} + \tilde{m}_s) M_w + (m_w^{eq} + \tilde{m}_w) M_s} \right) \\ &= \sigma E(T) \sqrt{\frac{M}{2\pi k_B T}} \left(RH - 1 + \frac{(m_s^{eq} + \tilde{m}_s) M_w}{m_w^{eq} M_s + m_s^{eq} M_w} \left(1 - \frac{\tilde{m}_w M_s + \tilde{m}_s M_w}{m_w^{eq} M_s + m_s^{eq} M_w} \right) \right) \\ &= \sigma E(T) \sqrt{\frac{M}{2\pi k_B T}} \left(\frac{\tilde{m}_s M_w}{m_w^{eq} M_s + m_s^{eq} M_w} - (1 - RH) \frac{\tilde{m}_w M_s + \tilde{m}_s M_w}{m_w^{eq} M_s + m_s^{eq} M_w} \right) \\ &= \left(\sigma E(T) \sqrt{\frac{M}{2\pi k_B T}} (RH - 1) \frac{M_s}{m_w^{eq} M_s + m_s^{eq} M_w} \right) \tilde{m}_w \\ &\quad + \left(\sigma E(T) \sqrt{\frac{M}{2\pi k_B T}} (RH) \frac{M_w}{m_w^{eq} M_s + m_s^{eq} M_w} \right) \tilde{m}_s. \end{aligned}$$

Similarly, substitute into equation (2.29), we have

$$\begin{aligned} \frac{d}{dt} \tilde{m}_s &= D \left(C_s - \frac{m_s^{eq} + \tilde{m}_s}{m_w^{eq} + \tilde{m}_w} \rho_0 \right) \left(1 - \frac{m_s^{eq} + \tilde{m}_s}{m_s^{max}} \right) \\ &= D \left(C_s - \frac{(m_s^{eq} + \tilde{m}_s) \rho_0}{m_w^{eq} \left(1 + \frac{\tilde{m}_w}{m_w^{eq}} \right)} \right) \left(1 - \frac{m_s^{eq} + \tilde{m}_s}{m_s^{max}} \right) \\ &= D \left(\frac{-\tilde{m}_s \rho_0 + C_s \tilde{m}_w}{m_w^{eq}} \right) \left(1 - \frac{m_s^{eq} + \tilde{m}_s}{m_s^{max}} \right) \\ &= D \left(\frac{(m_s^{eq} - m_s^{max}) \rho_0}{m_w^{eq} m_s^{max}} \tilde{m}_s + \frac{C_s (m_s^{max} - m_s^{eq})}{m_w^{eq} m_s^{max}} \tilde{m}_w \right) \end{aligned}$$

Let

$$A = \frac{\sigma E(T) \sqrt{\frac{M}{2\pi k_B T}}}{m_w^{eq} M_s + m_s^{eq} M_w},$$

and

$$B = \frac{D(m_s^{max} - m_s^{eq})}{m_w^{eq} m_s^{max}}.$$

Note, $A, B > 0$. We have the linearized system

$$\frac{d}{dt} \begin{bmatrix} \tilde{m}_w \\ \tilde{m}_s \end{bmatrix} = \begin{bmatrix} A(RH_0 - 1)M_s & ARH_0 M_w \\ BC_s & -B\rho_0 \end{bmatrix} \begin{bmatrix} \tilde{m}_w \\ \tilde{m}_s \end{bmatrix}.$$

When $RH_0 = \frac{M_s \rho_0}{M_s \rho_0 + C_s M_w}$, the determinant of the matrix is 0, and the two eigenvalues are,

$$\lambda_1 = 0,$$

$$\lambda_2 = A(RH_0 - 1)M_s - B\rho_0 < 0.$$

Since one of the eigenvalues is zero, to determine the stability of the equilibrium we need to investigate the 2nd order of the perturbed equation.

$$\begin{aligned} \frac{d}{dt} \tilde{m}_w &= A((RH_0 - 1)M_s) \tilde{m}_w + (M_w RH_0) \tilde{m}_s \\ &+ \frac{A}{m_w^{eq}} (M_s RH_0 \tilde{m}_w^2 + M_w RH_0 \tilde{m}_w \tilde{m}_s), \end{aligned} \quad (2.39)$$

$$\begin{aligned} \frac{d}{dt} \tilde{m}_s &= B(-\rho_0 \tilde{m}_s + C_s \tilde{m}_w) \\ &+ \frac{B}{m_s^{eq}(m_s^{max} - m_s^{eq})} ((C_s(m_s^{max} - m_s^{eq}) - \rho_0) \tilde{m}_s^2) \\ &- \frac{B}{m_s^{eq}(m_s^{max} - m_s^{eq})} C_s \tilde{m}_w \tilde{m}_s. \end{aligned} \quad (2.40)$$

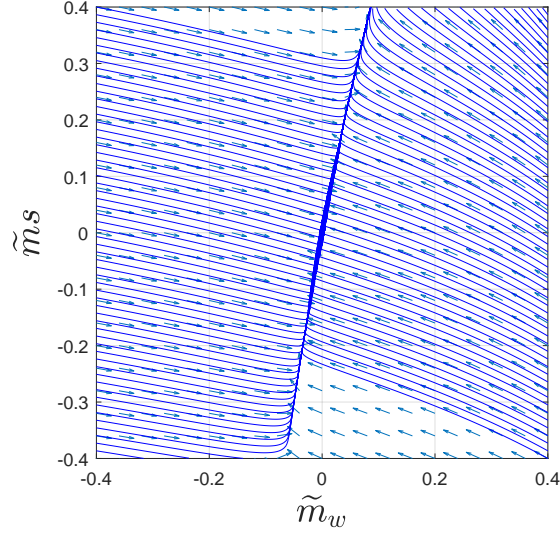


Figure 2.16: The phase portrait with streamlines for equation (2.39) and (2.40). If we put the initial points close enough around the origin, the points will converge to the equilibrium point eventually. Therefore, in the critical RH case, the system is stable. The mass of water and the mass of salt will come back to the red line in figure (2.13)

Case 2: High RH

For equilibrium case (2), we have an equilibrium solution

$$m_s^{eq} = m_s^{max},$$

$$m_w^{eq} = \frac{RH}{1 - RH} \frac{M_w}{M_s} m_s^{max}.$$

Substituting the equilibrium solution into the linearized matrix after perturbation, we have

$$\frac{d}{dt} \begin{bmatrix} \tilde{m}_w \\ \tilde{m}_s \end{bmatrix} = \sigma E(T) \sqrt{\frac{M}{2\pi k_B T}} \begin{bmatrix} -(1 - RH)^2 \frac{M_s}{m_s^{max} M_w} & \frac{RH(1 - RH)}{m_s^{max}} \\ 0 & 0 \end{bmatrix} \begin{bmatrix} \tilde{m}_w \\ \tilde{m}_s \end{bmatrix}$$

with eigenvalues

$$\lambda_1 = 0,$$

and

$$\lambda_2 = -(1 - RH)^2 \frac{M_s}{m_s^{max} M_w} < 0.$$

Since one of the eigenvalues is zero, we further investigate the second order terms from the perturbed equations. Substitute the equilibrium solution into equation (2.39) and (2.40), we have

$$\begin{aligned} \frac{d}{dt} \tilde{m}_w &= \frac{\sigma E(T) \sqrt{\frac{M}{2\pi k_B T}} (1 - RH)}{m_s^{max} M_w} \left(-RH M_w m_s^{max} \tilde{m}_w + \left(\frac{(RH M_w)^2 m_s^{max}}{(1 - RH) M_s} \right) \tilde{m}_s \right) \\ &\quad + \frac{\sigma E(T) \sqrt{\frac{M}{2\pi k_B T}} (1 - RH)}{m_s^{max} M_w} (M_s RH \tilde{m}_w^2 + M_w RH \tilde{m}_w \tilde{m}_s), \\ \frac{d}{dt} \tilde{m}_s &= \frac{D(1 - RH) M_s}{(RH M_w + (1 - RH) M_s) (m_s^{max})^2} ((\rho_0 - C_s) \tilde{m}_s^2 - C_s \tilde{m}_w \tilde{m}_s). \end{aligned}$$

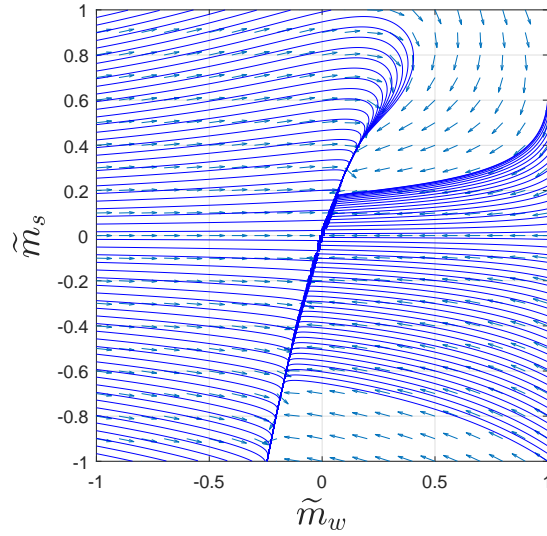


Figure 2.17: The phase portrait with streamlines for the above ODE system of \tilde{m}_s and \tilde{m}_w . If we perturbed the solutions close enough to the origin, the perturbation converges to zero. Therefore, the system is stable at high RH, and the perturbation around the equilibria will converge to the red dot (equilibrium point) in Figure (2.14)

Case 3: Low RH

For case (3), we have a critical solution

$$\begin{aligned} m_w^{eq} &= 0, \\ m_s^{eq} &= 0. \end{aligned}$$

To find the stability at the singular point, let

$$\begin{aligned} \tilde{m}_w &= m_w^{eq} + \epsilon = \epsilon, \\ \tilde{m}_s &= m_s^{eq} + \delta = \delta. \end{aligned}$$

Since for low RH, evaporation dominates equation (2.28), the water mass decreases over time. Therefore, along the x-axis in figure (2.15), the vector field always points to the origin. As water mass decreases, salt precipitates out. Hence, in order to find the condition of having negative direction of the vector field along y-axis, substitute \tilde{m}_w and \tilde{m}_s into equation (2.29) and set $m'_s(t) < 0$, we have

$$\delta'(t) = D \left(C_s - \frac{\delta \rho_0}{\epsilon} \right) \left(1 - \frac{\delta}{m_s^{max}} \right) < 0, \quad (2.41)$$

and

$$\delta > \frac{\epsilon C_s}{\rho_0}. \quad (2.42)$$

As long as the perturbation is in the region bounded by $\delta > \frac{\epsilon C_s}{\rho_0}$, we have the decreases in $m_s(t)$. While this is not enough to show equation (2.41) approaches the singular point. Now, look at the equation (2.41) in terms of δ (m_s) only to see if the critical points are stable. The critical points are

$$\delta = \frac{\epsilon C_s}{\rho_0},$$

and

$$\delta = m_s^{max}.$$

- When $\frac{\epsilon C_s}{\rho_0} < \delta < m_s^{max}$, $\delta'(t)$ is negative and approaches the critical point $\frac{\epsilon C_s}{\rho_0}$.

- When $0 < \delta < \frac{\epsilon C_s}{\rho_0}$, $\delta'(t)$ is positive, and approaches the critical point $\frac{\epsilon C_s}{\rho_0}$.

Look at the limit of the critical point $\frac{\epsilon C_s}{\rho_0}$ when ϵ approaches zero, we have

$$\lim_{\epsilon \rightarrow 0} \delta = \lim_{\epsilon \rightarrow 0} \frac{\epsilon C_s}{\rho_0} = 0. \quad (2.43)$$

We can conclude that when $0 < \delta < m_s^{max}$, the solution approaches the critical point of the equation (2.41). And moreover, the critical point approaches zero when evaporation dominates equation 2.28 ($RH < RH_0$). Hence the singular point (0,0) is stable.

Model Simulation

If we assume the salt on the stone is calcium nitrate ($Ca(NO_2)_2$), the critical relative humidity (RH_0) is 0.4646 or 46.46% (Table (2.5)).

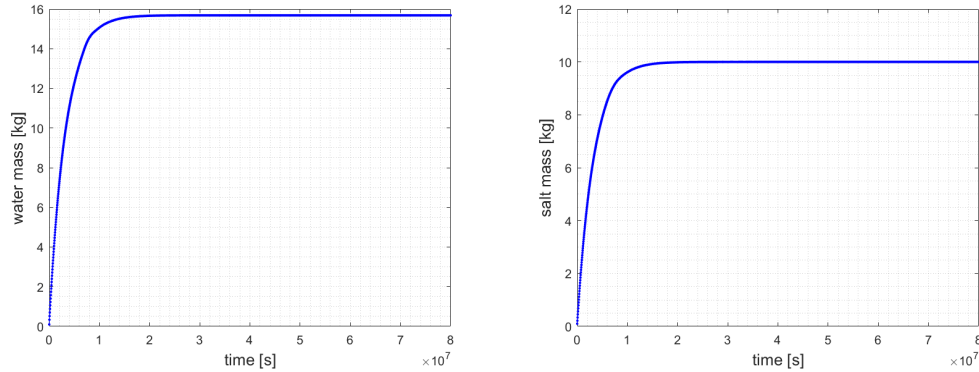


Figure 2.18: Water mass (left) and salt mass (right). Parameters: see table 2.4 and $RH = 90\% > RH_0$. Initial condition: $m_w = 0.1kg$, $m_s = 0.1kg$. Since the actual RH is greater than RH_0 , water mass and salt mass increase in time. All the available salt in the system dissolves into the water and water vapor condenses into the solution to reach the equilibrium point for high RH.

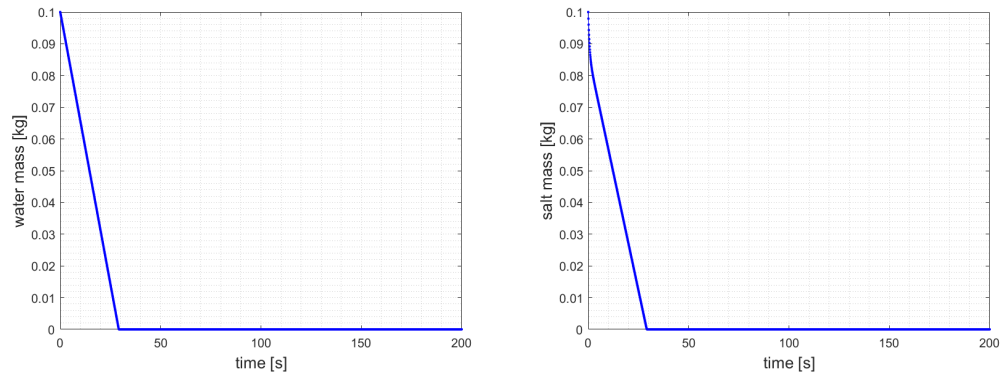


Figure 2.19: Water mass (left) and salt mass (right). Parameters: see table 2.4 and $RH = 40\% < RH_0$. Initial condition: $m_w = 0.1kg$, $m_s = 0.1kg$. When the actual RH is lower than RH_0 , both of the masses decrease to zero (the singular point) in time. Salt precipitates into solid phase and water in the solution evaporates into the air.

2.2.4 Deliquescence Model with Biofilm

In this model, we add biomass into consideration. Biofilm growth uptakes water and CO_2 , while here we assume CO_2 is in abundance, and water mass in the system is the only constraint for biofilm growth.

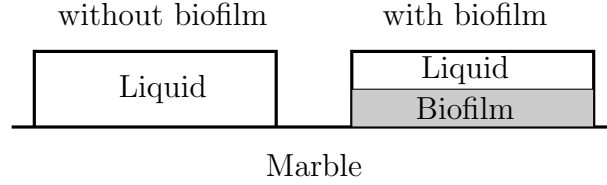


Figure 2.20: Comparison of bare marble and biofilm covering marble

Model Setup

The ODE system for deliquescence model with biofilm is

$$m'_w(t) = \sqrt{\frac{M}{2\pi k_B}} \left(\sigma_c \frac{P_v}{\sqrt{T_V}} - \sigma_e \frac{P_s(T_L)}{\sqrt{T_L}} \right) - \eta m_b(t) m_w(t), \quad (2.44)$$

$$m'_s(t) = D \left(C_s - \frac{m_s(t)\rho_0}{m_w(t)} \right) \left(1 - \frac{m_s(t)}{m_s^{max}} \right), \quad (2.45)$$

$$m'_b(t) = \eta Y m_w(t) m_b(t) \left(1 - \frac{m_b(t)}{N} \right), \quad (2.46)$$

where m_b is the biomass in the system, η is the photosynthesis rate which is small, Y is the yield constant between units, and N is the carrying capacity of biofilm. The carrying capacity of biofilm in the environment is the maximum population size that the environment can sustain indefinitely, given the food, habitat, water, and other necessities available in the environment. We consider that biofilm growth consumes water and CO_2 , therefore we have an extra term in equation (2.44) describes the water uptake during the process. Equation (2.46) describes the growth of biomass. Biomass increases when there is available water in the environment and the biomass is below the carrying capacity, while it stops growing otherwise. This term is different from the water uptake term from photosynthesis in equation (2.44) by multiplying a logistic term

$1 - \frac{m_b(t)}{N}$ to limit the exponential growth of biomass. When biomass reaches its carrying capacity, biomass stops increases but the existed biofilm uptakes water to survive (in chapter 2.3, we consider the death rate of biomass).

After simplification with the same settings from the previous model, we have,

$$m'_w(t) = \sigma E \sqrt{\frac{M}{2\pi k_B T}} \left(RH - \frac{\frac{m_w(t)}{M_w}}{\frac{m_w(t)}{M_w} + \frac{m_s(t)}{M_s}} \right) - \eta m_b(t) m_w(t), \quad (2.47)$$

$$m'_s(t) = D \left(C_s - \frac{m_s(t) \rho_0}{m_w(t)} \right) \left(1 - \frac{m_s(t)}{m_s^{max}} \right), \quad (2.48)$$

$$m'_b(t) = \eta Y m_w(t) m_b(t) \left(1 - \frac{m_b(t)}{N} \right). \quad (2.49)$$

Critical Relative Humidity

To find the RH_0 in this model, let $m_w(t)$, $m_s(t)$, and $m_b(t)$ be time independent. Set $m'_w(t) = 0$, $m'_s(t) = 0$, and $m'_b(t) = 0$, we have

$$0 = m'_w(t) = \sigma E \sqrt{\frac{M}{2\pi k_B T}} (RH - r_w) - \eta m_b m_w, \quad (2.50)$$

$$0 = m'_s(t) = D \left(C_s - \frac{m_s \rho_0}{m_w} \right) \left(1 - \frac{m_s}{m_s^{max}} \right), \quad (2.51)$$

$$0 = m'_b(t) = \eta Y m_b m_w \left(1 - \frac{m_b}{N} \right). \quad (2.52)$$

When $RH = RH_0$, solving equation (2.50 - 2.52), we have

$$RH_0 = \frac{\frac{m_w^{eq}}{M_w}}{\frac{m_w^{eq}}{M_w} + \frac{m_s^{eq}}{M_s}} + \frac{\eta m_b^{eq} m_w^{eq}}{\sigma E(T) \sqrt{\frac{M}{2\pi k_B T}}}. \quad (2.53)$$

Compared with the RH_0 (equation (2.53)) derives from the model without biofilm, RH_0 increases in this model. The second term in the expression of RH_0 is the increment of relative humidity under the influence of photosynthesis. Biofilm growth uptakes water and lower the ratio of the number of water molecules among all the molecules (r_w), which means we need to have a higher RH_0 to balance the equilibrium. Since $\frac{\eta m_b^{eq} m_w^{eq}}{\sigma E(T) \sqrt{\frac{M}{2\pi k_B T}}} \geq 0$, RH_0 might be slightly

greater than 1 when $RH = 100\%$ ($r_w = 1$ at equilibrium), in this case RH is always smaller than RH_0 . Under this circumstance, the system could be in low RH case (case (4)), and the solution of the system decreases to zero even with relatively high RH.

- When $RH > RH_0$, $m'_w(t) > 0$. Water mass increases because condensation dominates equation (2.50). The ratio $c(t)$ decreases as m_w increases, as a result, salt dissolution dominates equation (2.51) and $m'_s(t) > 0$. The masses of salt and water increase until all the available salt dissolves into the solution and biomass reaches the carrying capacity.
- When $RH < RH_0$, $m'_w(t) < 0$. Evaporation of water dominates equation (2.50), and we have a decreasing amount of water. As water mass decreases, the solution becomes supersaturated, and salt precipitates at the same time. Therefore both of the masses decrease to zero and biofilm stops growing. However, it is possible that $RH_0 > 1$, and we will never reach a relative humidity which exceeds the RH_0 .
- When $RH = RH_0$, $m'_w(t) = 0$. There are no mass fluxes on the air-liquid and stone-liquid interfaces, while as long as the water mass does not hit zero and biomass below the carrying capacity, we still have the increase in biomass.

Equilibrium Solution

- Case (1). When $m_b = 0$, there is no biomass in the system. This model is as the same as the previous model which has three sub cases.
 - When $RH = RH_0$, the equilibrium solutions are

$$m_s^{eq} = \frac{C_s}{\rho_0} m_w^{eq},$$

$$m_b^{eq} = 0.$$

– When $RH > RH_0$, the equilibrium solutions are

$$\begin{aligned} m_w^{eq} &= \frac{RH}{1 - RH} \frac{M_w}{M_s} m_s^{max}, \\ m_s^{eq} &= m_s^{max}, \\ m_b^{eq} &= 0. \end{aligned}$$

– When $RH < RH_0$, the equilibrium solutions are

$$\begin{aligned} m_w^{eq} &= 0, \\ m_s^{eq} &= 0, \\ m_b^{eq} &= 0. \end{aligned}$$

- Case (2). When $RH = RH_0 = \frac{\frac{m_w^{eq}}{M_w}}{\frac{m_w^{eq}}{M_w} + \frac{m_s^{eq}}{M_s}} + \frac{\eta m_b^{eq} m_w^{eq}}{\sigma E(T) \sqrt{\frac{M}{2\pi k_B T}}}$, $C_s = \frac{m_s^{eq} \rho_0}{m_w^{eq}}$, $m_b^{eq} = N$, the equilibrium solutions for case (2) are

$$\begin{aligned} m_w^{eq} &= \frac{\left(RH_0 - \frac{1}{1 + \frac{C_s M_w}{\rho_0 M_s}} \right) \sigma E(T) \sqrt{\frac{M}{2\pi k_B T}}}{\eta N}, \\ m_s^{eq} &= \frac{C_s}{\rho_0} m_w^{eq}, \\ m_b^{eq} &= N. \end{aligned}$$

The critical case in the model without biofilm has infinitely many solutions, while here the solution is unique. In the previous case, we obtain the steady state as long as RH equals to the percentage of the number of water molecules among all the molecules in the solution, but this case we have biomass involved and it will uptake water to break the stability. Hence, the solution is unique.

- Case (3). When $RH > RH_0 = \frac{\frac{m_w^{eq}}{M_w}}{\frac{m_w^{eq}}{M_w} + \frac{m_s^{eq}}{M_s}} + \frac{\eta m_b^{eq} m_w^{eq}}{\sigma E(T) \sqrt{\frac{M}{2\pi k_B T}}}$, $m_s^{eq} = m_s^{max}$,

$m_b^{eq} = N$, the equilibrium solutions for case (3) are

$$m_w^{eq} = \frac{\left(RH_0 - \frac{1}{1 + \frac{C_s M_w}{\rho_0 M_s}}\right) \sigma E(T) \sqrt{\frac{M}{2\pi k_B T}}}{\eta N},$$

$$m_s^{eq} = m_s^{max},$$

$$m_b^{eq} = N.$$

- Case (4). When $RH < RH_0$, $m_w^{eq} = 0$, $m_s^{eq} = 0$. The equilibria for case (4) is

$$m_w^{eq} = 0,$$

$$m_s^{eq} = 0,$$

$$m_b^{eq} = K,$$

where K is a number between 0 and carrying capacity N . When the masses of water and salt are zero, the system reaches the equilibrium and the mass of biofilm stays the same which does not affect the stability. Also, this critical point is a singularity of the system.

Stability Analysis

To check the stability of the equilibrium solutions, perturb m_s , m_w , and m_b around the equilibria, and set

$$m_s = m_s^{eq} + \tilde{m}_s, \tag{2.54}$$

$$m_w = m_w^{eq} + \tilde{m}_w, \tag{2.55}$$

$$m_b = m_b^{eq} + \tilde{m}_b. \tag{2.56}$$

Substituting equation (2.54) - (2.56) into equation (2.44) - (2.46) and ignoring the higher order terms, we have,

$$\begin{aligned} \frac{d}{dt}\tilde{m}_w &= \left(\frac{\sigma E(T)\sqrt{\frac{M}{2\pi k_B T}}(RH-1)M_s}{m_w^{eq}M_s + m_s^{eq}M_w} - \eta m_b^{eq} \right) \tilde{m}_w \\ &\quad + \left(\frac{\sigma E(T)\sqrt{\frac{M}{2\pi k_B T}}RH M_w}{m_w^{eq}M_s + m_s^{eq}M_w} \right) \tilde{m}_s - \eta m_w^{eq} \tilde{m}_b, \end{aligned} \quad (2.57)$$

$$\frac{d}{dt}\tilde{m}_s = D \left(\frac{(m_s^{eq} - m_s^{max})\rho_0}{m_w^{eq}m_s^{max}} \tilde{m}_s + \frac{C_s(m_s^{max} - m_s^{eq})}{m_w^{eq}m_s^{max}} \right) \tilde{m}_w, \quad (2.58)$$

$$\frac{d}{dt}\tilde{m}_b = Y \left(\eta m_w^{eq} - \frac{2\eta}{N} m_w^{eq} m_b^{eq} \right) \tilde{m}_b + Y \left(\eta m_b^{eq} \left(1 - \frac{1}{N} \right) \right) \tilde{m}_w. \quad (2.59)$$

We can write the above equations as a linear system

$$\frac{d}{dt} \begin{bmatrix} \tilde{m}_w \\ \tilde{m}_s \\ \tilde{m}_b \end{bmatrix} = \begin{bmatrix} AM_s(RH-1) - \eta m_b^{eq} & AM_w RH & -\eta m_w^{eq} \\ BC_s & -B\rho_0 & 0 \\ Y\eta m_b^{eq} \left(1 - \frac{1}{N}\right) & 0 & Y\eta m_w^{eq} \left(1 - \frac{2}{N} m_b^{eq}\right) \end{bmatrix} \begin{bmatrix} \tilde{m}_w \\ \tilde{m}_s \\ \tilde{m}_b \end{bmatrix},$$

where

$$\begin{aligned} A &= \frac{\sigma E(T)\sqrt{\frac{M}{2\pi k_B T}}}{m_w^{eq}M_s + m_s^{eq}M_w} > 0, \\ B &= \frac{D(m_s^{max} - m_s^{eq})}{m_w^{eq}m_s^{max}} > 0, \end{aligned}$$

Note $A, B > 0$ **Case 1: No biofilm**

When $m_b^{eq} = 0$, there are three sub cases corresponding to different RH.

Sub Case 1: Critical RH

The perturbed matrix of the system is

$$\frac{d}{dt} \begin{bmatrix} \tilde{m}_w \\ \tilde{m}_s \\ \tilde{m}_b \end{bmatrix} = \begin{bmatrix} AM_s(RH-1) & AM_w RH & -\eta m_w^{eq} \\ BC_s & -B\rho_0 & 0 \\ 0 & 0 & \eta m_w^{eq} \end{bmatrix} \begin{bmatrix} \tilde{m}_w \\ \tilde{m}_s \\ \tilde{m}_b \end{bmatrix}.$$

The eigenvalues of the above matrix are:

$$\begin{aligned} \lambda_1 &= 0, \\ \lambda_2 &= A(RH-1)M_s + -B\rho_0 < 0, \\ \lambda_3 &= \eta m_w^{eq} > 0, \end{aligned}$$

and eigenvectors

$$v_1 = \begin{bmatrix} -\frac{M_w RH}{M_s(RH-1)} \\ 1 \\ 0 \end{bmatrix}, v_2 = \begin{bmatrix} \frac{A(RH-1)M_s}{BC_s} \\ 1 \\ 0 \end{bmatrix},$$

$$v_3 = \begin{bmatrix} \frac{\eta m_w^{eq} + B\rho_0}{BC_s} \\ 1 \\ \frac{(AM_s(RH-1) - \eta m_w^{eq})(\eta m_w^{eq} + B\rho_0) + ABC_s M_w RH}{BC_s \eta m_w^{eq}} \end{bmatrix}.$$

The first two eigenvalues λ_1 and λ_2 are as the same as the critical RH case without biofilm, and the last eigenvalue λ_3 is related to photosynthesis and biofilm growth. Since λ_3 is positive, the equilibrium point in this case is a saddle point which is unstable. Correspondingly, the third entry in eigenvector v_3 is the growth of biofilm.

Sub Case 2: High RH

For the high RH case, we have an equilibrium solution

$$m_s^{eq} = m_s^{max},$$

$$m_w^{eq} = \frac{RH}{1-RH} \frac{M_w}{M_s} m_s^{max},$$

$$m_b^{eq} = 0.$$

The perturbed matrix of the system is

$$\frac{d}{dt} \begin{bmatrix} \tilde{m}_w \\ \tilde{m}_s \\ \tilde{m}_b \end{bmatrix} = \begin{bmatrix} -C(1-RH)^2 \frac{M_s}{m_s^{max} M_w} & C \frac{RH(1-RH)}{m_s^{max}} & -\eta m_w^{eq} \\ 0 & 0 & 0 \\ 0 & 0 & \eta m_w^{eq} \end{bmatrix} \begin{bmatrix} \tilde{m}_w \\ \tilde{m}_s \\ \tilde{m}_b \end{bmatrix},$$

where $C = \sigma E(T) \sqrt{\frac{M}{2\pi k_B T}}$. The above matrix has eigenvalues

$$\lambda_1 = 0,$$

$$\lambda_2 = -C(1-RH)^2 \frac{M_s}{m_s^{max} M_w} < 0,$$

$$\lambda_3 = \eta m_w^{eq} > 0,$$

and eigenvectors

$$v_1 = \begin{bmatrix} -\frac{M_w RH}{M_s(RH-1)} \\ 1 \\ 0 \end{bmatrix}, v_2 = \begin{bmatrix} 1 \\ 0 \\ 0 \end{bmatrix}, v_3 = \begin{bmatrix} \frac{\eta m_w^{eq}}{-C(1-RH)^2 \frac{M_s}{m_s^{max}} M_w - \eta m_w^{eq}} \\ 0 \\ 1 \end{bmatrix}.$$

The first two eigenvalues (λ_1, λ_2) and eigenvectors (v_1, v_2) are the same as the high RH case without biofilm (case 2 in the previous model, see chapter 2.2.3), and the last one is related to photosynthesis and biofilm growth. λ_3 is the positive eigenvalue, and along the eigenvector v_3 , the water turn into biomass if it doesn't reach the carrying capacity. Therefore, the system is unstable.

Sub Case 3: Low RH

For low RH case, we have an equilibrium solution

$$m_w^{eq} = 0,$$

$$m_s^{eq} = 0,$$

$$m_b^{eq} = 0.$$

To find the stability at the singular point, let

$$\tilde{m}_w = m_w^{eq} + \epsilon_1 = \epsilon_1,$$

$$\tilde{m}_s = m_s^{eq} + \epsilon_2 = \epsilon_2,$$

$$\tilde{m}_b = m_b^{eq} + \epsilon_3 = \epsilon_3.$$

Since for low RH, evaporation dominates equation (2.47), the water mass decreases over time. Therefore, along direction of the vector space of water mass, the vector field always points to the negative direction. The growth of biomass is depending on the water mass, and so far, we assume the biomass is non-decreasing. Once water mass decreases to zero, the biomass stops growing. In order to find the condition of having negative direction of the vector field along the direction of the vector field of salt mass, substitute ϵ_1 and ϵ_2 into equation (2.48) and set $\epsilon'_2(t) < 0$, we have

$$\epsilon'_2(t) = D \left(C_s - \frac{\epsilon_2 \rho_0}{\epsilon_1} \right) \left(1 - \frac{\epsilon_2}{m_s^{max}} \right) < 0. \quad (2.60)$$

we need

$$C_s < \frac{\epsilon_2 \rho_0}{\epsilon_1},$$

As long as the perturbation is in the region bounded by $\epsilon_2 > \frac{\epsilon_1 C_s}{\rho_0}$, we have the decreases in ϵ_2 . While this is not enough to show equation (2.60) is approaching the singular point. Now, look at the equation (2.60) in terms of ϵ_2 (m_s) only to see if the critical points are stable. The critical points are

$$\epsilon_2 = \frac{\epsilon_1 C_s}{\rho_0},$$

and

$$\epsilon_2 = m_s^{max}.$$

- When $\frac{\epsilon_1 C_s}{\rho_0} < \epsilon_2 < m_s^{max}$. Equation (2.60) is negative, and approaches the critical point $\frac{\epsilon_1 C_s}{\rho_0}$.
- When $0 < \epsilon_2 < \frac{\epsilon_1 C_s}{\rho_0}$. Equation (2.60) is positive, and approaches the critical point $\frac{\epsilon_1 C_s}{\rho_0}$.

Look at the limit of the critical point $\frac{\epsilon_1 C_s}{\rho_0}$ when ϵ_1 approaches zero, we have

$$\lim_{\epsilon_1 \rightarrow 0} \epsilon_2 = \lim_{\epsilon_1 \rightarrow 0} \frac{\epsilon_1 C_s}{\rho_0} = 0. \quad (2.61)$$

We can conclude that when $0 < \epsilon_2 < m_s^{max}$, the solution approaches the critical point of the equation (2.60). And moreover, the critical point approaches zero when evaporation dominates equation 2.47 ($RH < RH_0$). The biomass will stay after the perturbation. Hence, after the perturbation ($\epsilon_1, \epsilon_2, \epsilon_3$), the solution will converge to $(0,0,\epsilon_3)$. The singular point $(0,0,0)$ is stable.

Case 2: Critical RH

The equilibrium solution at the critical RH with biomass is

$$\begin{aligned} m_w^{eq} &= \frac{\left(RH_0 - \frac{1}{1 + \frac{C_s M_w}{\rho_0 M_s}} \right) C}{\eta N}, \\ m_s^{eq} &= \frac{C_s}{\rho_0} m_w^{eq}, \\ m_b^{eq} &= N. \end{aligned}$$

The matrix after perturbation at the critical RH is

$$\frac{d}{dt} \begin{bmatrix} \tilde{m}_w \\ \tilde{m}_s \\ \tilde{m}_b \end{bmatrix} = \begin{bmatrix} AM_s(RH - 1) - \eta N & AM_w RH & -\eta m_w^{eq} \\ BC_s & -B\rho_0 & 0 \\ \eta(N - 1) & 0 & -\eta m_w^{eq} \end{bmatrix} \begin{bmatrix} \tilde{m}_w \\ \tilde{m}_s \\ \tilde{m}_b \end{bmatrix},$$

The characteristic polynomial for the above matrix is

$$\begin{aligned} &(\lambda - AM_s(RH - 1) + \eta N)(\lambda + B\rho_0)(\lambda + \eta m_w^{eq}) \\ &+ \eta m_w^{eq}(\lambda + B\rho_0)\eta(N - 1) - (\lambda + \eta m_w^{eq})AM_w RH BC_s = 0. \end{aligned}$$

To solve for λ , we expanded the above expression, we have

$$\begin{aligned} &\lambda^3 + \lambda^2(-AM_s(RH - 1) + \eta N + B\rho_0 + \eta m_w^{eq}) \\ &+ \lambda B\rho_0 \eta m_w^{eq} - (AM_s(RH - 1) - \eta N)\eta m_w^{eq} - B\rho_0(AM_s(RH - 1) - \eta N) \\ &+ (AM_s(RH - 1) - \eta N)(-B\rho_0)\eta m_w^{eq} + \eta^2 m_w^{eq}(\lambda + B\rho_0)(N - 1) \\ &- (\lambda + \eta m_w^{eq})AM_w RH BC_s = 0 \end{aligned}$$

Since it is hard to find the signs of the eigenvalues from this characteristic polynomial, we approximate the eigenvalues with the ones from the previous model (deliquescence model without biofilm). We have two eigenvalues from the previous model, while in this model we have three eigenvalues and the third eigenvalue comes from the growth of biomass. The approximated eigenvalues are

$$\begin{aligned} \tilde{\lambda}_1 &= \lambda_1 + \eta \hat{\lambda}_1, \\ \tilde{\lambda}_2 &= \lambda_2 + \eta \hat{\lambda}_2, \\ \tilde{\lambda}_3 &= \eta \hat{\lambda}_3, \end{aligned}$$

where

$$\begin{aligned} \lambda_1 &= 0, \\ \lambda_2 &= A(RH - 1)M_s - B\rho_0 < 0. \end{aligned}$$

Substituting the approximated eigenvalues into the characteristic polynomial and solve for the $\hat{\lambda}$. The sign of $\hat{\lambda}$ combined with the sign of λ will tell us the stability of the approximated eigenvalues $\tilde{\lambda}$.

When $\tilde{\lambda}_1 = \eta\hat{\lambda}_1$, ignoring the higher order terms of η , we have,

$$\begin{aligned} & -\eta\hat{\lambda}_1 B\rho_0 AM_s(RH-1) - (\eta\hat{\lambda}_1 + \eta m_w^{eq})AM_w RHBC_s - AM_s(RH-1)B\rho_0\eta m_w^{eq} = 0, \\ & -\hat{\lambda}_1 B\rho_0 AM_s(RH-1) - \hat{\lambda}_1 AM_w RHBC_s - m_w^{eq} AM_w RHBC_s = 0. \end{aligned}$$

After simplification, we have

$$\hat{\lambda}_1 = \frac{m_w^{eq}(M_w RHC_s + M_s(RH-1)\rho_0)}{-M_s(RH-1)\rho_0 - M_w RHC_s} = -m_w^{eq} < 0. \quad (2.62)$$

Hence, $\tilde{\lambda}_1 = \lambda_1 + \eta\hat{\lambda}_1 = \hat{\lambda}_1 < 0$. Since $\tilde{\lambda}_3 = \eta\hat{\lambda}_3$ has the same structure as $\tilde{\lambda}_1$, $\tilde{\lambda}_3$ is also negative.

When $\tilde{\lambda}_2 = \lambda_2 + \eta\hat{\lambda}_2$, the eigenvalue from the previous model λ_2 is negative, and η is small compare to $\hat{\lambda}_2$, the small perturbation does not affect the sign of the eigenvalue. Hence, $\tilde{\lambda}_2$ is also negative. Since all the eigenvalues are negative, the system at critical RH is stable for asymptotically small η .

Case 3: High RH

The equilibrium solution at high RH is

$$\begin{aligned} m_w^{eq} &= \frac{\left(RH_0 - \frac{1}{1 + \frac{C_s M_w}{\rho_0 M_s}}\right) C}{\eta N}, \\ m_s^{eq} &= m_s^{max}, \\ m_b^{eq} &= N. \end{aligned}$$

After substituting the solution into the matrix, we have

$$\frac{d}{dt} \begin{bmatrix} \tilde{m}_w \\ \tilde{m}_s \\ \tilde{m}_b \end{bmatrix} = \begin{bmatrix} \frac{CM_s(RH-1)}{m_w^{eq}M_s + m_s^{max}M_w} - \eta N & \frac{CM_w RH}{m_w^{eq}M_s + m_s^{max}M_w} & -\eta m_w^{eq} \\ 0 & 0 & 0 \\ \eta(N-1) & 0 & -\eta m_w^{eq} \end{bmatrix} \begin{bmatrix} \tilde{m}_w \\ \tilde{m}_s \\ \tilde{m}_b \end{bmatrix}.$$

The characteristic polynomial of the matrix is

$$\lambda(\eta(N-1))(-\eta m_w^{eq}) - \lambda \left(\left(\frac{CM_s(RH-1)}{m_w^{eq}M_s + m_s^{max}M_w} \right) - \eta N - \lambda \right) (-\eta m_w^{eq} - \lambda) = 0. \quad (2.63)$$

Since the growth rate η is small in equation (2.63), ignoring the higher order terms of η , we have,

$$\lambda \left(\left(\frac{CM_s(RH-1)}{m_w^{eq}M_s + m_s^{max}M_w} \right) - \eta N - \lambda \right) (-\eta m_w^{eq} - \lambda) = 0. \quad (2.64)$$

The approximate eigenvalues of the above system is,

$$\begin{aligned} \lambda_1 &= \left(\frac{CM_s(RH-1)}{m_w^{eq}M_s + m_s^{max}M_w} \right) - \eta N < 0, \\ \lambda_2 &= -\eta m_w^{eq} < 0, \\ \lambda_3 &= 0. \end{aligned}$$

Since two of the eigenvalues are negative, the stability of the system depends on λ_3 . The approximate eigenvector for λ_3 is

$$v_3 = \begin{bmatrix} \frac{m_w^{eq}}{N-1} \\ -\frac{m_w^{eq}M_s + m_s^{max}M_w}{CM_wRH} \eta m_w^{eq} - \frac{M_s(RH-1)m_w^{eq}}{M_wRH(N-1)} \\ 1 \end{bmatrix}$$

Since $\frac{m_w^{eq}}{N-1} < 0 < 1$, $-\frac{m_w^{eq}M_s + m_s^{max}M_w}{CM_wRH} \eta m_w^{eq} - \frac{M_s(RH-1)m_w^{eq}}{M_wRH(N-1)} < 0 < 1$, and biomass is a non-decreasing variable, the system is stable at high RH for asymptotically small η .

Case 4: Low RH

The equilibrium solution at low RH is

$$\begin{aligned} m_w^{eq} &= 0, \\ m_s^{eq} &= 0, \\ m_b^{eq} &= K. \end{aligned}$$

The stability at this equilibrium solution is similar to the proof in the low RH case when $m_b = 0$. This is a stable equilibria.

Model Simulation

Assume that the salt exists on the stone is calcium nitrate ($Ca(NO_2)_2$), then the critical relative humidity (RH_0) is 0.4646 or 46.46% (Table (2.5)).

High RH

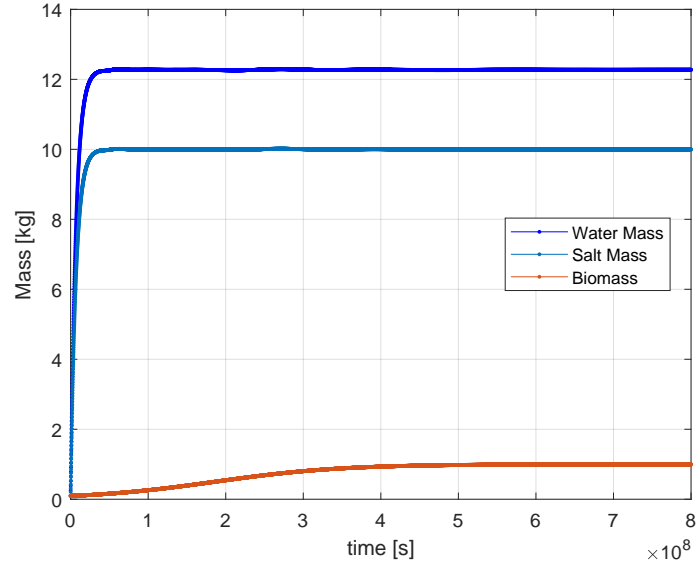


Figure 2.21: Plot of water mass, salt mass, and biomass. Parameters: see table (2.4), $\eta = 10^{-6}$, $N = 1$ and $RH = 90\% > RH_0$. Initial conditions: $m_w = 0.1kg$, $m_s = 0.1kg$, $m_b = 0.1$. The water and salt masses increase to the equilibrium, all the available salt dissolves into the solution, and biomass reaches the carrying capacity.

Low RH

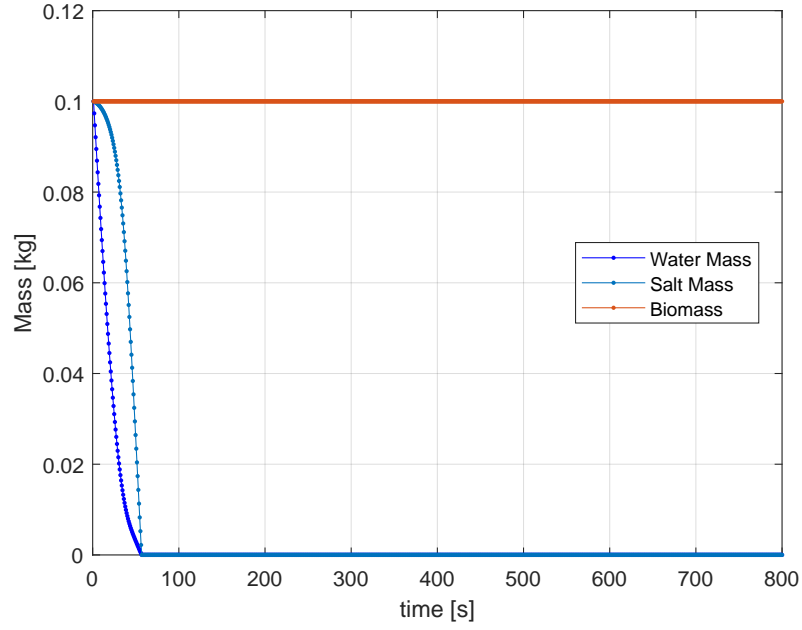


Figure 2.22: Plot of water mass, salt mass, and biomass. Parameters: see table (2.4), $\eta = 10^{-6}$, $N = 1$ and $RH = 50\% < RH_0$. Initial conditions: $m_w = 0.1kg$, $m_s = 0.1kg$, $m_b = 0.1$. The actual RH is lower than RH_0 for the model without biofilm, which is also lower than RH_0 for the model with biofilm. The mass of water and the mass of salt decrease to zero in time, and biofilm stops growing once the mass of water hits zero. The salt precipitates into solid phase and the water in the solution evaporates into the air.

In the above simulation, we assume the constant relative humidity and temperature, but this setting is not realistic in nature. We will apply the real data to the model later in this project.

2.2.5 Conclusion and Discussion

Model without Biofilm

In the deliquescence model without biofilm, we derive a formula for critical relative humidity (RH_0) for different salt depending on the molecular mass and solubility. When $RH > RH_0$, water vapor condensation dominates equation (2.28) and salt dissolution dominates equation (2.29). The mass of water increases until all the available salt dissolved into the solution, and water mass also approaches the equilibrium (shown in figure 2.18). Moreover, this equilibrium is stable. When $RH < RH_0$, water evaporation dominates equation (2.28) and salt precipitation dominates equation (2.29). The mass of water decreases and salt precipitates out into its solid phase, both of the two masses approaches the singular point (0,0) (shown in figure 2.19). This critical point of the ode system is also stable after analysis. When $RH = RH_0$, there is no mass flux on the liquid-air and stone/salt-air interfaces. At this equilibrium, the percentage of water molecules in the solution equals the percentage of vapor water in the air, and the system is perfectly balanced. In this critical relative humidity case, the system is also stable. We obtain the water and salt masses for biofilm living environment from this model, which can be used for the next model to simulate biofilm growth.

Model with Biofilm

In the deliquescence model with biofilm, we add biomass into the previous model. Photosynthesis process uptakes the available water on the marble, which causes the decrease in water mass. When $RH > RH_0$, water vapor condensation dominates equation (2.47), salt dissolution dominates equation (2.48), and biomass increases in equation (2.49) until reaches its carrying capacity N (shown in figure 2.21). The equilibrium point at high RH is stable after analysis. When $RH < RH_0$, water evaporation dominates equation (2.47), salt precipitation dominates equation (2.48), and biomass stop increases in equation (2.49) when water mass approaches zero (shown in figure 2.22). If

we perturb the equilibrium solution, water mass and salt mass approach zero, while the biomass is non-decreasing. When $RH = RH_0$, there is no mass flux on the liquid-air and stone/salt-air interfaces, and this equilibrium is stable. From the simulation result, we can conclude that when the outside RH is large (compared with RH_0), biomass increases and biomass stays the same with low RH (compared with RH_0). In the next section, we will apply time series data to the model and compare biofilm growth rate in different weathers.

2.3 Simulation with Time Series Data

2.3.1 Data Visualization

We set up a weather station for almost two years on the roof of Jefferson memorial near biofilm habitation on marble, measured local weather data. In this section, we apply the time series data to our model. In the weather station, we had four ibuttons measuring temperature in Celsius, one ibutton measured relative humidity in % (shown in figure 2.23), a rain gauge (shown in figure 2.24 middle and right), and a light sensor measured Photosynthetically Active Radiation (PAR, in micromoles of photons per meter squared per second, $\mu\text{mol} \cdot \text{m}^{-2} \cdot \text{s}^{-1}$) (shown in figure 2.24 left). In our model, temperature and humidity are two weather data related to water and salt masses on the marble, which also determine the activity of biofilm growth. We select four sample days in each of summer and winter to demonstrate the data we collect from these four meters (shown in figure 2.25 and 2.26).



Figure 2.23: ibuttons (left) and one of the ibuttons on the roof of JM (right).
ibuttons recorded temperature and humidity of the air near the marble.



Figure 2.24: Light sensor (left : *LI-190R Quantum Sensor*) and rain gauge (middle and right : *RG3 Onset Hobo Rain Gauge Data Logger*) measured light intensity and precipitation on the roof.

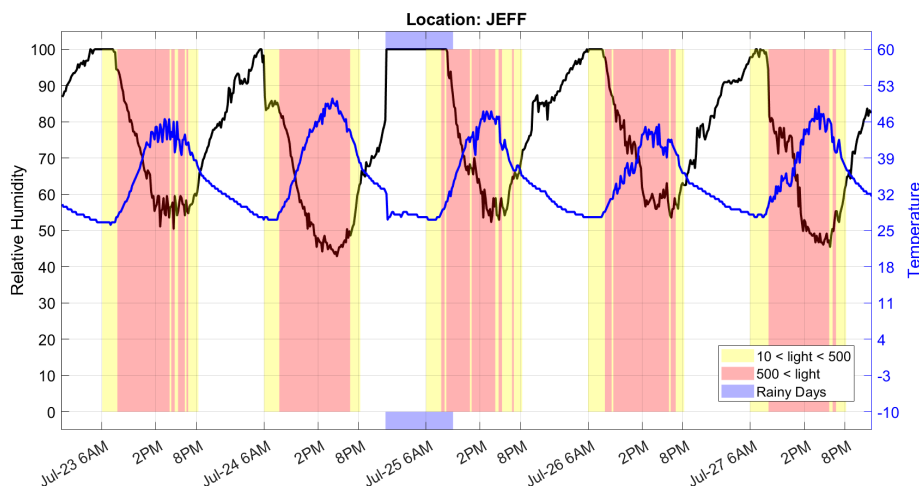


Figure 2.25: Plot with sample date selected in summer (07/23/2016-07/27/2016). (Black) Relative humidity and (blue) temperature. Red blocks in the plot represent high light intensity ($>500 \mu\text{mol} \cdot \text{m}^{-2} \cdot \text{s}^{-1}$), and the blue block in the plot represents activity of rain gauge, which means we have precipitation during that period. To check the validity of the data we collected from the rain gauge, we compared with the weather data collected by the National Oceanic and Atmospheric Administration (NOAA). During this time (07/23/2016-07/27/2016), there was a thunderstorm starting at midnight on 07/24/2016 which verifies our data.

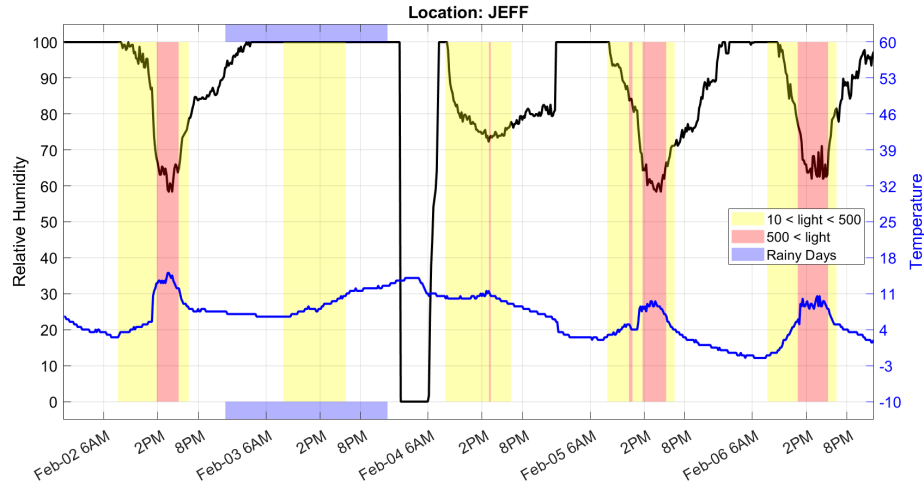


Figure 2.26: Plot with sample date selected in winter (02/02/2016-02/06/2016). (Black) Relative humidity and (blue) temperature. Red blocks in the plot represent high light intensity ($>500\mu\text{mol} \cdot \text{m}^{-2} \cdot \text{s}^{-1}$), and the blue block in the plot represents activity of rain gauge, which means we have precipitation during that period. Checking with the weather data collected by the National Oceanic and Atmospheric Administration (NOAA), we had rain on 02/03/2016, which validates the correctness of our data. Notice that there is a sudden drop in relative humidity on 02/04/2016. This irregularity might be attributed to the inaccuracy of a rain-soaked button.

2.3.2 Simulation for Deliquescence Model with Biofilm

In order to understand how biofilm grows in different weathers, we select 28 days in the summer (2016/07/13-2016/8/11) and 28 days in the winter (2016/01/21-2016/02/19) for simulations and compare the biomass after a one month period with the same initial conditions. We first plot the time series data of temperature and relative humidity (shown in figure 2.27 and 2.30), then apply the data to the deliquescence model with biofilm in chapter 2.2.3 (shown in figure 2.28 for 1 month data in the summer, figure 2.29 for three months duplicated data in the summer and figure 2.31 for one month data in the winter, figure 2.32 for three months duplicated data in the winter). We duplicate the data for three months to reproduce the biofilm living environment for a longer time in the extreme weathers.

Summer

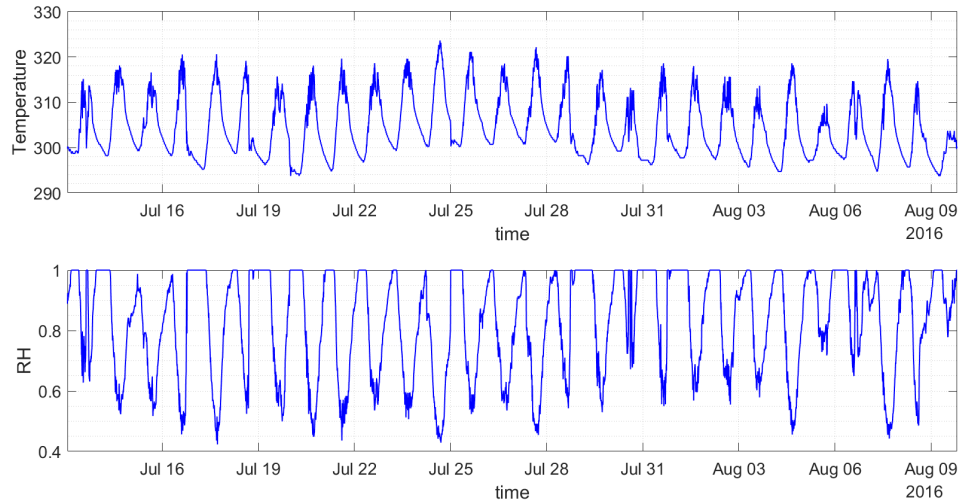


Figure 2.27: Summer data used for simulation.

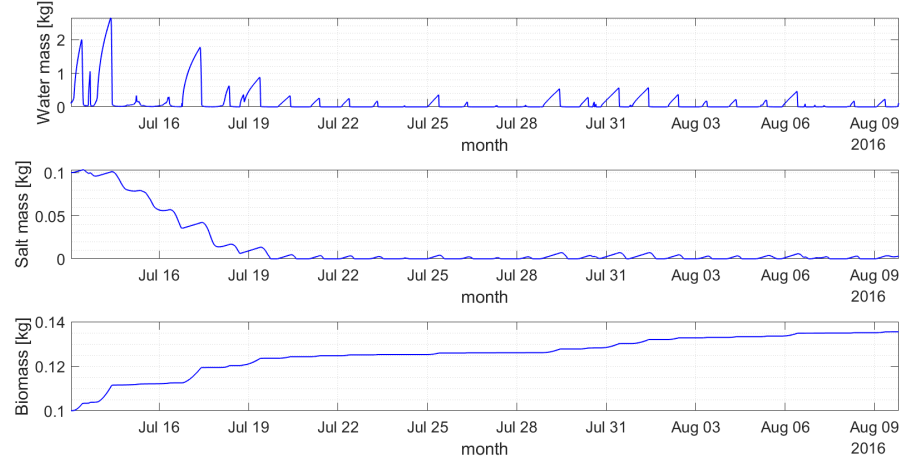


Figure 2.28: Water mass (top), salt mass (middle), and biomass (bottom). Parameters: $\eta = 10^{-6}$ and $N = 1kg$. Initial conditions: $m_w = 0.1kg$, $m_s = 0.1kg$, $m_b = 0.1kg$, Time period: 2016/07/13-2016/8/11.

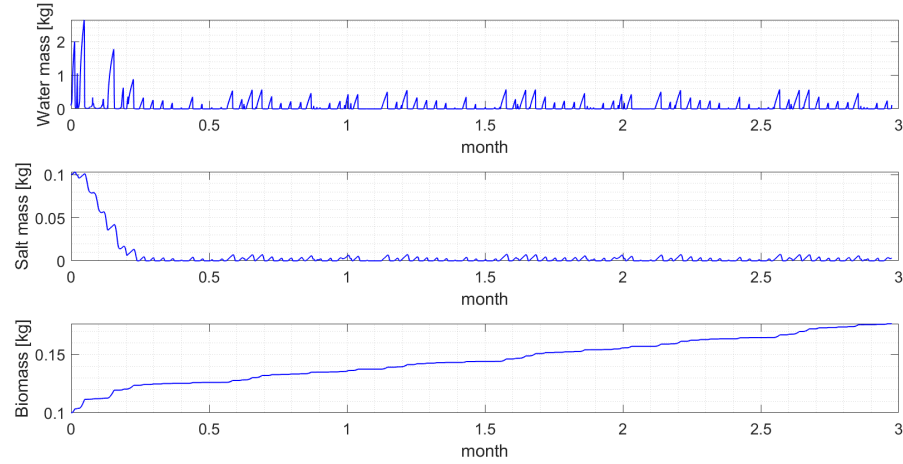


Figure 2.29: Water mass (top), salt mass (middle), and biomass (bottom). Parameters: $\eta = 10^{-6}$ and $N = 1kg$. Initial conditions: $m_w = 0.1kg$, $m_s = 0.1kg$, $m_b = 0.1kg$. Data: duplicated the temperature and RH data from figure 2.27 three times.

Winter

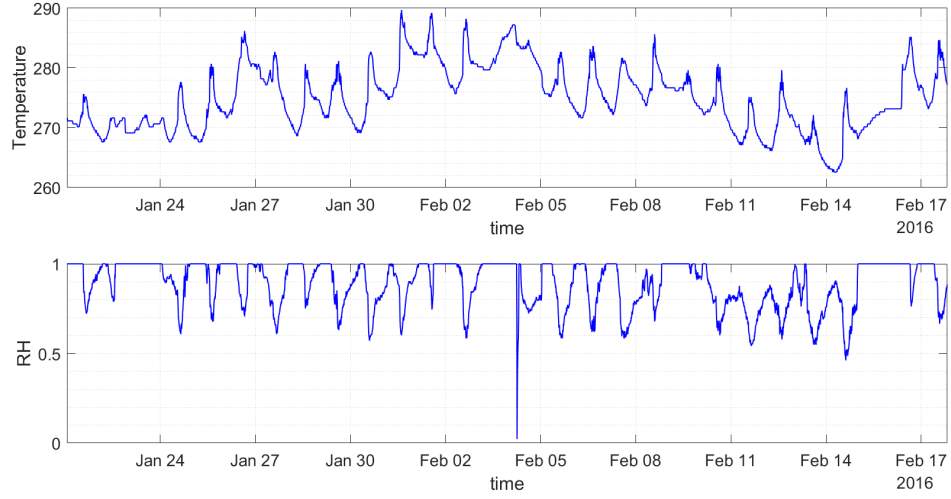


Figure 2.30: Winter data used for simulation.

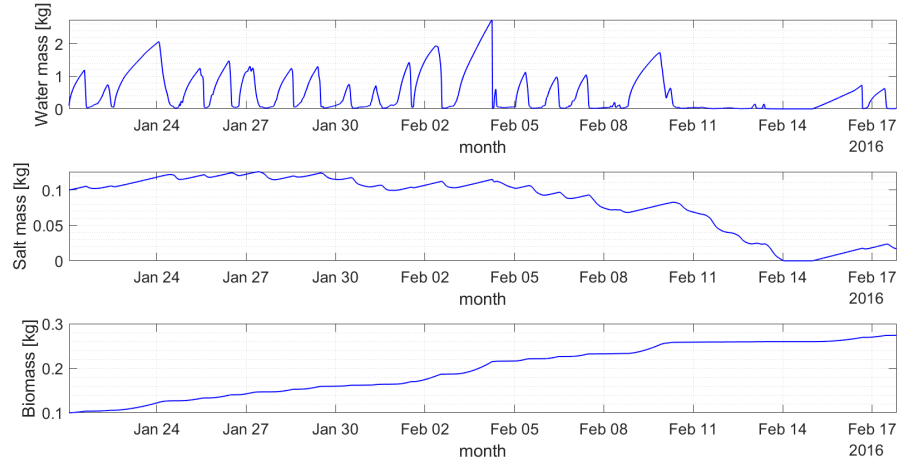


Figure 2.31: Water mass (top), salt mass (middle), and biomass (bottom). Parameters: $\eta = 10^{-6}$ and $N = 1kg$. Initial conditions: $m_w = 0.1kg$, $m_s = 0.1kg$, $m_b = 0.1kg$, Time period: 2016/01/21-2016/02/19.

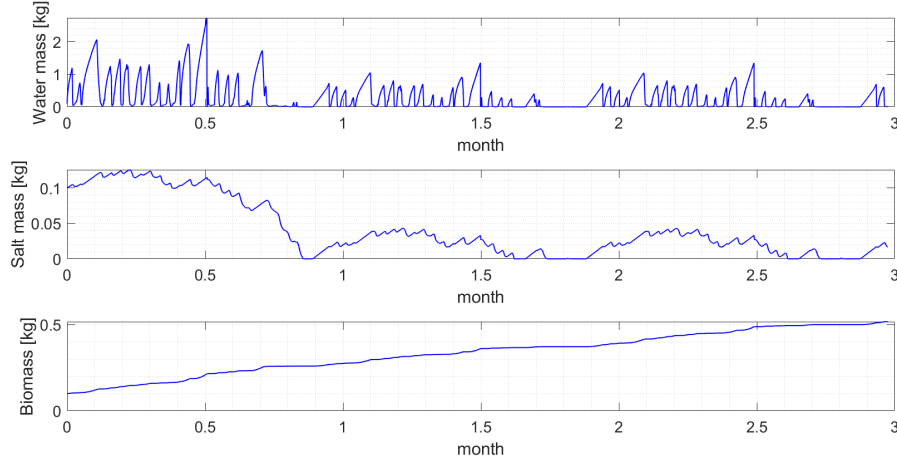


Figure 2.32: Water mass (top), salt mass (middle), and biomass (bottom). Parameters: $\eta = 10^{-6}$ and $N = 1kg$. Initial conditions: $m_w = 0.1kg$, $m_s = 0.1kg$, $m_b = 0.1kg$, Data: duplicated the temperature and RH data from figure 2.30 three times.

To compare the weather data for simulation (shown in figure 2.27, and 2.30), we find that the average relative humidity is 0.82 in the summer and 0.88 in the winter, while the average temperature is $304K$ (30.85°) in summer and $275K$ (1.85°) in winter. The temperature range is 294-322 degree Kelvin in the summer and 264-289 degree Kelvin in the winter. With the same initial conditions, the simulation results is $0.135kg$ in the summer (shown in the bottom plots in figure 2.28) and $0.28kg$ in the winter (shown in the bottom plots in figure 2.31) after 28 days. From this result, we can tentatively conclude that biofilm grows faster in the winter than in the summer. We duplicate the typical summer and winter data (2.27 and 2.30) three times, and run the simulation over this time period. After three months, biomass reaches approximately $0.18kg$ in summer (shown in the bottom plots in figure 2.29) and $0.5kg$ in winter (shown in the bottom plots in figure 2.32), which again shows that biofilm grows faster in the winter than in the summer in the long term. From this piece of information, though the temperature is higher in the summer, and biofilm does not grow faster due to the lower relative humidity.

Also, this result explains that both the relative humidity and temperature affect the increases in biomass: the higher relative humidity and temperature, the faster growth rate for biofilm.

2.3.3 Simulation for Deliquescence model with a Loss term

In order to account for the empirically observed biofilm growth, we add a loss term for biomass to limit the non-decreasing growth of biofilm. The deliquescence model for biofilm growth with a loss term is

$$m'_w(t) = \sqrt{\frac{M}{2\pi k_B}} \left(\sigma_c \frac{P_v}{\sqrt{T_V}} - \sigma_e \frac{P_s(T_L)}{\sqrt{T_L}} \right) - \eta m_b(t) m_w(t), \quad (2.65)$$

$$m'_s(t) = D \left(C_s - \frac{m_s(t) \rho_0}{m_w(t)} \right) \left(1 - \frac{m_s(t)}{m_s^{max}} \right), \quad (2.66)$$

$$m'_b(t) = \eta Y m_w(t) m_b(t) \left(1 - \frac{m_b(t)}{N} \right) - d m_b(t), \quad (2.67)$$

where d is the death rate of biofilm. The death rate d is small compared with the growth rate η .

Summer

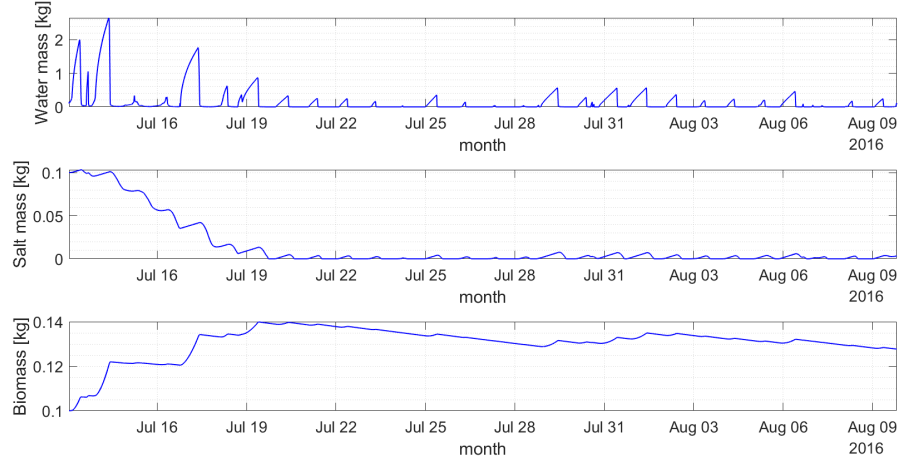


Figure 2.33: Water mass (top), salt mass (middle), and biomass (bottom). Parameters: $\eta = 10^{-6}$, $d = 1.5 \times 10^{-7}$, and $N = 1kg$. Initial conditions: $m_w = 0.1kg$, $m_s = 0.1kg$, and $m_b = 0.1$. Time period: 2016/07/13-2016/8/11.

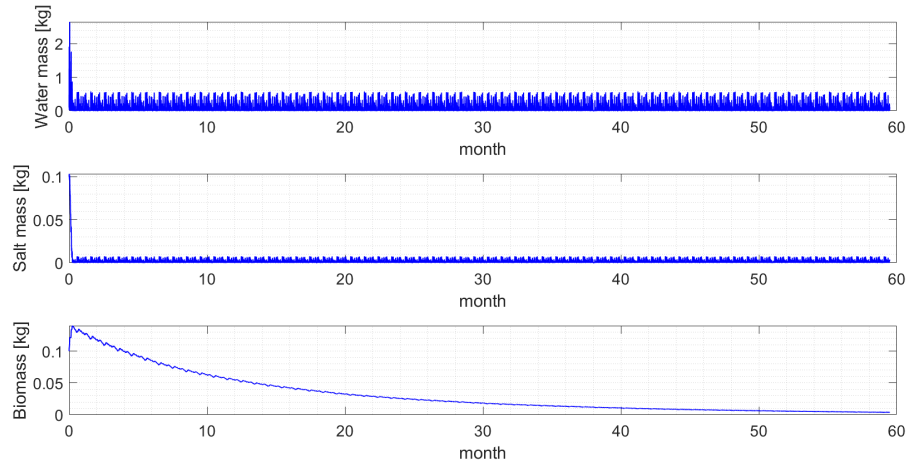


Figure 2.34: Water mass (top), salt mass (middle), and biomass (bottom). Parameters: $\eta = 10^{-6}$, $d = 1.5 \times 10^{-7}$, and $N = 1kg$. Initial conditions: $m_w = 0.1kg$, $m_s = 0.1kg$, and $m_b = 0.1$. Data: duplicated the temperature and RH data from figure 2.27 60 times (five years).

Winter

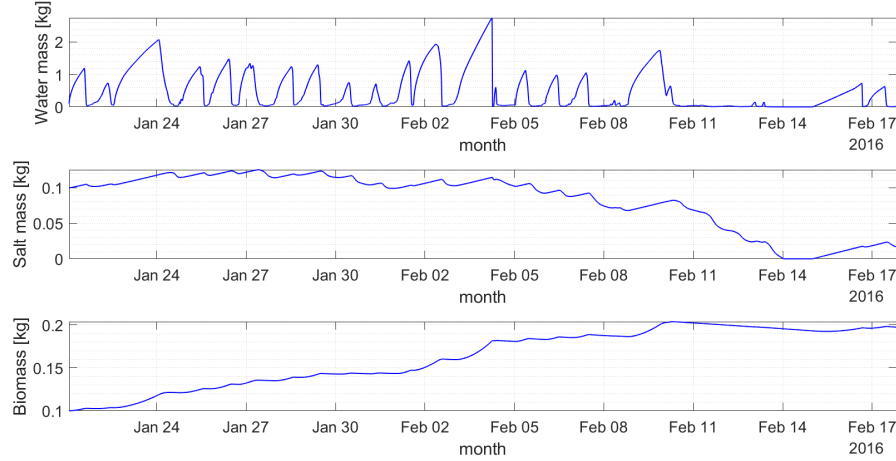


Figure 2.35: Water mass (top), salt mass (middle), and biomass (bottom). Parameters: $\eta = 10^{-6}$, $d = 1.5 \times 10^{-7}$, and $N = 1kg$. Initial conditions: $m_w = 0.1kg$, $m_s = 0.1kg$, and $m_b = 0.1$. Time period: 2016/01/21-2016/02/19.

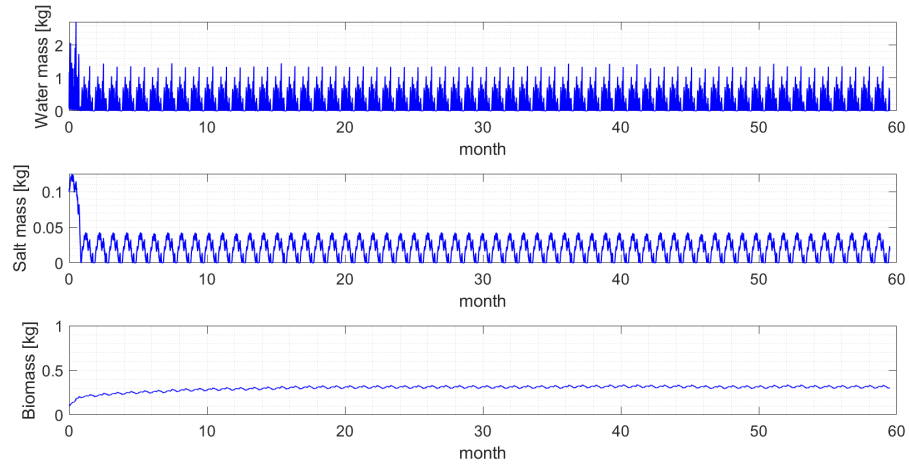


Figure 2.36: Water mass (top), salt mass (middle), and biomass (bottom). Parameters: $\eta = 10^{-6}$, $d = 1.5 \times 10^{-7}$, and $N = 1kg$. Initial conditions: $m_w = 0.1kg$, $m_s = 0.1kg$, and $m_b = 0.1$. Data: duplicated the temperature and RH data from figure 2.30 60 times (five years).

From the simulation, the biomass reaches $0.13kg$ (shown in figure 2.33) after one month and $0.01kg$ (shown in figure 2.34) after repeating 60 times of the summer data. The biomass reaches $0.2kg$ (shown in figure 2.35) after one month and $0.3kg$ (shown in figure 2.36) after repeating 60 times of the winter data.

2.3.4 Simulation for Deliquescence Model with Year-Around Data

From the previous section, we know that biomass increases faster in the winter than in the summer. In this section, we apply the model with the year-around data to confirm this phenomenon.

Data Preparation

We download the data from the weather station month by month. To simulate the loss term over an entire year, we clean the raw data as follows.

- Step (1) Put all the real-time monthly data together in one file to check if all the units are consistent, and all the data is in the right range (no outliers).
- Step (2) Fill the gaps by interpolation. There is a couple days gap between some of the two collections due to the limited memory of ibutton. We interpolate the missing data with the average or median (of the relative humidity and temperature data) from five days before and after the missing dates (use the values at the same time of the day).
- Step (3) Trim the data length to one year. After this step, we have year-round data starting from 05/20/2015 to 05/20/2016.

Simulations

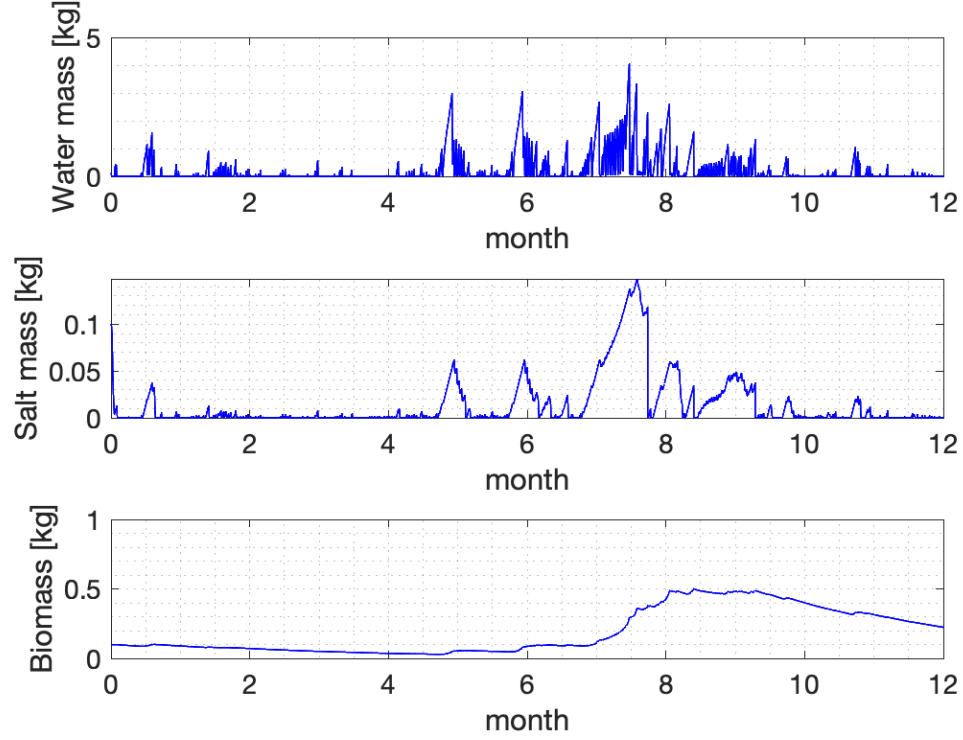


Figure 2.37: Water mass (top), salt mass (middle), and biomass (bottom). Parameters: $\eta = 10^{-6}$, $d = 1.5 \times 10^{-7}$, and $N = 1kg$. Initial conditions: $m_w = 0.1kg$, $m_s = 0.1kg$, and $m_b = 0.1$. Data Period: 05/20/2015-05/20/2016. From the plot, biofilm grows faster in the winter than in the summer.

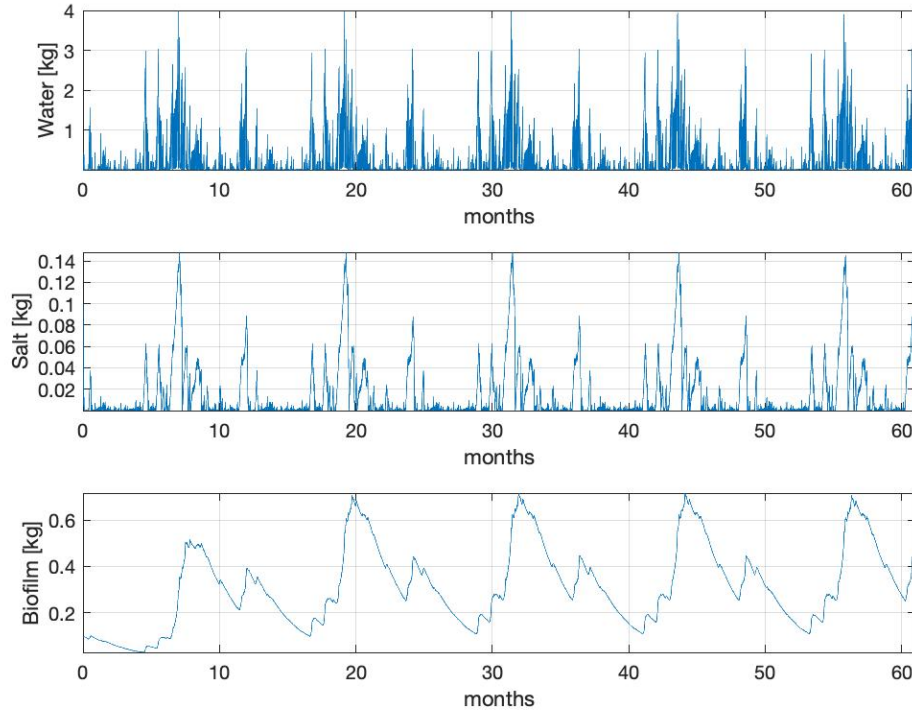


Figure 2.38: Water mass (top), salt mass (middle), and biomass (bottom). Parameters: $\eta = 10^{-6}$, $d = 1.5 \times 10^{-7}$, and $N = 1kg$. Initial conditions: $m_w = 0.1kg$, $m_s = 0.1kg$, and $m_b = 0.1$. Data: duplicated the temperature and RH data for the entire year 5 times (five years). Overall, biomass increases in winters and decreases in summers.

2.3.5 Conclusion and Discussion

In this section, we apply time series data we collect from the weather station on the roof of the Jefferson Memorial to the deliquescence model in Chapter 2.2.4 and a modified deliquescence model with a loss term in biomass. From our simulation results, the biofilm grows lightly faster in winter than in summer in both models. In the first model, biomass reaches $0.135kg$ in summer and $0.28kg$ in winter (shown in the bottom plots in figure 2.28 and 2.31) after 28 days. Also, biomass reaches approximately $0.18kg$ (shown in figure 2.29) in summer and $0.5kg$ (shown in figure 2.32) in winter if we run the model

over 3 months period (repeated the data three times). In the model with loss term, the biomass reaches $0.13kg$ (shown in in the bottom plots in figure 2.33) in summer and $0.2kg$ (shown in in the bottom plots in figure 2.35) in winter after one month. Also, biomass reaches approximately $0.55kg$ (shown in in the bottom plots in figure 2.34) in summer and $0.3kg$ (shown in in the bottom plots in figure 2.36) in winter if we run the model over 60 months period (repeated the data 60 times (five years)). Moreover, finally, we apply the data of the entire year to the model with loss term (shown in in the bottom plots in figure 2.37). According to the simulation result, biofilm growth is much faster in the winter season than in the summer season. Overall, biomass increases in years. However, our model only considered relative humidity and temperature data, which may not be sufficient to conclude that biofilm growth is faster during the winter (as we did not consider enough data, e.g., sunlight intensity).

2.4 Data Analysis

In this section, we apply a supervised learning algorithm to obtain a machine learning model which can be used to predict biofilm growth rate with given temperature and relative humidity (as training data).

2.4.1 Support Vector Machine

Support vector machine (SVM) analysis is a popular machine learning tool for classification and regression, first identified by Vladimir Vapnik and his colleagues in 1992 [117]. Our problem is continuous, so we can use support vector regression (SVR) instead of a classification algorithm. SVM regression is considered a nonparametric technique because it relies on kernel functions.

Suppose we are given training data $(x_1, y_1), \dots, (x_n, y_n) \in X \times \mathbb{R}$, where X denotes the spaces of the input patterns (e.g. $X = \mathbb{R}^d$ (real space of d dimensions)). In SVR, our goal is to find a function $f(x)$ that has the smallest deviation from the actually obtained targets y_i for all the training data, and at the same time is as flat as possible. The problem is to find the linear function

$$f(x) = \langle w, x \rangle + b, \quad (2.68)$$

where $w \in X$, $b \in \mathbb{R}$, and $\langle \cdot, \cdot \rangle$ denotes the inner product in X . Flatness means that one seeks a small w . One way to ensure this is to minimize the norm, i.e. $\|w\|^2 = \langle w, w \rangle$. We can write this problem as a convex optimization problem (all minimum are global), minimize

$$\frac{1}{2} \|w\|^2 = \langle w, w \rangle, \quad (2.69)$$

subject to

$$|y_i - \langle w, x_i \rangle - b| \leq \epsilon, \quad (2.70)$$

where ϵ is a small positive infinitesimal quantity.

2.4.2 k-fold Cross Validation

Cross-validation is a statistical method used to estimate the skill of machine learning models. It is commonly used in applied machine learning to compare and select a model for a given predictive modeling problem because the results in skill estimate that generally have a lower bias than other methods.

Cross-validation is a resampling procedure used to evaluate machine learning models on a limited data sample. The procedure has a single parameter called k that refers to the number of groups that a given data sample is to be split into (usually $5 \leq k \leq 10$). When a specific value for k is chosen, it may be used in place of k in reference to the model, such as $k = 10$ becoming 10-fold cross-validation. Since the data set is large enough, we choose $k = 5$ to train the data in this project, which means that we split all the data into five parts. The general procedure is as follows:

- Shuffle the dataset randomly.
- Split the dataset into k groups.
- For each group
 - Take the group as a test data set
 - Take the remaining groups as a training data set
 - Fit a model on the training set and evaluate it on the test set
 - Retain the evaluation score and discard the model
- Summarize the skill scores of the model.

Importantly, each observation in the data sample is assigned to an individual group and stays in that group for the duration of the procedure. This means that each sample is given the opportunity to be used in the test set 1 time and used to train the model $k-1$ times. The results of a k -fold cross-validation are often summarized with the mean of the model errors.

2.4.3 SVR Model Result

During the regression, we train relative humidity, temperature, and biofilm growth data (16 months in total).

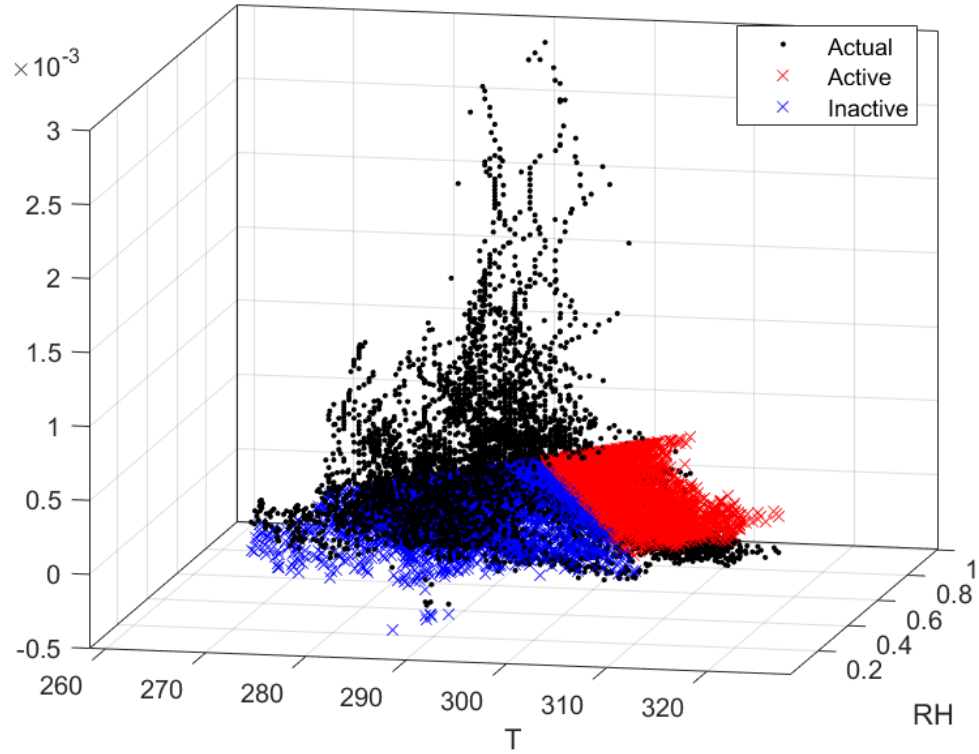


Figure 2.39: Black samples are time series data, the red and blue plane is the regression hyperplane (2D in this case). We trained the data with optimized hyperparameters and k-fold cross validation with $k = 5$. There are some outliers at $RH = 1$, which are statistical errors of the model.

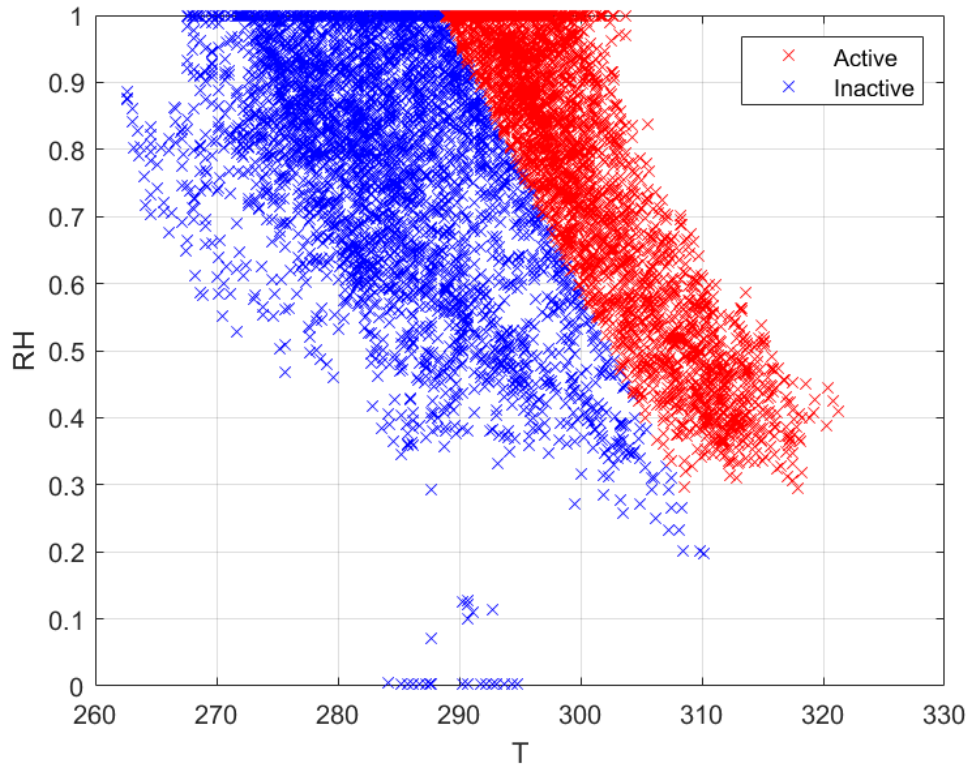


Figure 2.40: Activity of biofilm. Samples in red are active and in blue are inactive. The boundary is $RH = -0.03T + 6$. When $RH > -0.03T + 0.6$, biomass increases and conversely, decreases.

2.4.4 Conclusion and Discussion

We set a weather station on the roof of the Jefferson Memorial, from where we obtain sufficient data to study the living environment of biofilm on the dome. Applying the time series data on our deliquescence model with loss term, we obtain growth rates data for biofilm, from which we may create an activity region for biofilm activity with support vector regression. When the data falls inside the active region (red region shown in figure 2.40), biofilm is active. If any of the temperatures data is not in the active region (blue region shown in figure 2.40), biofilm stops growing until we obtain the ideal situation again. The boundary between two regions is the function $RH = -0.03T + 6$. When $RH > -0.03T + 0.6$, biomass increases and conversely, decreases.

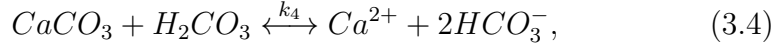
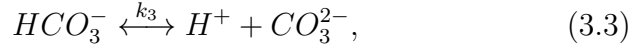
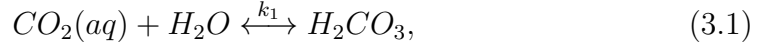
CHAPTER 3

FUTURE WORK

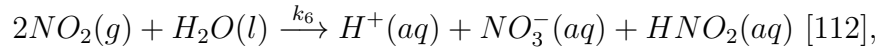
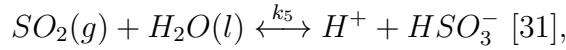
There are some ideas that I would like to try in the future.

- The deliquescence model we have in Chapter 2 is a basic model which only considered humidity and temperature so far. In the next step of this project, we will add some complexities to this model, e.g., time-dependent light intensity and time-dependent loss term of biofilm. Light intensity is one of the essential components for photosynthesis, so the growth rates for biofilm are different for day time and night time (also cloudy or sunny days) even with the same temperature and relative humidity data. The loss rate of biofilm also depends on the surrounding environment (extreme weathers, e.g., storm, snow, heat), which needs more discussion in the future.
- After a thin layer of liquid is produced from deliquescence, there will be a series of chemical reactions started with the dissolution of CO_2 from the air. Aqueous $CO_2(aq)$ undergoes several important inorganic reactions.

Consider the following reactions between $CO_2(aq)$, H_2O and $CaCO_3$ [77]



where k_1 , k_2 , k_3 , and k_4 are equilibrium reaction rate coefficients under prescribed conditions. Due to the pollution, we may also have sulfur dioxide (SO_2) and nitrogen dioxide (NO_2) in the air which also affects the pH of the solution,



where k_5 , k_6 are also equilibrium reaction rate constants under prescribed conditions. These reactions change the pH of the solution and may create an acidic environment on the marble, which may cause the loss of calcium ion (a main component of marble). In the next step of my research, I will consider the chemical kinetics in the deliquescence model with biofilm to simulate the damage of marble (stone, in general).

- In the last part of the thesis, I applied some machine learning techniques to train and test the prediction model with the existing data. This model can be used to predict the growth rate of biomass at any given temperature and humidity or the accumulated biomass after certain time period. So far, the method we have applied is support vector regression, and in the next step we will compare the results from different algorithms. Also, train and test the model with larger data sets to update the algorithm.

REFERENCES

- [1] E. Alpkvista and I. Klapper. A multidimensional multispecies continuum model for heterogeneous biofilm development. *Bulletin of Mathematical Biology*, 69(2):765–789, 2007.
- [2] AC. Aristotelous, I. Klapper, Y. Grabovsky, B. Pabst, B. Pitts, and P. Stewart. Diffusive transport through a model host-biofilm system. *Physical Review E*, 92(2):022703, 2015.
- [3] C. Baker-Austin and M. Dopson. Life in acid: ph homeostasis in acidophiles. *Trends in Microbiology*, 15(4):165–171, 2007.
- [4] E. Barghoorn and J. Schopf. Microorganisms three billion years old from the precambrian of south africa. *Science*, 152(3723):758–763, 1966.
- [5] S. Baron. *Classification–Medical Microbiology*. University of Texas Medical Branch at Galveston, 1996.
- [6] T. Bjarnsholt, M. Alhede, M. Alhede, S. Eickhardt-Sørensen, C. Moser, M. Kühl, P. Jensen, and N. Høiby. The in vivo biofilm. *Trends in Microbiology*, 21(9):466–474, 2013.
- [7] T. Bjarnsholt, K. Kirketerp-Møller, P. Jensen, K. Madsen, R. Phipps, K. Krogfelt, N. Høiby, and M. Givskov. Why chronic wounds will not heal: a novel hypothesis. *Wound Repair and Regeneration*, 16(1):2–10, 2008.

- [8] I. Booth. Regulation of cytoplasmic pH in bacteria. *Microbiological Reviews*, 49(4):359, 1985.
- [9] G. Borriello, E. Werner, F. Roe, A. Kim, G. Ehrlich, and P. Stewart. Oxygen limitation contributes to antibiotic tolerance of *Pseudomonas aeruginosa* in biofilms. *Antimicrobial Agents and Chemotherapy*, 48(7):2659–2664, 2004.
- [10] R. Bos, H. Van der Mei, and H. Busscher. Physico-chemistry of initial microbial adhesive interactions—its mechanisms and methods for study. *FEMS Microbiology Reviews*, 23(2):179–230, 1999.
- [11] S. Brooks, M. Wise, M. Cushing, and M. Tolbert. Deliquescence behavior of organic/ammonium sulfate aerosol. *Geophysical Research Letters*, 29(19):23–1, 2002.
- [12] M. Burmølle, T. Thomsen, M. Fazli, I. Dige, L. Christensen, P. Homøe, M. Tvede, B. Nyvad, T. Tolker-Nielsen, M. Givskov, et al. Biofilms in chronic infections—a matter of opportunity—monospecies biofilms in multispecies infections. *FEMS Immunology & Medical Microbiology*, 59(3):324–336, 2010.
- [13] HJ. Busscher and HC. Van der Mei. Physico-chemical interactions in initial microbial adhesion and relevance for biofilm formation. *Advances in Dental Research*, 11(1):24–32, 1997.
- [14] E. Campbell, W. Bruyninckx, C. Kelly, L. Glover, E. McNamee, B. Bowers, A. Bayless, M. Scully, B. Saeedi, L. Golden-Mason, et al. Transmigrating neutrophils shape the mucosal microenvironment through localized oxygen depletion to influence resolution of inflammation. *Immunity*, 40(1):66–77, 2014.
- [15] M. Chaudhry and S. Beg. A review on the mathematical modeling of biofilm processes: advances in fundamentals of biofilm modeling. *Chem-*

- ical Engineering & Technology: Industrial Chemistry-Plant Equipment-Process Engineering-Biotechnology*, 21(9):701–710, 1998.
- [16] Q. Chaudhry, M. Blom-Zandstra, S. Gupta, and E. Joner. Utilising the synergy between plants and rhizosphere microorganisms to enhance breakdown of organic pollutants in the environment (15 pp). *Environmental Science and Pollution Research*, 12(1):34–48, 2005.
 - [17] F. Chye, A. Abdullah, and M. Ayob. Bacteriological quality and safety of raw milk in malaysia. *Food Microbiology*, 21(5):535–541, 2004.
 - [18] F. Clarelli, C. Di Russo, R. Natalini, and M. Ribot. A fluid dynamics model of the growth of phototrophic biofilms. *Journal of Mathematical Biology*, 66(7):1387–1408, 2013.
 - [19] NG. Cogan and C. Wolgemuth. Pattern formation by bacteria-driven flow. *Biophysical Journal*, 88(4):2525–2529, 2005.
 - [20] J. Conway. The game of life. *Scientific American*, 223(4):4, 1970.
 - [21] J. Costerton. Introduction to biofilm. *International Journal of Antimicrobial Agents*, 11(3-4):217–221, 1999.
 - [22] J. Costerton, P. Stewart, and E. Greenberg. Bacterial biofilms: a common cause of persistent infections. *Science*, 284(5418):1318–1322, 1999.
 - [23] E. Cowley, S. Kopf, A. LaRiviere, W. Ziebis, and D. Newman. Pediatric cystic fibrosis sputum can be chemically dynamic, anoxic, and extremely reduced due to hydrogen sulfide formation. *MBio*, 6(4):e00767–15, 2015.
 - [24] D. Davies. Understanding biofilm resistance to antibacterial agents. *Nature Reviews Drug Discovery*, 2(2):114, 2003.
 - [25] R. Diegelmann. Excessive neutrophils characterize chronic pressure ulcers. *Wound Repair and Regeneration*, 11(6):490–495, 2003.

- [26] R. Dodge, R. Fairbanks, L. Benninger, and F. Maurrasse. Pleistocene sea levels from raised coral reefs of haiti. *Science*, 219(4591):1423–1425, 1983.
- [27] R. Donlan and J. Costerton. Biofilms: survival mechanisms of clinically relevant microorganisms. *Clinical Microbiology Reviews*, 15(2):167–193, 2002.
- [28] S. Dowd, Y. Sun, P. Secor, D. Rhoads, B. Wolcott, G. James, and R. Wolcott. Survey of bacterial diversity in chronic wounds using pyrosequencing, dgge, and full ribosome shotgun sequencing. *BMC Microbiology*, 8(1):43, 2008.
- [29] D. Downey, S. Bell, and J. Elborn. Neutrophils in cystic fibrosis. *Thorax*, 64(1):81–88, 2009.
- [30] H. Eberl and R. Sudarsan. Exposure of biofilms to slow flow fields: The convective contribution to growth and disinfection. *Journal of Theoretical Biology*, 253(4):788–807, 2008.
- [31] M. Falk and P. Giguère. On the nature of sulphurous acid. *Canadian Journal of Chemistry*, 36(7):1121–1125, 1958.
- [32] M. Fazli, T. Bjarnsholt, K. Kirketerp-Møller, A. Jørgensen, C. Andersen, M. Givskov, and T. Tolker-Nielsen. Quantitative analysis of the cellular inflammatory response against biofilm bacteria in chronic wounds. *Wound Repair and Regeneration*, 19(3):387–391, 2011.
- [33] T. Field, A. White, J. Elborn, and M. Tunney. Effect of oxygen limitation on the in vitro antimicrobial susceptibility of clinical isolates of pseudomonas aeruginosa grown planktonically and as biofilms. *European Journal of Clinical Microbiology and Infectious Diseases*, 24(10):677, 2005.

- [34] N. Fierer and R. Jackson. The diversity and biogeography of soil bacterial communities. *Proceedings of the National Academy of Sciences*, 103(3):626–631, 2006.
- [35] D. Frank, A. Wysocki, D. Specht-Glick, A. Rooney, R. Feldman, A. St. Amand, N. Pace, and J. Trent. Microbial diversity in chronic open wounds. *Wound Repair and Regeneration*, 17(2):163–172, 2009.
- [36] Y. Frankel, J. Melendez, N. Wang, L. Price, J. Zenilman, and G. Lazarus. Defining wound microbial flora: molecular microbiology opening new horizons. *Archives of Dermatology*, 145(10):1193–1195, 2009.
- [37] J. Goldberg, J. Pankey, I. Politis, B. Zavizion, and A. Bramley. Effect of oxygen tension on killing of escherichia coli by bovine polymorphonuclear neutrophil leucocytes in vitro. *Journal of Dairy Research*, 62(2):331–338, 1995.
- [38] A. Gorbushina and W. Broughton. Microbiology of the atmosphere-rock interface: how biological interactions and physical stresses modulate a sophisticated microbial ecosystem. *Annual Review of Microbiology*, 63:431–450, 2009.
- [39] R. Gough, V. Chevrier, and M. Tolbert. Formation of liquid water at low temperatures via the deliquescence of calcium chloride: Implications for antarctica and mars. *Planetary and Space Science*, 131:79–87, 2016.
- [40] A. Gristina, Y. Shibata, G. Giridhar, A. Kreger, and Q. Myrvik. The glycocalyx, biofilm, microbes, and resistant infection. In *Seminars in Arthroplasty*, volume 5, pages 160–170, 1994.
- [41] EA. Guggenheim. The theoretical basis of raoult’s law. *Transactions of the Faraday Society*, 33:151–156, 1937.
- [42] S. Gupta, N. Laskar, and D. Kadouri. Evaluating the effect of oxygen

- concentrations on antibiotic sensitivity, growth, and biofilm formation of human pathogens. *Microbiology Insights*, 9:MBI-S40767, 2016.
- [43] N. Gurung, S. Ray, S. Bose, and V. Rai. A broader view: microbial enzymes and their relevance in industries, medicine, and beyond. *BioMed Research International*, 2013, 2013.
- [44] A. Guss, G. Roeselers, I. Newton, C. Young, V. Klepac-Ceraj, S. Lory, and C. Cavanaugh. Phylogenetic and metabolic diversity of bacteria associated with cystic fibrosis. *The ISME Journal*, 5(1):20, 2011.
- [45] A. Han, J. Zenilman, J. Melendez, M. Shirtliff, A. Agostinho, G. James, P. Stewart, E. Mongodin, D. Rao, A. Rickard, et al. The importance of a multifaceted approach to characterizing the microbial flora of chronic wounds. *Wound Repair and Regeneration*, 19(5):532–541, 2011.
- [46] H. Harvey. *The chemistry and fertility of sea waters*. Cambridge University Press, 1955.
- [47] F. Harzevili and H. Chen. *Microbial Biotechnology: Progress and Trends*. CRC Press, 2018.
- [48] K. Heller. Probiotic bacteria in fermented foods: product characteristics and starter organisms. *The American Journal of Clinical Nutrition*, 73(2):374s–379s, 2001.
- [49] S. Hermanowicz. A model of two-dimensional biofilm morphology. *Water Science and Technology*, 37(4-5):219–222, 1998.
- [50] H. Heukelekian and A. Heller. Relation between food concentration and surface for bacterial growth. *Journal of Bacteriology*, 40(4):547, 1940.
- [51] H. Horn and S. Lackner. Modeling of biofilm systems: a review. In *Productive Biofilms*, pages 53–76. Springer, 2014.

- [52] J. Hyde, R. Darouiche, and J. Costerton. Strategies for prophylaxis against prosthetic valve endocarditis: a review article. *Journal of Heart Valve Disease*, 7(3):317–326, 1998.
- [53] G. James, Z. Ge, M. Usui, R. Underwood, H. Nguyen, H. Beyenal, E. deLancey Pulcini, A. Agostinho Hunt, H. Bernstein, and P. Fleckman. Microsensor and transcriptomic signatures of oxygen depletion in biofilms associated with chronic wounds. *Wound Repair and Regeneration*, 24(2):373–383, 2016.
- [54] G. James, E. Swogger, R. Wolcott, E. deLancey Pulcini, P. Secor, J. Sestrich, J. Costerton, and P. Stewart. Biofilms in chronic wounds. *Wound Repair and regeneration*, 16(1):37–44, 2008.
- [55] E. Jensen, A. Kharazmi, K. Lam, J. Costerton, and N. Høiby. Human polymorphonuclear leukocyte response to pseudomonas aeruginosa grown in biofilms. *Infection and Immunity*, 58(7):2383–2385, 1990.
- [56] A. Jesaitis, M. Franklin, D. Berglund, M. Sasaki, C. Lord, J. Bleazard, J. Duffy, H. Beyenal, and Z. Lewandowski. Compromised host defense on pseudomonas aeruginosa biofilms: characterization of neutrophil and biofilm interactions. *The Journal of Immunology*, 171(8):4329–4339, 2003.
- [57] M. Kalani, K. Brismar, B. Fagrell, J. Ostergren, and G. Jörneskog. Transcutaneous oxygen tension and toe blood pressure as predictors for outcome of diabetic foot ulcers. *Diabetes Care*, 22(1):147–151, 1999.
- [58] V. Kalia. *Microbial Factories: Biodiversity, Biopolymers, Bioactive Molecules*, volume 2. Springer, 2016.
- [59] P. King, D. Citron, D. Griffith, O. Lomovskaya, and M. Dudley. Effect of oxygen limitation on the in vitro activity of levofloxacin and other antibiotics administered by the aerosol route against pseudomonas aeruginosa

- from cystic fibrosis patients. *Diagnostic Microbiology and Infectious Disease*, 66(2):181–186, 2010.
- [60] I. Klapper and J. Dockery. Finger formation in biofilm layers. *SIAM Journal on Applied Mathematics*, 62(3):853–869, 2002.
- [61] I. Klapper and J. Dockery. Mathematical description of microbial biofilms. *SIAM Review*, 52(2):221–265, 2010.
- [62] S. Klebanoff. Oxygen metabolism and the toxic properties of phagocytes. *Annals of Internal Medicine*, 93(3):480–489, 1980.
- [63] O. Knacke and IN. Stranski. The mechanism of evaporation. *Progress in Metal Physics*, 6:181–235, 1956.
- [64] M. Kolpen, C. Hansen, T. Bjarnsholt, C. Moser, L. Christensen, M. van Gennip, O. Ciofu, L. Mandsberg, A. Kharazmi, G. Döring, et al. Polymorphonuclear leucocytes consume oxygen in sputum from chronic pseudomonas aeruginosa pneumonia in cystic fibrosis. *Thorax*, 65(1):57–62, 2010.
- [65] M. Kolpen, M. Kühl, T. Bjarnsholt, C. Moser, C. Hansen, L. Liengaard, A. Kharazmi, T. Pressler, N. Høiby, and P. Jensen. Nitrous oxide production in sputum from cystic fibrosis patients with chronic pseudomonas aeruginosa lung infection. *PloS One*, 9(1):e84353, 2014.
- [66] K. Kragh, M. Alhede, P. Jensen, C. Moser, T. Scheike, C. Jacobsen, S. Poulsen, S. Eickhardt-Sørensen, H. Trøstrup, L. Christoffersen, et al. Polymorphonuclear leukocytes restrict growth of pseudomonas aeruginosa in the lungs of cystic fibrosis patients. *Infection and Immunity*, 82(11):4477–4486, 2014.
- [67] J. Kreft, G. Booth, and J. Wimpenny. Bacsim, a simulator for individual-based modelling of bacterial colony growth. *Microbiology*, 144(12):3275–3287, 1998.

- [68] J. Kreft, C. Picioreanu, J. Wimpenny, and M. van Loosdrecht. Individual-based modelling of biofilms. *Microbiology*, 147(11):2897–2912, 2001.
- [69] C. Kumar and S. Anand. Significance of microbial biofilms in food industry: a review. *International Journal of Food Microbiology*, 42(1-2):9–27, 1998.
- [70] M. Van Loosdrecht, J. Heijnen, H. Eberl, J. Kreft, and C. Picioreanu. Mathematical modelling of biofilm structures. *Antonie van Leeuwenhoek*, 81(1-4):245–256, 2002.
- [71] M. Van Loosdrecht, J. Heijnen, H. Eberl, J. Kreft, and C. Picioreanu. Mathematical modelling of biofilm structures. *Antonie van Leeuwenhoek*, 81(1-4):245–256, 2002.
- [72] P. Louis and H. Flint. Diversity, metabolism and microbial ecology of butyrate-producing bacteria from the human large intestine. *FEMS Microbiology Letters*, 294(1):1–8, 2009.
- [73] J. Lyczak, C. Cannon, and G. Pier. Lung infections associated with cystic fibrosis. *Clinical Microbiology Reviews*, 15(2):194–222, 2002.
- [74] WN. Mack, JP. Mack, and AO. Ackerson. Microbial film development in a trickling filter. *Microbial Ecology*, 2(3):215–226, 1975.
- [75] G. Mandell. Bactericidal activity of aerobic and anaerobic polymorphonuclear neutrophils. *Infection and Immunity*, 9(2):337–341, 1974.
- [76] R. Marek and J. Straub. Analysis of the evaporation coefficient and the condensation coefficient of water. *International Journal of Heat and Mass Transfer*, 44(1):39–53, 2001.
- [77] G. Mills and H. Urey. The kinetics of isotopic exchange between carbon dioxide, bicarbonate ion, carbonate ion and water¹. *Journal of the American Chemical Society*, 62(5):1019–1026, 1940.

- [78] J. Monteith and M. Unsworth. *Principles of environmental physics: plants, animals, and the atmosphere*. Academic Press, 2013.
- [79] A. Morita, M. Sugiyama, H. Kameda, S. Koda, and D. Hanson. Mass accommodation coefficient of water: Molecular dynamics simulation and revised analysis of droplet train/flow reactor experiment. *The Journal of Physical Chemistry B*, 108(26):9111–9120, 2004.
- [80] N. Morris, D. Stickler, and R. McLean. The development of bacterial biofilms on indwelling urethral catheters. *World Journal of Urology*, 17(6):345–350, 1999.
- [81] W. Nicholson, N. Munakata, G. Horneck, H. Melosh, and P. Setlow. Resistance of bacillus endospores to extreme terrestrial and extraterrestrial environments. *Microbiology and Molecular Biology Reviews*, 64(3):548–572, 2000.
- [82] D. Noguera, G. Pizarfo, D. Stahl, and B. Rittmann. Simulation of multispecies biofilm development in three dimensions. *Water Science and Technology*, 39(7):123–130, 1999.
- [83] MJR. Nout. Fermented foods and food safety. *Food Research International*, 27(3):291–298, 1994.
- [84] A. Noyes and W. Whitney. The rate of solution of solid substances in their own solutions. *Journal of the American Chemical Society*, 19(12):930–934, 1897.
- [85] M. Oremland, K. Michels, A. Bettina, C. Lawrence, B. Mehrad, and R. Laubenbacher. A computational model of invasive aspergillosis in the lung and the role of iron. *BMC Systems Biology*, 10(1):34, 2016.
- [86] L. Passerini, K. Lam, J. Costerton, and E. King. Biofilms on indwelling vascular catheters. *Critical Care Medicine*, 20(5):665–673, 1992.

- [87] T. Petrak, Z. Kalodera, P. Novaković, and L. Karolyi. Bacteriological comparison of parallel and counter flow water chilling of poultry meat. *Meat Science*, 53(4):269–271, 1999.
- [88] C. Picioreanu, M. Van Loosdrecht, and J. Heijnen. Mathematical modeling of biofilm structure with a hybrid differential-discrete cellular automaton approach. *Biotechnology and Bioengineering*, 58(1):101–116, 1998.
- [89] C. Picioreanu, M. van Loosdrecht, and J. Heijnen. A new combined differential-discrete cellular automaton approach for biofilm modeling: Application for growth in gel beads. *Biotechnology and Bioengineering*, 57(6):718–731, 1998.
- [90] B. Pihlstrom, B. Michalowicz, and N. Johnson. Periodontal diseases. *The lancet*, 366(9499):1809–1820, 2005.
- [91] L. Price, C. Liu, J. Melendez, Y. Frankel, D. Engelthaler, M. Aziz, J. Bowers, R. Rattray, J. Ravel, C. Kingsley, et al. Community analysis of chronic wound bacteria using 16s rna gene-based pyrosequencing: impact of diabetes and antibiotics on chronic wound microbiota. *PloS One*, 4(7):e6462, 2009.
- [92] C. Truesdell and K. Rajagopal. *An introduction to the mechanics of fluids*. Springer, 2010.
- [93] KR. Rajagopal and L. Tao. Mechanics of mixtures. *Journal of Fluid Mechanics*, 323:410–410, 1996.
- [94] J. Richards and C. Melander. Controlling bacterial biofilms. *Chem-biochem*, 10(14):2287–2294, 2009.
- [95] B. Rittmann and P. McCarty. *Environmental biotechnology: principles and applications*. Tata McGraw-Hill Education, 2012.

- [96] L. Rothschild and R. Mancinelli. Life in extreme environments. *Nature*, 409(6823):1092, 2001.
- [97] Y. Rozen and S. Belkin. Survival of enteric bacteria in seawater. *FEMS Microbiology Reviews*, 25(5):513–529, 2001.
- [98] C. Ruangsetakit, K. Chinsakchai, P. Mahawongkajit, C. Wongwanit, and P. Mutirangura. Transcutaneous oxygen tension: a useful predictor of ulcer healing in critical limb ischaemia. *Journal of Wound Care*, 19(5):202–206, 2010.
- [99] J. Russell and D. Wilson. Why are ruminal cellulolytic bacteria unable to digest cellulose at low ph? *Journal of Dairy Science*, 79(8):1503–1509, 1996.
- [100] B. Schaible, C. Taylor, and K. Schaffer. Hypoxia increases antibiotic resistance in pseudomonas aeruginosa through altering the composition of multidrug efflux pumps. *Antimicrobial Agents and Chemotherapy*, 56(4):2114–2118, 2012.
- [101] J. Schopf. The fossil record: tracing the roots of the cyanobacterial lineage. In *The Ecology of Cyanobacteria*, pages 13–35. Springer, 2000.
- [102] C. Sen. Wound healing essentials: let there be oxygen. *Wound Repair and Regeneration*, 17(1):1–18, 2009.
- [103] C. Sen and S. Roy. Redox signals in wound healing. *Biochimica et Biophysica Acta (BBA)-General Subjects*, 1780(11):1348–1361, 2008.
- [104] R. Sender, S. Fuchs, and R. Milo. Revised estimates for the number of human and bacteria cells in the body. *PLoS Biology*, 14(8):e1002533, 2016.
- [105] S. Shimizu. 11 vitamins and related compounds: Microbial production. *Biotechnology*, page 319, 1996.

- [106] C. Sibley, M. Grinwis, T. Field, C. Eshaghurshan, M. Faria, S. Dowd, M. Parkins, H. Rabin, and M. Surette. Culture enriched molecular profiling of the cystic fibrosis airway microbiome. *PloS One*, 6(7):e22702, 2011.
- [107] V. Spence and W. Walker. Tissue oxygen tension in normal and ischaemic human skin. *Cardiovascular Research*, 18(3):140–144, 1984.
- [108] P. Stewart. Diffusion in biofilms. *Journal of Bacteriology*, 185(5):1485–1491, 2003.
- [109] P. Stewart. Biophysics of biofilm infection. *Pathogens and Disease*, 70(3):212–218, 2014.
- [110] P. Stewart, T. Zhang, R. Xu, B. Pitts, M. Walters, F. Roe, J. Kikhney, and A. Moter. Reaction–diffusion theory explains hypoxia and heterogeneous growth within microbial biofilms associated with chronic infections. *NPJ Biofilms and Microbiomes*, 2:16012, 2016.
- [111] X. Sun, X. Shen, R. Jain, Y. Lin, J. Wang, J. Sun, J. Wang, Y. Yan, and Q. Yuan. Synthesis of chemicals by metabolic engineering of microbes. *Chemical Society Reviews*, 44(11):3760–3785, 2015.
- [112] R. Svensson, E. Ljungström, and O. Lindqvist. Kinetics of the reaction between nitrogen dioxide and water vapour. *Atmospheric Environment*, 21(7):1529–1539, 1987.
- [113] I. Tang and H. Munkelwitz. Composition and temperature dependence of the deliquescence properties of hygroscopic aerosols. *Atmospheric Environment. Part A. General Topics*, 27(4):467–473, 1993.
- [114] C. Taylor, G. Doherty, P. Fallon, and E. Cummins. Hypoxia-dependent regulation of inflammatory pathways in immune cells. *The Journal of Clinical Investigation*, 126(10):3716–3724, 2016.

- [115] C. Truesdell and K. Rajagopal. *An introduction to the mechanics of fluids*. Springer, 2010.
- [116] M. Tunney, T. Field, T. Moriarty, S. Patrick, G. Doering, M. Muhlebach, M. Wolfgang, R. Boucher, D. Gilpin, A. McDowell, et al. Detection of anaerobic bacteria in high numbers in sputum from patients with cystic fibrosis. *American Journal of Respiratory and Critical Care Medicine*, 177(9):995–1001, 2008.
- [117] V. Vapnik. *The nature of statistical learning theory*. Springer, 2013.
- [118] F. Villa, P. Stewart, I. Klapper, J. Jacob, and F. Cappitelli. Subaerial biofilms on outdoor stone monuments: changing the perspective toward an ecological framework. *Bioscience*, 66(4):285–294, 2016.
- [119] Q. Wang and T. Zhang. Review of mathematical models for biofilms. *Solid State Communications*, 150(21-22):1009–1022, 2010.
- [120] K. Williamson and P. McCarty. Verification studies of the biofilm model for bacterial substrate utilization. *Journal (Water Pollution Control Federation)*, pages 281–296, 1976.
- [121] J. Wimpenny and R. Colasanti. A unifying hypothesis for the structure of microbial biofilms based on cellular automaton models. *FEMS Microbiology Ecology*, 22(1):1–16, 1997.
- [122] J. Wingender and H. Flemming. Biofilms in drinking water and their role as reservoir for pathogens. *International Journal of Hygiene and Environmental Health*, 214(6):417–423, 2011.
- [123] C. Woese and G. Fox. Phylogenetic structure of the prokaryotic domain: the primary kingdoms. *Proceedings of the National Academy of Sciences*, 74(11):5088–5090, 1977.
- [124] D. Worlitzsch, R. Tarran, M. Ulrich, U. Schwab, A. Cekici, K. Meyer, P. Birrer, G. Bellon, J. Berger, T. Weiss, et al. Effects of reduced mucus

- oxygen concentration in airway pseudomonas infections of cystic fibrosis patients. *The Journal of Clinical Investigation*, 109(3):317–325, 2002.
- [125] Y. Wu, I. Klapper, and P. Stewart. Hypoxia arising from concerted oxygen consumption by neutrophils and microorganisms in biofilms. *Pathogens and Disease*, 76(4):fty043, 2018.
- [126] K. Xu, P. Stewart, F. Xia, C. Huang, and G. McFeters. Spatial physiological heterogeneity in pseudomonas aeruginosa biofilm is determined by oxygen availability. *Applied Environmental Microbiology*, 64(10):4035–4039, 1998.
- [127] Y. Xu, R. Maltesen, L. Larsen, H. Schønheyder, V. Le, J. Nielsen, P. Nielsen, T. Thomsen, and K. Nielsen. In vivo gene expression in a staphylococcus aureus prosthetic joint infection characterized by rna sequencing and metabolomics: a pilot study. *BMC Microbiology*, 16(1):80, 2016.
- [128] S. Yoon, R. Hennigan, G. Hilliard, U. Ochsner, K. Parvatiyar, M. Kamani, H. Allen, T. DeKievit, P. Gardner, U. Schwab, et al. Pseudomonas aeruginosa anaerobic respiration in biofilms: relationships to cystic fibrosis pathogenesis. *Developmental Cell*, 3(4):593–603, 2002.
- [129] E. Zaura-Arite, J. Van Marle, and JM. Ten Cate. Confocal microscopy study of undisturbed and chlorhexidine-treated dental biofilm. *Journal of Dental Research*, 80(5):1436–1440, 2001.
- [130] E. Zemanick, S. Sagel, and J. Harris. The airway microbiome in cystic fibrosis and implications for treatment. *Current opinion in pediatrics*, 23(3):319–324, 2011.
- [131] Z. Zhang, D. Claessen, and D. Rozen. Understanding microbial divisions of labor. *Frontiers in Microbiology*, 7:2070, 2016.

- [132] G. Zhao, P. Hochwalt, M. Usui, R. Underwood, P. Singh, G. James, P. Stewart, P. Fleckman, and J. Olerud. Delayed wound healing in diabetic (db/db) mice with pseudomonas aeruginosa biofilm challenge: a model for the study of chronic wounds. *Wound Repair and Regeneration*, 18(5):467–477, 2010.
- [133] C. Zobell. The effect of solid surfaces upon bacterial activity. *Journal of Bacteriology*, 46(1):39, 1943.